UNIVERSITY OF SOUTHAMPTON

SPECTROSCOPY OF CHROMIUM DOPED GLASS FOR AMPLIFIERS AND LASERS

Charles Richard Haythornthwaite

Thesis submitted for the qualification of
Doctor of Philosophy

Optoelectonic Research Centre

Faculty of Science

September 1999

UNIVERSITY OF SOUTHAMPTON

ABSTRACT

FACULTY OF SCIENCE
OPTOELECTRONIC RESESEARCH CENTRE

Doctor of Philosophy

SPECTROSCOPY OF CHROMIUM DOPED GLASS FOR AMPLIFIERS AND LASERS

by Charles Richard Haythornthwaite

To date, there has been no demonstration of a transition metal laser that uses a glass host. Calculations show that if reasonable pump power could be confined to the small cross-sectional area of a fibre optic core, the threshold pump power could be brought down to a realistic level for laser action. A transition metal fibre laser, if practicable, would make a cheap, compact and highly tunable laser source in the near infrared. This project comprised two parts. Firstly, spectroscopy and developmental work on a host glass identified as being an excellent prospect for a Cr^{3+} fibre laser. Secondly, the spectroscopic investigation of a new family of glass found to host Cr^{4+}.

Lithium lime silicate (LLS) glass was identified as an excellent prospect for a Cr^{3+} fibre laser. Not only possessing suitable thermal properties for fibre drawing, LLS had a radiative quantum efficiency (QE) measured as 15% - a very high figure for Cr^{3+} doped glass. It absorbed in two broad bands, 400-500nm and 600-750nm and the emission spectrum was also extremely broad, extending between 700nm and 1050nm. The upper state lifetime was about 35μs and the peak cross-section of emission was found to be $6x10^{-21}cm^2$. The LLS composition was optimised in terms of its spectroscopy and thermal properties and a fibre was fabricated. An excited state absorption (ESA) investigation was performed on the fibre – this is believed to be the first report of an ESA experiment on transition metal doped glass. Unfortunately, the fibre quality was not sufficient to make a realistic attempt at a demonstration of a fibre laser.

There are very few glasses known to host Cr^{4+}, and none of these have thermal properties suitable for fibre drawing. This thesis reports the discovery that sulphide chalcogenide glasses, which are stable enough for fibre drawing, also host the chromium (IV) ion. A wide range of sulphide based glass was fabricated and the spectroscopic investigation revealed the QE to be low, ranging from 0 to 3%. The absorption spectra typically extended between 600nm and 1300nm and the emission between 0.8μm and 1.5μm. As the samples were warmed up from liquid nitrogen to room temperature, the peak of emission experienced a remarkable blue shift of up to 400nm owing to a site-dependent non-radiative decay mechanism. The upper state lifetime was found to be about 1μs. Despite the low QE and short lifetime, calculations suggest that laser action in a low-loss narrow-cored fibre might still be feasible. However, the lifetime cross-section product for arsenic trisulphide, the best of the glasses tried, was about a factor of six times smaller than the Cr^{3+} doped LLS.

CONTENTS

Acknowledgements

I am very grateful to everybody who has helped me over the last four years. Perhaps the ORC's greatest strengths are the broad expertise of those who work there and their spirit of cooperation.

My special thanks to the following:

Jason Hector, my long-term lab partner in crime

Ji Wang for his tutorials in glass fabrication (I always admired his fearless approach)

Beth Taylor who continued the fabrication supervision

Dan Hewak for his chalcogenide glass expertise

Roger Moore who pulled the fibre and taught me "Failing to prepare is preparing to fail"

Thorsten Schweitzer who contributed to the fibre investigations

EPSRC for my funding

And particularly, Bill Brocklesby for all his excellent supervision.

I hope that, overall, I have helped rather than hindered the advancement of Science.

Chapter 1

Introduction

1.1 Overview

Solid state lasers that make use of transition metals as the active ion have had a long history and can, in fact, be traced back to the first demonstration of laser action - the Cr doped ruby laser[1]. There have been many more transition metal lasers developed since then which have generally been noted for having the characteristic of much broader absorption and emission bands than devices relying on rare earths as the lasing ion. Much of the impetus for the research towards finding new tunable sources lies in the importance of their applications; spectroscopy, modelocking[2], environmental sensing and medicine are all fields where a range of widely tunable lasers centred at different wavelengths can be put to great effect. Table 1 shows which transition metal ions have been made to lase, and centred at which wavelength.

Probably the best known tunable solid state laser is the Titanium Doped Sapphire Laser, well recognised as an excellent light source in the near infrared. Having a tuning range approaching 300nm (with several mirror sets), and being easily pumped by the Ar ion laser for cw action, this particular transition metal laser has proven itself especially useful.

In the late 1980's, two new crystalline hosts for Cr were discovered which led to very effective lasers – Cr^{3+}:LiSAF [3] and Cr^{3+}:LiCAF [4]. Although these materials have a smaller tuning range than the Ti Sapphire laser they have the advantages of impressive energy storage lifetime, much-reduced pump thresholds and the possibility of being diode pumped.

Transition Metal Ion	Outer Electrons	Ligand Site Symmetry	Example of Crystal Lasers
Ti^{3+}	1	O_h	
Cr^{3+}	3	O_h	
Cr^{4+}	2	T_d	
Ni^{2+}	8	O_h T_d	
Co^{2+}	7	O_h T_d	
Cr^{2+}	4	T_d	

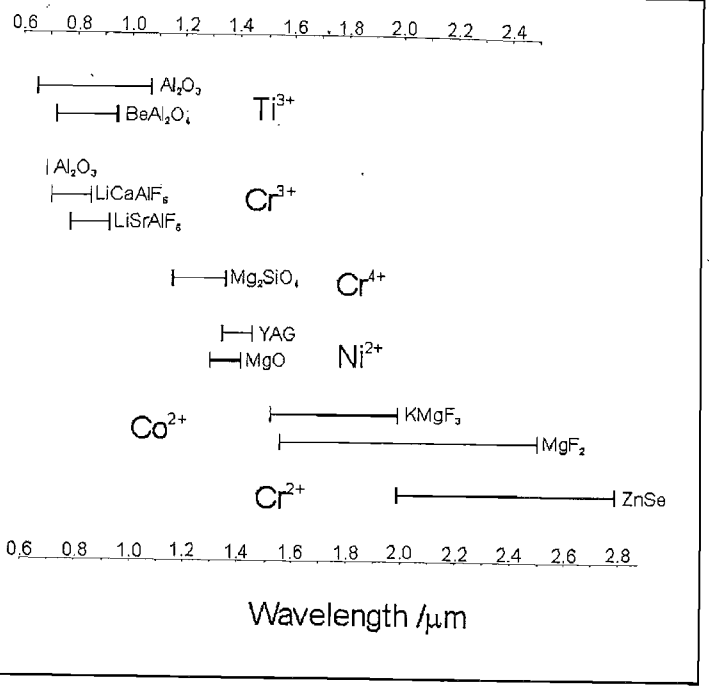

Table 1.1: **Transition Metal Ion Crystal Lasers**

(Information gathered from Laser Materials by F. Gan, World Scientific)

Unfortunately, the fabrication of high quality laser crystals is an expensive procedure and using large pump lasers means the system as a whole is bulky. New devices, with similar spectral properties but cheaper and more compact, would generate a great deal of interest if they could be developed.

Recently, two Ti sapphire waveguide lasers have been developed[5,6]. These represent the first demonstration of cw, room temperature, transition metal waveguide lasers. As well as being compact, the waveguide geometry brings about lower pump thresholds and being pumped in the blue offers the potential for blue diode laser pumping in the future.

Waveguide lasers, however, represent just one potential solution. An alternative line of reasoning suggests that if crystals are so expensive to produce, then perhaps adding transition metal ions to a glass might lead to cheaper lasers. Unhappily there are complications and to date as there has been no prior demonstration of a transition metal laser utilising a glass host. Already having small lifetimes, the transition metals when put into an amorphous host experience a very dramatic reduction in radiative quantum

efficiency. These two spectroscopic characteristics, when taken together, lead to high threshold pump powers making bulk lasers infeasible. Although technically difficult to do, if transition metals could be incorporated into optical fibres, laser action might then be possible: confinement of the pump beam leads to lower thresholds. This idea was the rationale behind this project. With a careful programme of spectroscopy and glass development, and then utilising the Optoelectronic Research Centre's soft-glass fibre-drawing capability, the aim was to work towards the first transition metal fibre laser. Out of the great range of possible transition metal ions that could have been chosen, this project has focussed on two in particular – Cr^{3+} and Cr^{4+}.

1.2 The Decision for Cr^{3+}

Interestingly, the element chromium is unique in the fact that it has had laser action demonstrated with as many as three different valencies of ion – Cr^{2+}, Cr^{3+} and Cr^{4+}. Cr^{3+} was a logical place to start since out of all the transition metal ions, Cr^{3+} has been shown to lase with the greatest number of different crystalline hosts[3] and its spectroscopy within crystals has been the most widely investigated. This seemed even more the case for glass hosts where trivalent chromium is the only transition metal ion that has had any sort of thorough spectroscopic investigation. There are a number of papers that have looked specifically at the radiative quantum efficiency of a great range of glasses, making an excellent start to overcoming the primary obstacle to the development of a laser.

In addition to trivalent chromium's track record as a lasing ion, a Cr^{3+} fibre laser would be a very attractive device. Having broad emission in the near infrared and an absorption band about 630nm suitable for diode pumping, there is the potential for a cheap compact alternative to the Ti sapphire laser.

1.3 The Decision for Cr^{4+}

One of the fundamental components in an optical telecommunications system is the fibre amplifier, which boosts the digital signal to overcome the inevitable attenuation along a long distance trunk route or maybe the splitting of the signal by the subdividing branches to many destinations.

Wave division multiplexing[7] is a solution to the problem of obtaining the maximum possible capacity out of an optical fibre network. Here many different digital signals are sent in parallel by coding them in terms of different wavelengths that are later separated at the end of a transmission route. What ultimately limits the number of channels that can be used is the size of the gain bandwidth of the optical amplifier.

To give some perspective, the Erbium Doped Fibre Amplifier, which is commonly used to boost optical signals occupying the 1.55μm telecommunications window, has a gain bandwidth of 35nm[8]. Now, Cr^{4+} has an emission bandwidth greater than 300nm at 1.3μm coincident with the second telecommunications window. It is very easy to see that an effective fibre amplifier utilising Cr^{4+} as the active ion would be an extremely attractive device.

In recent years, several Cr^{4+} crystal lasers have been developed, such as the Cr^{4+}:YAG and Cr^{4+}:Forsterite[9]. In glass hosts, however, it is very unusual to get stable Cr^{4+} rather than the more common Cr^{3+} and Cr^{6+}. In fact only three families of glass hosting Cr^{4+} have been cited in the literature and often with little emphasis on emission spectroscopy unfortunately. These three glasses[10] - aluminosilicates, gallates and aluminates[11] – all have poor thermal properties precluding any possibility of fibre fabrication and therefore an optical amplifier. Part of the project's aims was to search for a new glass hosting Cr^{4+} but with better characteristics for drawing fibre, hopefully leading to an amplifier or a laser in the future.

1.4 Form of the Project

Right from the start there was a clear strategy of how to how to achieve the project's aims effectively and develop a new fibre laser. Figure 1.1 gives a diagrammatic outline of the strategy taken to develop a laser. The range of techniques has been extremely broad including elements of fabrication, spectroscopy and device work.

The first stage involved melting a great number of sample glasses. It was hoped that investigating a large range of host compositions would lead to, firstly, a better understanding of what controlled key spectroscopic characteristics, secondly, the discovery of interesting new compositions, and finally the development and optimisation of old compositions. Once the bulk samples had been fabricated, they had

to be evaluated. This involved a full programme of spectroscopy but the critical experiments for predicting the potential for gain investigated excited-state radiative lifetimes and the radiative quantum efficiency. The best of these samples then had their thermal properties tested to see if they might be suitable for fibre drawing.

Glass compositions which had both good spectroscopy and good thermal properties could be drawn into fibres which were themselves evaluated. The particularly important investigations, here, were fibre loss, excited-state absorption and gain experiments. After any of the stages of evaluation (bulk spectroscopy, thermal properties or fibre spectroscopy), adjustments to the original glass composition or to the fabrication techniques could be made in order to lead to improved fibre. If at the end of this procedure a fibre with good gain is produced, there could then be an attempt to make a fibre laser.

1.5 The Form of the Thesis

This thesis comprises nine chapters describing the work carried out in this project. Chapter 2 introduces the basic theory to transition metal ion spectroscopy and glass chemistry that is required to analyse the results of this work. Much of the chapter explains why transition metals have such broad transitions and why these ions have poor radiative quantum efficiency when they sit within glass hosts. The spectroscopic techniques that were used throughout the project to investigate the bulk samples are described in Chapter 3.

The first section of results comes in Chapter 4, which covers the spectroscopy of the Cr^{3+} bulk glass samples. Out of the glasses investigated, lithium lime silicate glass was found to be the most promising in terms of a device and the results indicated what might be the optimal composition spectroscopically. Chapter 5 briefly gives the results of a theoretical treatment for how light propagates along passive waveguides and introduces a simple model to estimate the gain for a fibre amplifier.

The next chapter, Chapter 6, describes the fabrication techniques that were developed in order to draw lithium lime silicate fibre. The glass composition for the fibre was chosen for its favourable viscosity properties to produce bubble free glass as well as taking advantage of the spectroscopy results of Chapter 4.

Figure 1.1 : **A Route Towards a Laser**

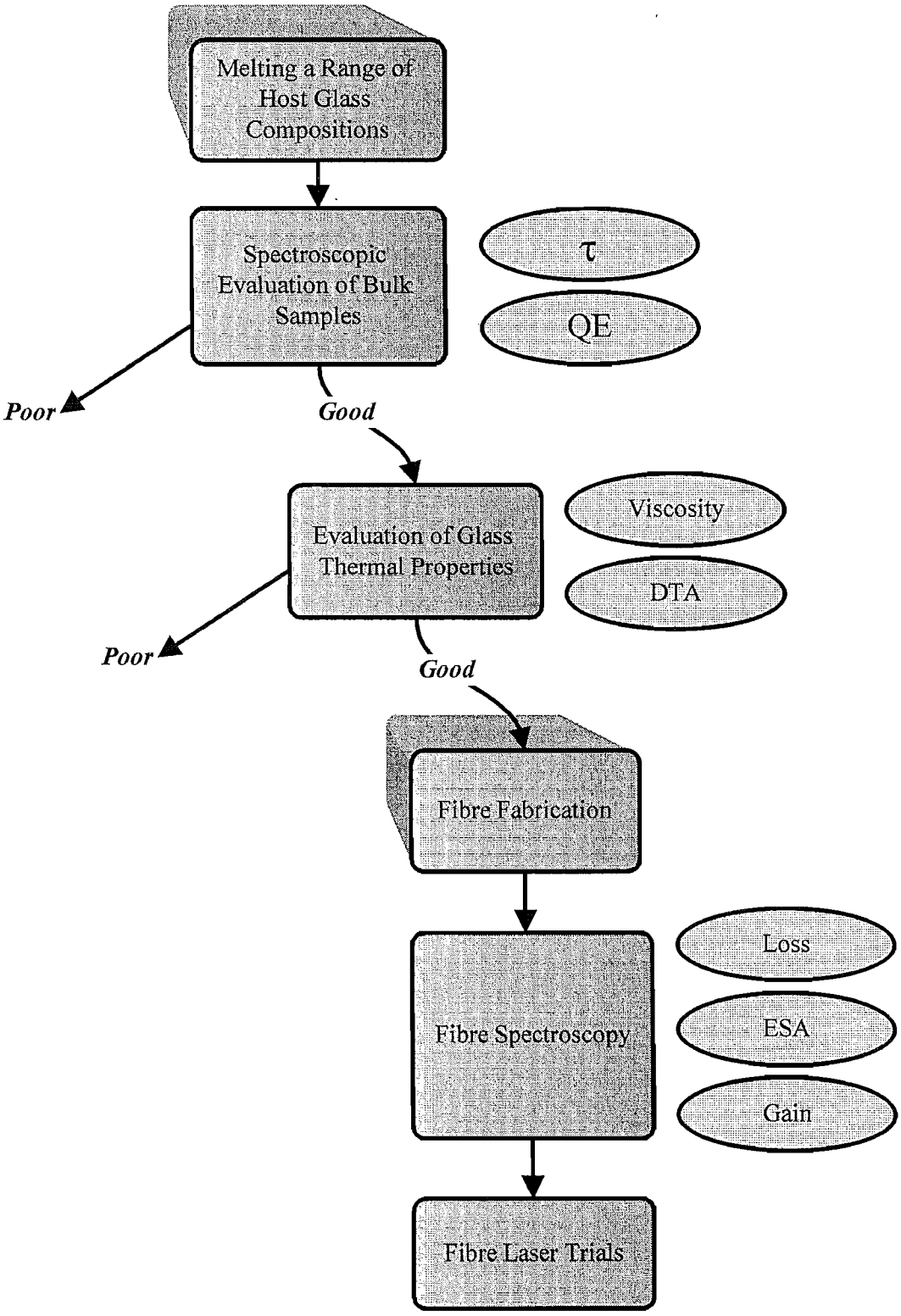

Chapter 7 reports the results for the investigation of the lithium lime silicate fibre. The excited state absorption (ESA) investigation is believed to be the first yet carried out looking at a transition metal within a glass host. The experiment revealed that ESA will be a significant obstacle for a successful laser. A gain investigation on the best fibre available was also carried out. Although the result was not clear cut, it was believed to be consistent with gain.

The final results chapter, Chapter 8, moves on to the topic of a new glass family that hosts the Cr^{4+} ion. Ten sulphide chalcogenide glasses were melted and investigated spectroscopically to determine their suitability as hosts for future fibre amplifiers and lasers. Chapter 9 is a summary chapter for the whole thesis and includes a discussion for the direction of future work.

---

[1] "Stimulated Optical Radiation in Ruby", T H Maiman, Nature, **187**, 493 (1960)
[2] "Broadly Tunable Femtosecond Solid-State Laser Sources", W Sibbett, R Grant and D Spence, Appl. Phys. B, **58**, 171 (1994)
[3] "Laser Performance of $LiSrAlF_6:Cr^{3+}$", S Payne, L Chase, L Smith, W Kway and H Newkirk, J. Appl. Phys., **66**, 1051 (1989)
[4] "$LiCaAlF_6:Cr^{3+}$: A Promising New Solid-State Laser Material", S Payne, L Chase, H Newkirk, L Smith and W Krupke, IEEE J. Quantum Electron., **24**, 2243 (1988)
[5] "Ti:Sapphire Planar Waveguide Laser Grown by Pulsed Laser Deposition" A A Anderson and R Eason, Optics Letters, **22**, (20), 1556 (1997)
[6] "Titanium Diffused Waveguides in Sapphire", L Hickey and J Wilkinson, Electronic Letters, **32**, (24), p2238 (1996)
[7] "Optical Fiber Telecommunications IIIB", ed I Kaminow, Academic Press, Chapter 2
[8] "Optical Fiber Telecommunications IIIB", ed I Kaminow, Academic Press, Chapter 2, pg23
[9] "Laser Action in Chromium-Activated Forsterite for Near-Infrared Excitation: Is Cr4+ the Laser Ion?", V Petricevic, S Gayen and R Alfano, Appl. Phys. Lett., **53**, (26), 2590 (1988)
[10] "Compositional Dependence of the Valency State of Cr Ions in Oxide Glasses", T Murata, M Torisaka, H Takebe and K Moringa, Journal of Non-Crystalline Solids, **220**, 139 (1997)
[11] "Spectroscopy of Cr^{4+} in MgCaBa Aluminate Glass", X Wu, S Huang, U Hommerich, B Aitken and M Newhouse, Chem. Phys. Lett **233**, 28 (1995)

Chapter 2

Theory

This theory chapter sets out the important ideas that are essential for an understanding of the work in this project. It covers not only theory behind the spectroscopy of transition metal ions but also some simple glass chemistry. Much of the first section, dealing with the spectroscopy for transition metals, introduces the key ideas of why the emission bands for transition metal ions are so broad (allowing the potential for large laser tunability) and also why quantum efficiency plummets when these ions sit in a glass host. Much of this transition metal theory is covered in further detail in spectroscopy textbooks[1,2]. Elements of this part of the chapter that are not covered by these recommended texts are given their own separate references.

2.1 The Fundamental Difference Between Rare Earths and Transition Metal Ions

The transition metal (TM) elements form a series in the fourth row of the periodic table between scandium and zinc. The electronic configuration of these atoms, which are often used as the active ion in lasers, consists of filled shells up to the 3p layer and then a partially filled 3d shell. It is because these optically active electrons lie on the outside, exposed and unshielded, that the crystal field of the ion's surroundings plays an integral role in setting the electron energy levels. It is also this interaction between the local crystal field and the ion that can be considered the source of the TMs' broad absorption and emission bands. This situation can be contrasted with the case of the rare earth ions whose active electrons, which are situated in the 4f level inside other filled shells, are shielded from the effects of local crystal fields. It is a consequence that crystal fields have little effect on rare earth energy levels and the transitions tend to be much narrower.

One important similarity between rare earths and TMs, however, is that the active electron transitions lie at optical or near infrared frequencies where dielectric hosts are transparent. This is obviously a vital characteristic for a solid-state laser.

2.2 Treatment of Energy Levels for Transition Metal Ions in Solids

The energy levels for a free ion are the eigenstates of the simplified time independent Hamiltonian:

$$\mathcal{H}_{fi} = \mathcal{H}_o + \mathcal{H}_e + \mathcal{H}_{so} \qquad 2.1$$

where,

- $\mathcal{H}_o$ is a spherically symmetric term which accounts for the Coulomb interaction between both the nucleus and the inner filled shells of electrons and the optically active electrons.
- $\mathcal{H}_e$ is the inter-electron interaction between the optically active electrons.
- $\mathcal{H}_{so}$ accounts for spin-orbit coupling for the optically active electrons.

These three terms are ordered according to the magnitude of their contribution where for small ions, like the transition metals, $\mathcal{H}_e > \mathcal{H}_{so}$.

Now when we consider the ion when it sits within a solid host, there is the additional consideration of the interaction of the host's crystal electric field with the ion. Three assumptions are made for the mathematical treatment of this static crystal field.

i) The system is essentially similar to the free ion but with an extra independent crystal field term.
ii) Only the nearest neighbouring ions of the host - the ligands - need be considered.
iii) Transition metal ions tend to sit in sites where the ligands have a specific site symmetry. E.g. trivalent transition metal ions such as Cr^{3+} and Ti^{3+} sit in octahedral sites.

So the Hamiltonian for a transition metal ion in a solid becomes,

$$\mathcal{H} = \mathcal{H}_o + \mathcal{H}_e + \mathcal{H}_c + \mathcal{H}_{so} \qquad 2.2$$

where $\mathcal{H}_c$ is the crystal field term. For transition metals, the magnitude of $\mathcal{H}_c$ is roughly that of $\mathcal{H}_e$ and the system may be thought of as being in either the strong or intermediate crystal field regime. This is pertaining to the order with which each term is considered, although both treat spin-orbit coupling as a perturbation. However, in advance of the crystal field being modelled and solving any equations, it is possible to get an excellent qualitative idea of the effect of the crystal field using the results of Group Theory.

Group Theory is a branch of mathematics that has powerful applications in many areas of Physics and Chemistry. In this problem, Group Theory allows an understanding of how eigenstates previously degenerate for a free ion will split under the interaction of the ligands' crystal field simply by considering the symmetry properties of the ion's environment. A very brief run through of the main ideas follows.

As described already, TMs have a tendency to sit in specific site symmetries. For instance, Cr^{3+} and Cr^{4+} sit in octahedral and tetrahedral sites respectively, which are shown in Figure 2.1. Both arrangements have a number of symmetry operations, such as rotations and reflections, which leaves the arrangement invariant, and the sets of these operations form mathematical groups. The axes of the rotation operations for the octahedral and tetrahedral sites are included on the diagram. In Group Theory every group has a character table which summarises many of the group's important properties. As an example, the octahedral group's character table is shown in Table 2.1. The columns of a character table are labelled by the different classes of symmetry for the group and the rows are labelled by the different irreducible representations for the group. Each element within the table corresponds to the character of a matrix whose dimensionality relates to which irreducible representation it belongs:

A ... (1x1) E ... (2x2) T ... (3x3)

An irreducible representation is the set of square matrices whose characters are shown in a row of the character table and they represent the symmetry properties of the whole group. A complete column shows the characters of a set of matrices that may be combined to form a reducible representation matrix for the class. The importance of a group's character

table is a reflection of the fact that the key results may be gained from these characters (which can be looked up) rather than the matrices themselves (which would have to be calculated).

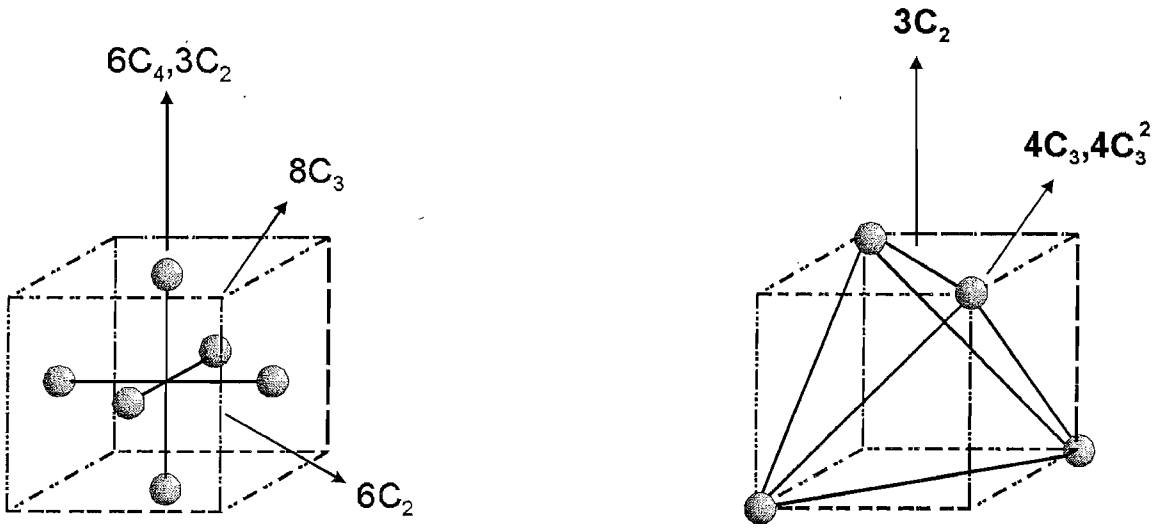

Octahedral Site *Tetrahedral Site*

Figure 2.1

	E	$8C_3$	$3C_2$	$6C_2'$	$6C_4$	Basis
A_1	1	1	1	1	1	$x^2+y^2+z^2$
A_2	1	1	1	−1	−1	xyz
E	2	−1	2	0	0	$(x^2-y^2, 3z^2-r^2)$
T_1	3	0	−1	−1	1	$(x, y, z); (R_x, R_y, R_z)$
T_2	3	0	−1	1	−1	(yz, zx, xy)

Table 2.1: Group Theory Character Table for the Octahedral Group

The connection between quantum mechanics and the theory of group representations can be stated in one sentence:

> *The eigenfunctions corresponding to an s-fold degenerate energy level of a Hamiltonian, $\mathcal{H}$, form a basis for an s-dimensional irreducible representation of the symmetry group of $\mathcal{H}$*

As a simple example of this idea, it is easiest to consider the case of a transition metal ion with a single electron e.g. Ti^{3+}. For the free ion and ignoring spin-orbit coupling at this stage, the five eigenstates with the 3d configuration will be degenerate. The question is what happens to them after the application of the octahedral crystal field when it sits in a solid.

Group Theory approaches this problem by using the five spherical harmonic functions for the 3d eigenstates as a basis to find a reducible representation for the octahedral group. This reducible representation is then decomposed to its constituent irreducible representations which are found to be E and T_2. Physically this is describing a situation where the five fold degenerate level has now split into one doubly degenerate level (labelled e) and one triply degenerate level (labelled t_2). This is useful information, but when it comes to finding the size of the splitting or which level has higher energy, Group Theory does not offer any labour saving shortcuts. The only way to do this is to solve the full Hamiltonian of Equation 2.2.

The simple model for the crystal field estimates the Coulomb interaction using point charges corresponding to the nearest neighbour ions,

$$H_c = \frac{1}{4\pi\varepsilon_0}\sum_i\sum_l \frac{Z_l e^2}{|\boldsymbol{R}_l - \boldsymbol{r}_i|}. \qquad 2.3$$

where $Z_l e$ is the point charge of a ligand, $\mathbf{R}_l$ is the position of a ligand and $\mathbf{r}_i$ is the position of the i^{th} electron. After substituting the $\mathcal{H}_c$ term with octahedral symmetry into Equation 2.2, the eigenstates and energy eigenvalues can be described. It is found that the five-fold orbital degeneracy of the 3d state is partially lifted by the crystal field interaction, yielding a doubly degenerate level and a triply degenerate level, confirming the Group Theory results. Detailed calculation gives the energy of the e orbital relative to the free ion energy

as 6Dq and that of the t_2 state as –4Dq: this gives a total splitting of 10Dq as shown in Figure2.2.

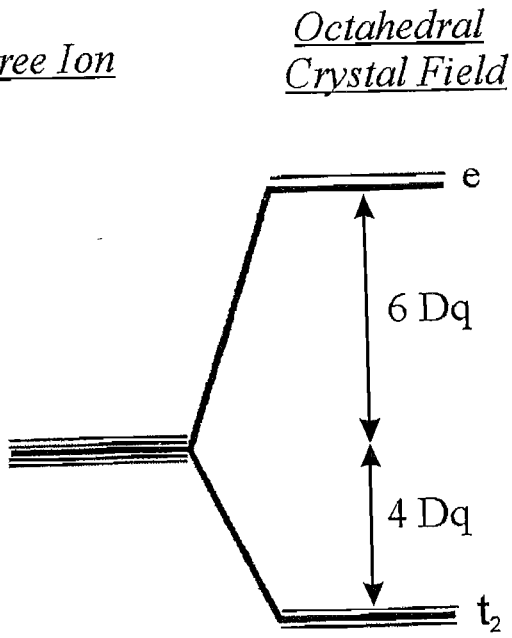

Figure 2.2: Octahedral Crystal Field Splitting

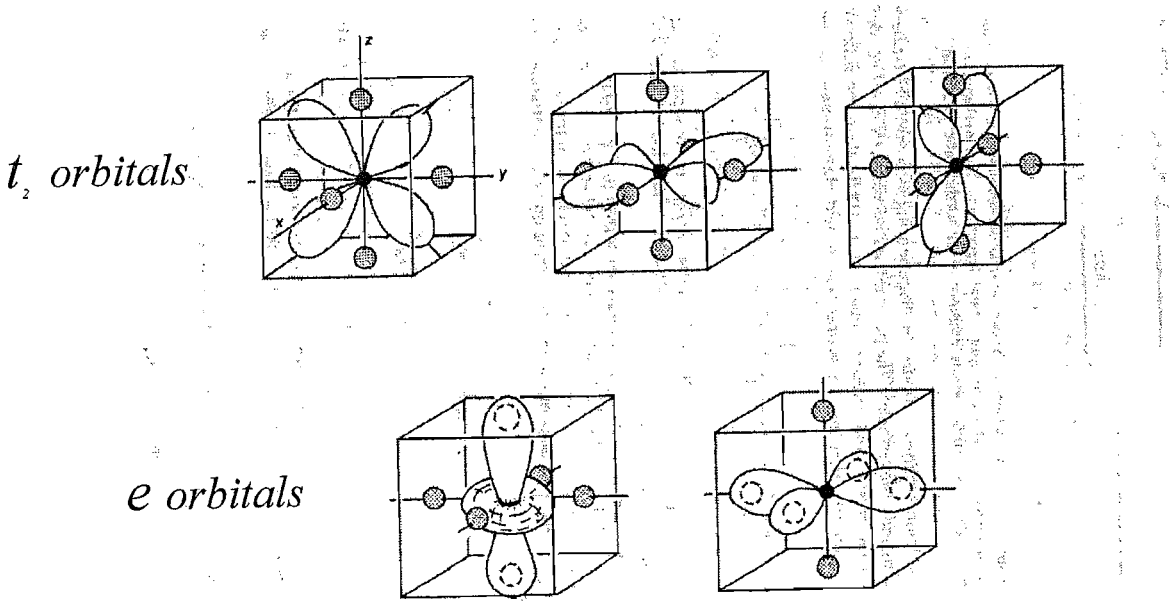

Figure 2.3: Octahedral Crystal Field Orbitals Formed from 3d Electron Wavefunctions

(Figure from "Optical Spectroscopy of Inorganic Solids" by B Henderson and G Imbusch, pg72)

The value of 10Dq is given by,

$$10Dq = 10\left(\frac{Ze^2}{6(4\pi\varepsilon_o)}\frac{\langle r^4\rangle_{3d}}{a^5}\right) \qquad 2.4$$

where Ze is the charge of the ligand ion, a is the separation between the ligands and the central ion, and $< r^4 >_{3d}$ is the expected value of the 3d electrons orbital radius to the fourth power. The fact that this crystal field model ignores the spatial extent of the ligands' charge, which can perhaps overlap with the wavefunction of the active ion, can lead to discrepancies between theory and experiment. Nonetheless, the model demonstrates the essential feature, namely that the strength of the crystal field increases rapidly with decreasing ion-ligand separation.

Intuitively, it seems to make good sense that the doublet has greater energy than the triplet. Figure 2.3 shows that the lobes of the wavefunction for the doublet are directed towards the negatively charged ligands, whereas the triplet lobes point in between the ligands.

2.3 Tanabe-Sugano Diagrams

In the more complicated situation where the TM ion has multiple 3d electrons, for instance Cr^{3+} has three, the electrons are distributed between the t_2 and e orbitals according to the Pauli principle. The energy levels for the various ion states are still very much dependent on the strength and symmetry of the crystal field but now also upon the Coulomb interaction between electrons in the 3d shell.

The effects of the interelectron interaction are characterised by three Racah parameters - A, B and C. The parameters are sufficient to quantify the interelectron interaction energy of multiple electron ions, and their values are dependent upon the particular ion-host combination. A simplification is that the Racah A parameter contributes only to a constant offset energy, and can be ignored when considering the relative energies of states. Additionally, although both B and C affect the relative energies of the states there is an approximate relation[3] between them such that the value of C/B generally lies between 4 and 5, giving just one independent parameter.

A very useful method of displaying the dependence of energy states upon the strength of the crystal field and the interelectron interaction was developed by Tanabe and Sugano[4]. They plotted E/B against Dq/B where E, the energy of a state, is relative to that of the lowest level. The value of Dq/B corresponds to the crystal field strength. Each Tanabe-Sugano diagram is specific to the site symmetry, the number of 3d electrons and to a lesser extent the exact value of C/B. Figure 2.4 shows the Tanabe-Sugano diagram for a $(3d)^3$ ion with octahedral symmetry such as Cr^{3+}.

There are many things to note about this diagram. Firstly, the nomenclature for the various levels e.g. $^4A_2$, ^2E, $^2T_1$ all correspond to irreducible representations for the octahedral symmetry group and the adjacent bracketed term describes how the 3d electrons are distributed between the t_2 and e orbitals. Energy levels, such as $^4T_2$, which have a strong dependence on the crystal field strength have electrons with e orbitals with energy 10Dq greater than the t_2. However, energy levels with solely t_2 orbitals are almost independent of the crystal field strength. The slight dependence upon Dq is due to configuration interaction between states with the same symmetry, for example inequivalent $^2T_1$ states are formed from $t_2^3$and t_2^2e configurations.

Efficient non-radiative decay within the excited states allows for luminescence only between the lowest excited state and the ground state. This makes the important levels $^4T_2$, ^2E and $^4A_2$. For hosts with high crystal fields (high field hosts), the ^2E level is the upper state. The luminescence is a very sharp line and is referred to as the R-line. For low field hosts, the $^4T_2$ level becomes the upper state and the emission is extremely broad due to a vibronic mechanism that is explained in the following section. It is these low field hosts that are of particular interest providing the potential for highly tunable lasers.

Glasses are low field hosts mainly because of their more loosely packed structure and the reduction of effective charge of the ligands through their covalent bonding. Primarily the network former determines the value of Dq in glass[7] and then smaller variations of crystal field depend upon the network modifiers. However, because of the disorder within glasses there will always be a continuous range of crystal fields owing to the range of sites[5].

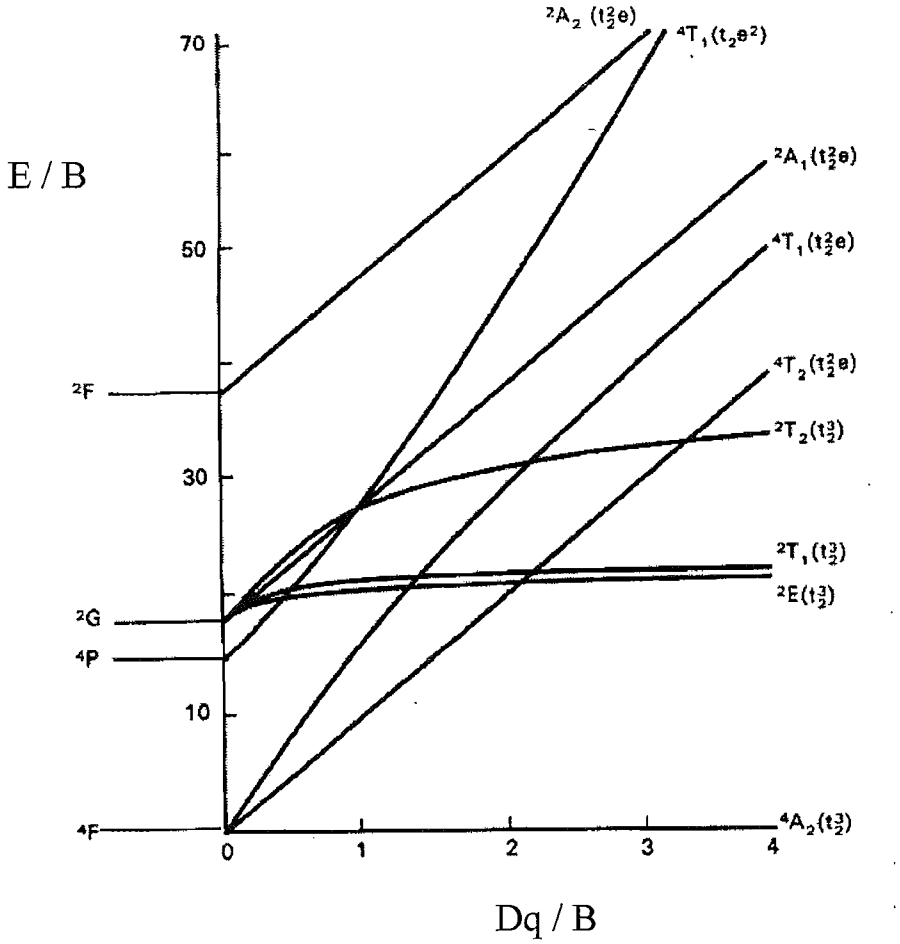

Figure 2.4: Tanabe-Sugano Diagram for a $(3d)^3$ Ion in an Octahedral Crystal Field with C/B = 4.8 as appropriate for Al_2O_3.

(Figure from "Optical Spectroscopy of Inorganic Solids" by B Henderson and G Imbusch, pg130)

2.4 Vibronic Coupling and Optical Lineshapes

For the TMs, the interaction of the unshielded 3d electrons with lattice vibrations has a profound effect upon the optical transitions. Vibronic coupling is the situation where the phonons are able to interact with the electrons, changing their energy, and it is this that is the origin for the broad optical transitions and the poor quantum efficiency for transition metals in glass. The coupling originates through the means of the crystal field, which can be seen when the full Hamiltonian for the active ion in a solid is written out,

$$\mathcal{H} = \mathcal{H}_{fi}(\mathbf{r_i}) + \mathcal{H}_{c}(\mathbf{r_i}, \mathbf{R_l}) + V_l(\mathbf{R_l}) + \Sigma\, \mathbf{P_l}^2/2m_l \qquad 2.5$$

where the first term is the Hamiltonian for the free ion, the second represents the vibrating crystal field, the third is the interion potential energy and the final term is the kinetic energy of the lattice ions. The terms are functions of the electronic coordinates $\mathbf{r_i}$ and the nuclear coordinates $\mathbf{R_l}$. Notice that the crystal field term contains both electronic and ionic coordinates, and it is this that couples together the electronic and ionic systems.

An excellent method to visualise this physical system is the Single Configuration Coordinate Model (SCCM) where the energy of the system is plotted against a single configurational coordinate describing the position of the surrounding lattice ions. Even if it is assumed that it is only the ligands that are pertinent to the problem, it would still require 18 parameters (3 dimensions x 6 ligands) to describe their collective position for an octahedral site. The SCCM, however, makes the problem more manageable simplifying this to just one coordinate, Q, which may be thought of as the ion-ligand separation in a totally symmetric 'breathing mode'. The electrons sit in a Morse potential well that the model assumes to be a harmonic potential at the relevant configurations close to the well minimum. The problem now consists of a quantum harmonic oscillator for each electronic level; only discrete energy levels are allowed, where $E = h\nu(n + \frac{1}{2})$, and the wavefunctions will be Hermite polynomials. Because the electronic and lattice systems are coupled together, the initial and final states for the electronic transitions are the electron-plus-lattice states, $\psi(\mathbf{r_i},\mathbf{R_l})\chi(\mathbf{R_l})$, called Born-Oppenheimer products.

The primary thing to note is that the ground state equilibrium configuration $Q_0^{(a)}$ need not be the same as that of the upper state $Q_0^{(b)}$. This describes a difference in the electron-lattice coupling for the electronic levels brought about by the different shape of the 3d are directed towards ligands and are more strongly coupled to electron spherical harmonics. Referring back to Figure 2.3, it can be seen that the e orbitals are directed towards ligands and are more strongly coupled to the lattice than the t_2 orbitals. One of the consequences of this change in coupling is that the average TM ion-ligand separation changes with the electronic state.

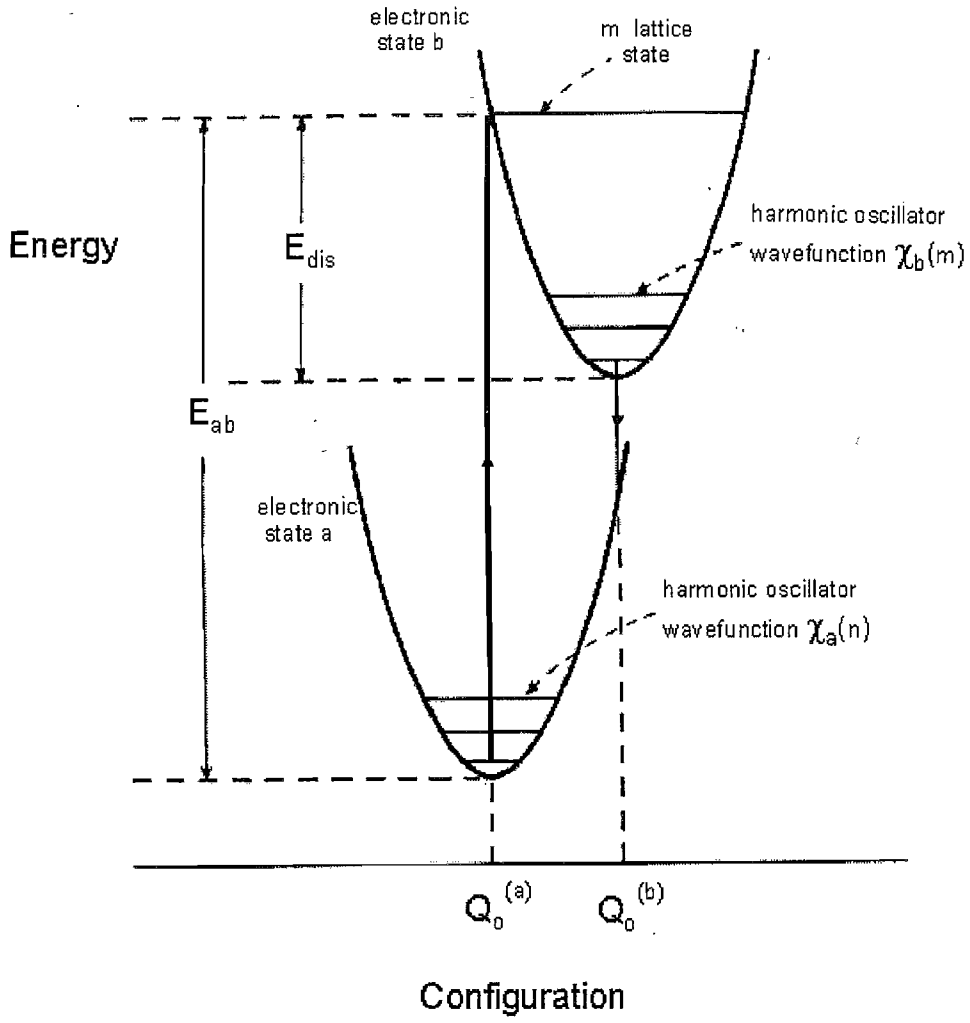

Figure 2.5: The Single Configuration Coordinate Model

The difference in electron-lattice coupling between the ground and excited state is characterised by the Huang-Rhys factor,

$$S = E_{dis}/h\nu \qquad 2.6$$

where $h\nu$ is the quantum of energy of the breathing mode. Assuming that the two levels are identical parabolas and $h\nu >> k_BT$ so that the higher lattice states within the ground state are not occupied, it is possible to calculate the absorption lineshape. The strength of the transition is proportional to the square of the overlap integral between the upper and

lower lattice states $< \chi_b(m) \mid \chi_a(n=0) >$.

$$I_o \sum_m \frac{\exp(-S)S^m}{m!} \delta(E_o + m\hbar\omega - E) \qquad 2.7$$

This equation is a Pekarian function and describes a series of weighted delta functions separated by the energy of the breathing mode phonon. Figure 2.6 shows the predicted absorption for various values of electron-phonon coupling. The points to note are firstly that the lowest energy line is the zero phonon line where n=0 and m=0 so that no phonons have been created during the absorption. Secondly, the most intense and therefore most probable transition corresponds to a vertical line on the SCCM diagram. This is the Frank Condon transition and may be explained classically by the fact that during the transition the electrons change state so fast that the nuclei do not have a chance to move. Finally the greater the electron-phonon coupling, the broader the transition and the more the Pekarian's envelope appears gaussian-shaped.

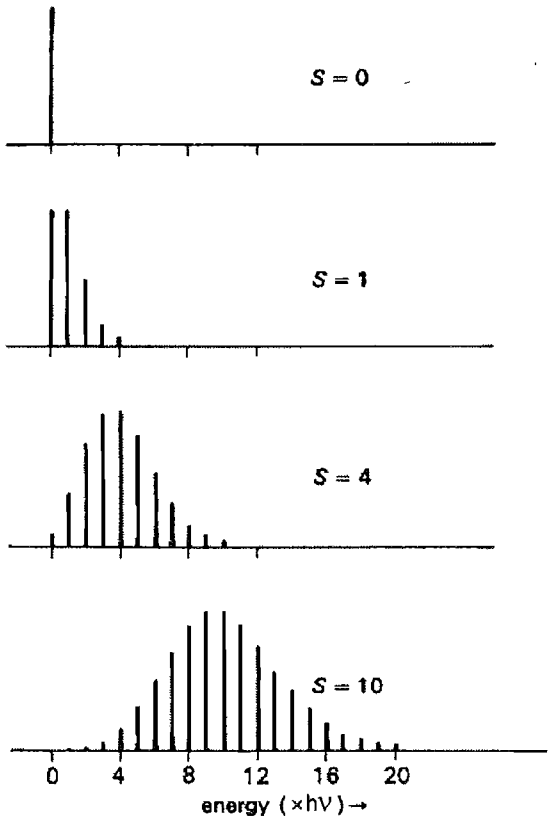

Figure 2.6: Pekarian Function

(Figure from "Optical Spectroscopy of Inorganic Solids" by B Henderson and G Imbusch, pg202)

Many different broadening mechanisms (as described later), however, make a series of delta functions unrealistic. Figure 2.7 shows how absorption and emission transitions on the SCCM lead to the real lineshapes for crystals. In fact, the broadening mechanisms for transition metals within glasses are so strong that none of the original Pekarian structure can be observed at all. Providing the energy levels for the excited and ground states are the same shape, the absorption and emission lineshapes should be mirror images of one another. The energy loss between the two bands is known as the Stokes shift and is due to the non-radiative decay between lattice states. It is this vibronic scheme that has provided the mechanism for many tunable 4 level lasers.

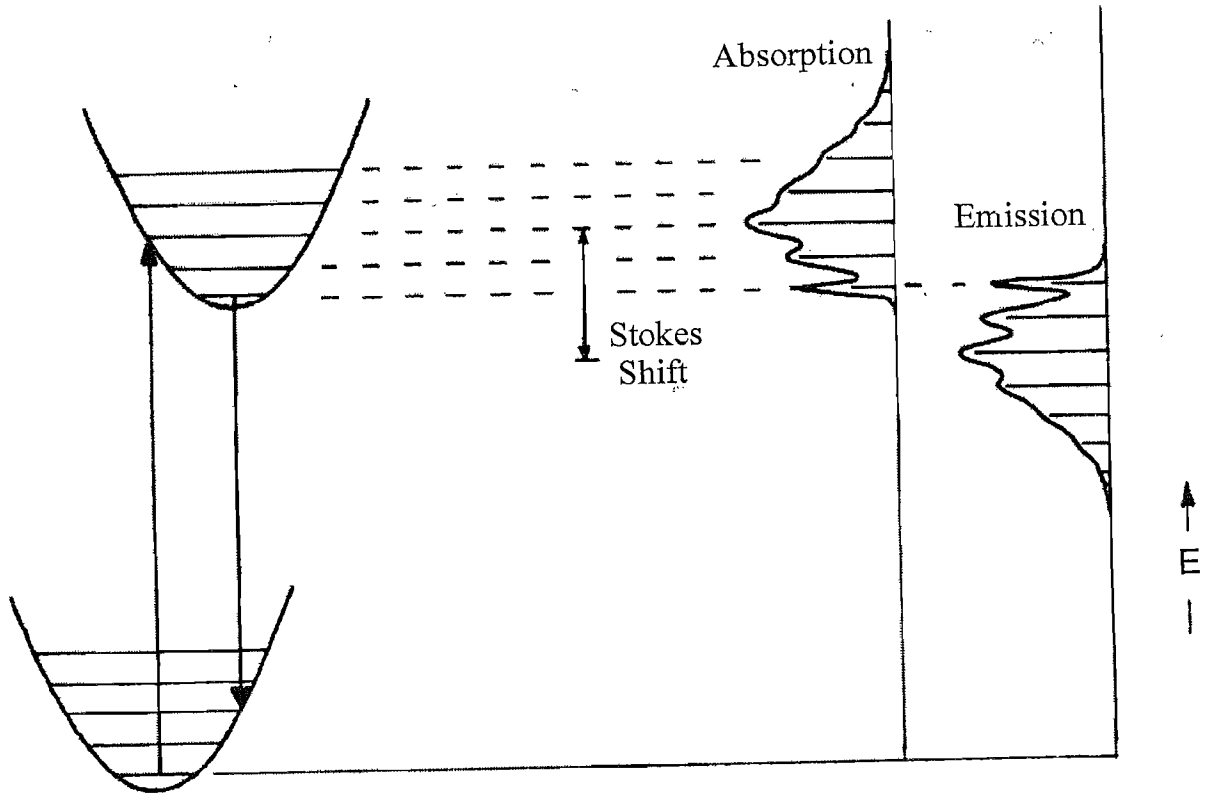

Figure 2.7: Low Temperature Absorption and Emission Transitions

(Figure from "Spectroscopy of Solid-State Laser-Type Materials" ed. B Di Bartolo, pg158)

2.5 Broadening Mechanisms

It has already been explained that the process of vibronic coupling allows lattice vibrations to interact with an electronic transition to create modulation sidebands. The reason that the predicted Pekarian function is not observed in reality is due to a number of line broadening mechanisms that can be separated into homogeneous and inhomogeneous.

Homogeneous Broadening Mechanisms:

- Lifetime Broadening – The origin of this is not so much the finite radiative lifetime but the extremely short phonon lifetime of the final state of an optical transition.
- Dephasing Time – This refers to the elastic scattering of phonon collisions with atoms, which causes a subtle change in the transition frequency through the means of a crystal field interaction. Intrinsically, the ability to predict the phase is decreased, reducing the coherence time and broadening the transition.
- Range of Phonon Modes - The SCCM assumes solely the breathing mode, which is unrealistic. Figure 2.8 shows the normal modes of an octahedral complex corresponding to phonons of different frequencies. The normal modes are classified according to their irreducible representation in the octahedral symmetry group.

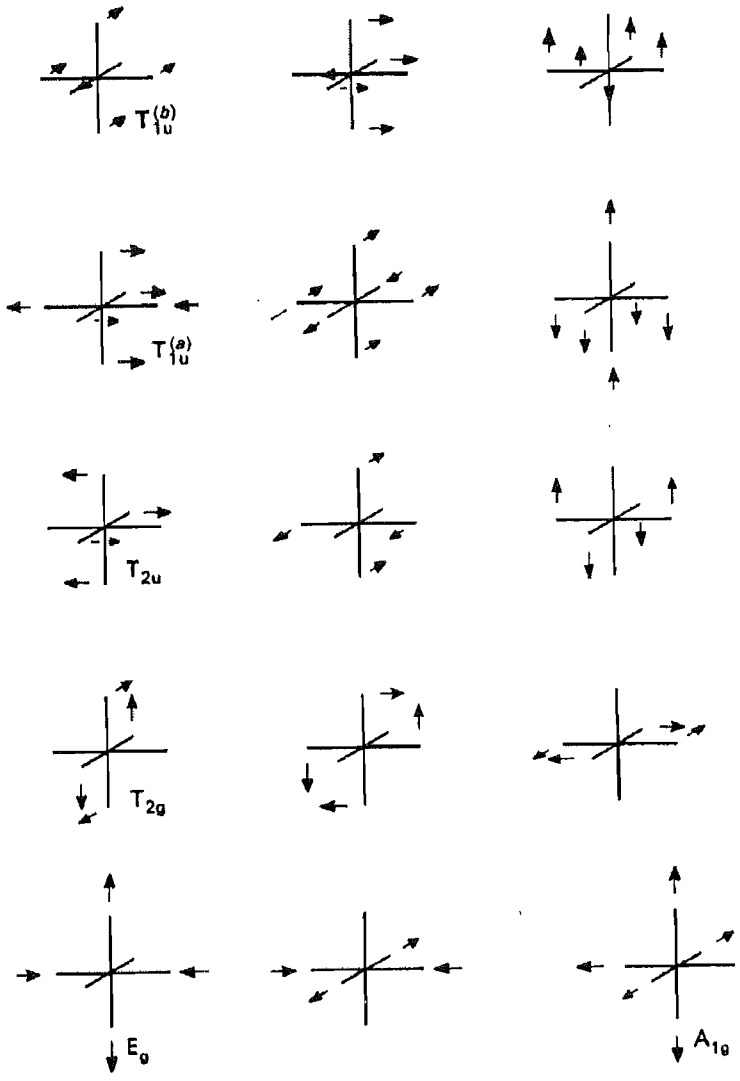

Figure 2.8:

Normal Modes of Distortion for the Octahedral Complex

(Figure from "Optical Spectroscopy of Inorganic Solids" by B Henderson and G Imbusch, pg192)

Inhomogeneous Broadening Mechanisms:

The disorder within the amorphous host leads to a continuous range of sites for the TM ion. A range of Dq can be created if different glass sites[5] have various ligand-central ion separations. It is also possible to imagine a range of S since the electron wavefunctions will overlap to different degrees with the ligands'. The general effect of this is to change the position of the parabolas of the SCCM relative to one another as shown in Figure 2.9.

Figure 2.9: The Effect of Variation in Crystal Field Strength and Electron-Lattice Coupling

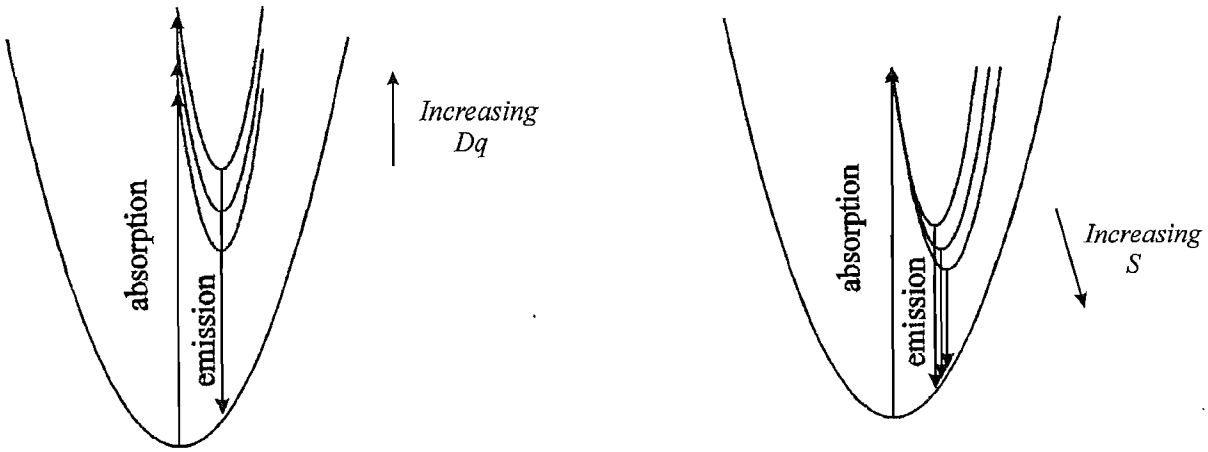

2.6 Low Radiative Quantum Efficiency for Transition Metals in Glass Hosts

Vibronic coupling, whilst being the dominant mechanism providing the broad emission bands, also has the disadvantage of greatly reducing the radiative quantum efficiency (QE). Many Cr^{3+} doped crystals have room temperature QEs close to 100%[6] whereas the majority of Cr^{3+} doped glasses have QEs much less than 5%[7]. Since any laser's pump threshold is in part determined by the QE, it is important when selecting a host to strike a balance between the maximum possible tunability and an acceptably low threshold. This

thermal quenching of luminescence for TMs in glass hosts comes about through an increased non-radiative rate but there is no correlation between values of QE and the maximum vibrational frequency of the glass[8], as in the case of rare earth ions. An understanding to why the radiative quantum efficiency plummets when the TM's host is a glass is most easily achieved by considering the Single Configurational Coordinate Model.

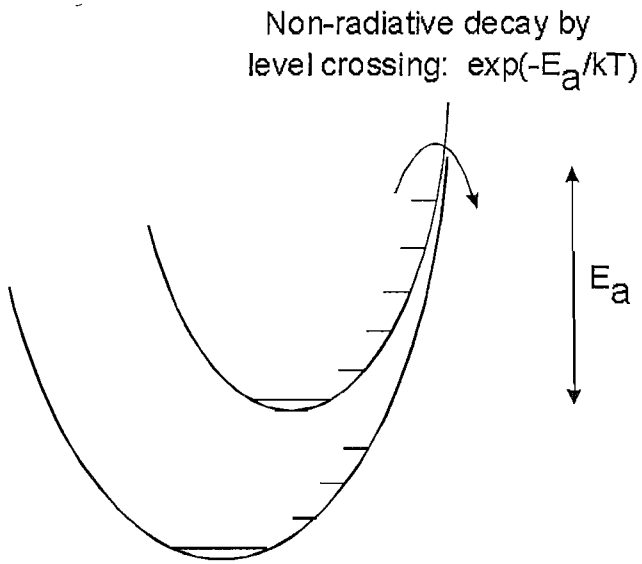

Figure 2.10: Non-Radiative Decay Mechanism for Transition Metals within Glass

Glasses have a much larger electron-lattice coupling than crystals, which is evidenced by their large Stokes shifts[8]. There are two good explanations for this. Firstly, the bonding between ligands and Cr in glass will have covalent character leading to more wavefunction overlap and increased coupling. Secondly, glass is a loose structure and when the electron is excited to the $^4T_2$ state, the Cr ion no longer has the same requirement for six-fold coordination. The local ionic complex can adjust to a different configuration of lower energy[8,9] with greater facility than in crystals and this has the effect of increasing S. With larger electron-lattice coupling, the upper electronic state's parabola gets translated across to bigger values of Q. Additionally, glasses will generally have weaker crystal field strength than crystals due to their more open structure. The important consequence of this increased Huang-Rhys factor and reduced Dq is that the two parabolas (not necessarily

similar curvatures) will pass close together and may even cross. Absorption of phonons may temporarily excite an electron, over an activation energy E_a, so that it can tunnel or maybe simply cross between parabola without emitting a photon, lowering the radiative quantum efficiency. Glass hosts that have relatively small electron-lattice coupling and relatively high crystal field strengths will have a large activation energy and experience less non-radiative decay for a given temperature. As the temperature increases, there will be increased phonon occupancy and the probability of level crossing will increase, following a Boltzman-like relationship.

Another aspect of this concept is that the range of different Huang-Rhys factors and crystal field strengths experienced by separate sites within a glass (see Figure 2.9) means that the degree of non-radiative decay will be site dependent.

2.7 The Effect of Distortions

Even in crystals, the assumption that the TM ion is surrounded by ligands in perfect octahedral symmetry is incorrect. This is even more the case for glass hosts, where the disorder produces static distortions in which the mean position of the ligands forming the crystal field deviates from the perfect octahedral arrangement. Distortions are important because they can affect the position of energy levels and the strength of transitions. However, since the distortions tend to be relatively small they are normally treated as perturbations. The distortions are conveniently categorised as even or odd parity according to whether inversion symmetry is maintained (even parity) or destroyed (odd parity). Odd and even parity distortions bring about quite different effects upon optical transitions.

2.7.1 Odd Parity Static Distortions

According to Time Independent Perturbation Theory, 3d – 3d electric dipole transitions are not allowed and the oscillator strength is zero. This is the Laporte selection rule. However, the introduction of the ion into a solid results in the mixing of free-ion wavefunctions such that oscillator strength is induced but may still be quite weak. Odd parity distortions, although having negligible effect on the energy level positions, act to increase the strength of the transition. The odd parity distortions lead to odd parity terms in the crystal field. This in turn allows odd parity wavefunctions to be mixed into the d functions and electric dipole transitions become stronger, substantially increasing the oscillator strength.

This idea has the potential to be very important in systems where there is significant non-radiative decay. If, by strengthening the effect of odd parity distortions, the non-radiative component in the measured lifetime can be made relatively less significant, then the $\sigma_e\tau$ product can be increased.

It should be mentioned that Cr^{4+} sitting in tetrahedral sites will not be susceptible to the effects of odd parity distortions in quite the same way, since the T_d arrangement itself does not possess inversion symmetry. Consequently, the crystal field Hamiltonian has both even and odd parity terms and this is the reason why TM ions sitting in T_d symmetry have an oscillator strength at least one order of magnitude higher than those sitting in O_h symmetry.

2.7.2 Even Parity Static Distortions

Even parity distortions are responsible for further splitting the energy levels that form in the octahedral crystal field. The distortion may be thought of as a perturbation to the basic O_h solution and can be treated either by Group Theory (for a qualitative solution) or analytically using the crystal field Hamiltonian with the symmetry of the distortion. Even parity distortions may be thought of as an additional inhomogeneous broadening mechanism.

2.7.3 Dynamic Distortions

The vibration of the ligands can modulate the crystal field away from pure octahedral symmetry, causing what is known as dynamic distortions. These have similar effects upon optical transitions as the static distortions. The normal modes of distortion of the octahedral complex were shown in Figure 2.8. Coupling to the odd parity T_{1u} or T_{2u} dynamic distortions removes the inversion symmetry and, as in the case of odd parity static distortions, the oscillator strength increases, becoming phonon assisted. This effect will be temperature dependent and will rely upon the mean thermal occupancy, n, of a vibrational mode:

$$n = \frac{1}{\exp(h\nu/k_BT) - 1} \qquad 2.8$$

The intensity of the transition can be shown to increase as $\coth(h\nu/k_BT)$.

A large element of this project was the fabrication of bulk glass samples and optical fibres. Decisions about glass compositions and fabrication techniques had to be made which were based upon some simple concepts of glass technology. The rest of this chapter briefly covers some glass chemistry that will aid the readers understanding of the rest of the thesis. These ideas are covered in greater detail in a number of texts[10,11,12].

2.8 The Definition of Glass, and its Manufacture

There are several useful definitions of glass and how it differs from crystalline solids[13]. Firstly, glasses, unlike crystals, exhibit no long-range order but do have short-range order over a scale of about 1nm. Secondly, there will be no discontinuities in physical properties, such as volume or entropy, during the transition from liquid to solid glass.

Whilst it is generally true that any crystalline solid can be made amorphous if it is cooled sufficiently rapidly, starting from above its melting point, there are actually many techniques to form glasses starting from solid crystals, liquid melts or gases. From the solid phase, amorphous materials can be created by radiation damage. One important example of glass manufacture from the gaseous phase is the Modified Chemical Vapour Deposition (MCVD) technique that is used to fabricate almost all commercial optical fibres. However, the soft glasses examined in this project were fabricated from materials in the liquid phase, which were then quenched rapidly to form glass.

2.9 The Glass Transition

Glasses show a decrease in volume as they are cooled from high temperature through a super-cooled liquid region until the glass transition (T_g) is reached where the coefficient of thermal expansion changes. A glass' volume-temperature curve (see Figure 2.11) is continuous, unlike that of crystals, but there is a kink at T_g, indicating a second order phase transition. The glass transition is the intersection between the glass solid and glass liquid phases and its temperature is not a constant for the material but increases with an increasing cooling rate. The lack of a discontinuity for glass is due to their viscoelastic property[13] where the viscosity of the glass liquid phase increases rapidly upon cooling. At the transition, the viscosity becomes so great that the migration of ions required for crystallisation has such a large time constant that crystallisation is prevented.

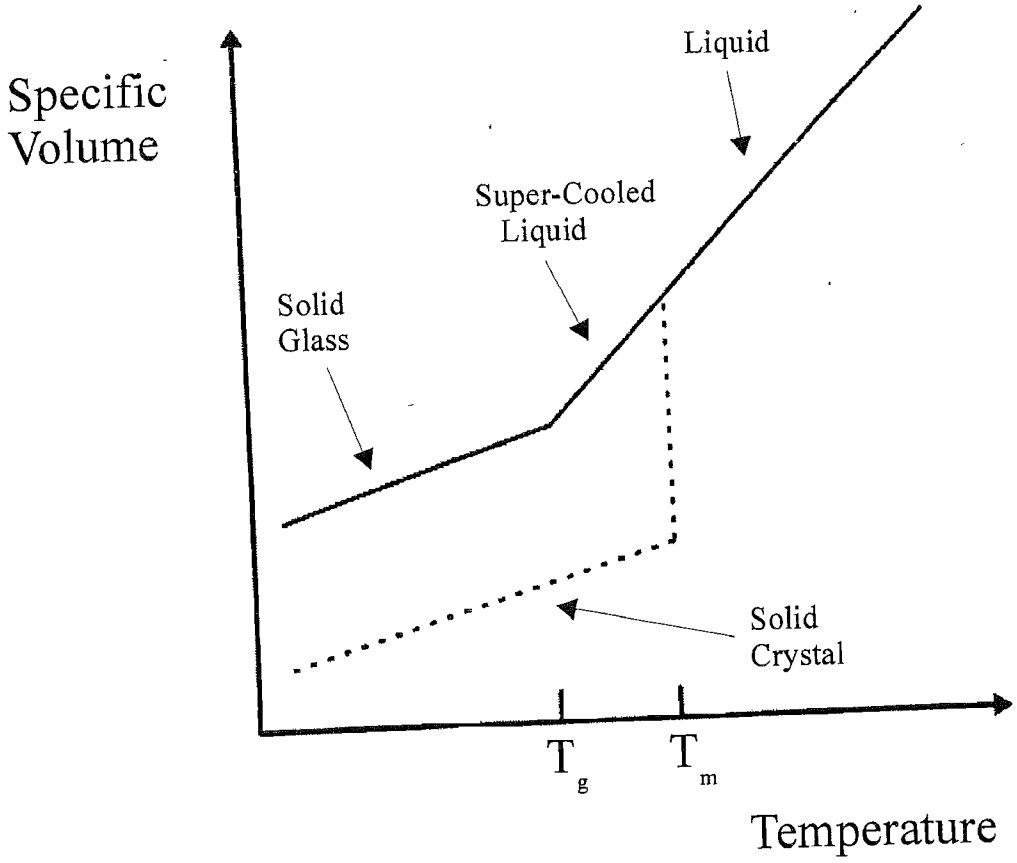

Figure 2.11: Relation Between the Glassy, Liquid and Crystalline States

If the thermodynamic variable of entropy for the system were considered while the material was being cooled, the graph would look similar to the volume-temperature graph in Figure 2.11. The excess entropy in the formation of the glass when compared to the crystal corresponds to disorder frozen into the glass from the liquid phase. The free energy has not been minimised and the glass is not in equilibrium. However, the glass will remain disordered because of the high viscosity when it is cool, making the phase metastable.

When a glass is quenched at different rates, many of its physical properties will change. The larger the cooling rate, the lower the glass' density (due to a more open and disordered ionic configuration), the lower the viscosity and the lower the refractive index.

2.10 Crystallisation and Glass Stability

Crystallisation is a two-stage process. It is initiated by the nucleation of nanocrystals and then followed by crystal growth throughout the glass matrix. As shown by Figure 2.12, the rate of nucleation and growth of crystals is temperature dependent. When a glass is quenched during its fabrication, it will first pass through the growth peak and then the nucleation peak. Since this is the wrong order for effective devitrification, what becomes important is the overlap between the two peaks producing a danger region that must be passed through as quickly as possible during quenching. However, in practice there will normally be plenty of nucleation centres already in existence; these might be small impurities, bubbles within the glass or dust on the surface. In this case it is only the rate of growth that is important.

Figure 2.13 shows the rate of growth for a soda-lime-silica glass. The rate of growth falls to zero at the melting point and has negative values at higher temperatures. The fall in the rate of growth at lower temperatures occurs because the increasing viscosity prevents the migration of ions needed for crystal growth. The consequence of this is that stable glasses, which are less prone to devitrification, have high viscosity that curtails the extent of the growth peak towards lower temperatures.

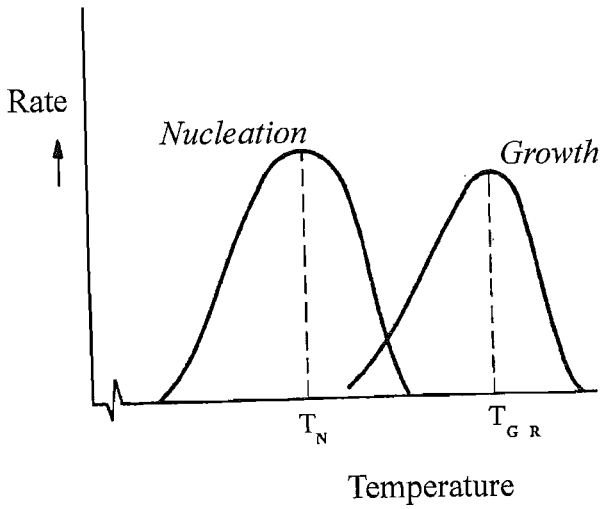

Figure 2.12: Nucleation and Growth Rate

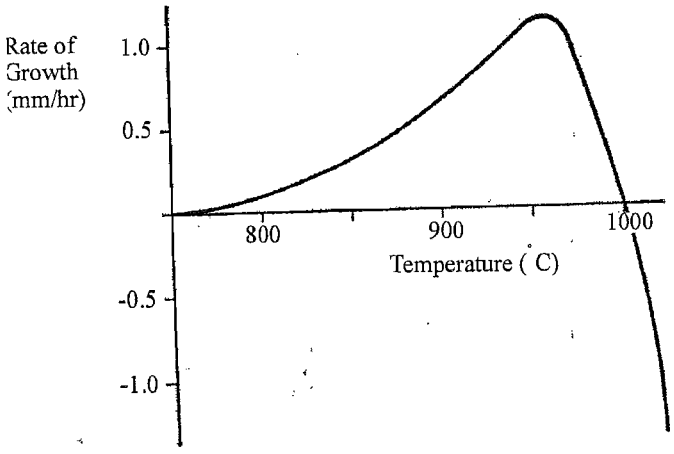

Figure 2.13: Growth Rate (for Na_2O-3CaO-SiO_2)[14]

(Figure from "Glass" by G O Jones, pg 30)

2.11 Formers, Modifiers and Intermediates

These terms refer to the role various cations play in the structure of a glass. In oxide glasses, examples of network formers are Si^{4+}, P^{5+}, Ge^{4+} and B^{3+}. They are all highly charged, the bonds are in part covalent in character, therefore directional and their coordination is low. These properties lead to increased viscosity and they can form stable glasses on their own, e.g SiO_2. Network modifiers act to break up the network and examples of these cations are Li^+, Na^+ and Ca^{2+}. These all have small charges, bond ionically and generally have a higher coordination number than formers. Lastly, intermediates (such as Al^{3+} and Zn^{2+}) are cations that can behave either as formers or modifiers depending upon the composition.

The addition of network modifiers can often have an important and prominent effect on the characteristics of a glass. Increasing the modifier concentration has the following effects:

- Increases glass density – the modifiers tend to fill in the holes within the network.
- Decreases the viscosity – although the glass is more tightly packed with atoms, they are less tightly braced in three dimensions.
- Increases the solubility of dopant impurities within the glass.

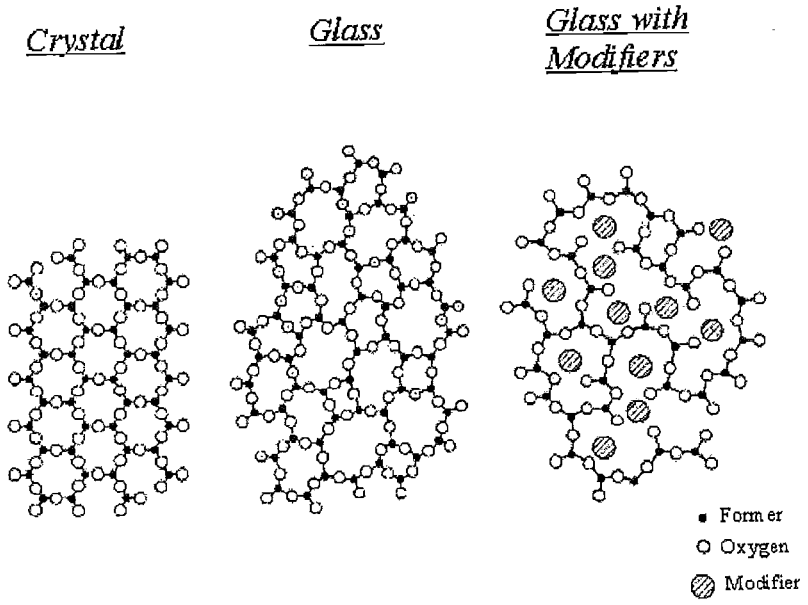

Figure 2.14: Diagramatic 2D Structure of Crystal and Glass

(Figure from "Glass" by G O Jones)

2.12 Annealing

During the process of quenching, undesirable mechanical stresses between adjoining layers are frozen into the glass due to different rates of cooling. This renders the glass extremely brittle and difficult to cut and polish. To make the glass more robust, a post-thermal treatment can be carried out called annealing. The glass is heated up and held close to T_g where the viscosity is low enough for the stresses to dissipate. Afterwards, the glass is cooled extremely slowly (~2°C /min) so no further stresses may develop.

Another advantage of the annealing process is to ensure the uniformity of physical properties, such as density and refractive index, that would have otherwise been affected by different rates of cooling.

---

[1] "Optical Spectroscopy of Inorganic Solids", Chapters 2,3 and 9, B Henderson and G F Imbusch, Oxford (1989)

[2] "Specroscopy of Solid-State Laser-Type Materials", ed. B Di Bartolo, Plenum Press (1987)

[3] S.Sugano, Y Tanabe and H Kamimura, "Multiplets of Transition Metal Ions in Crystals", Academic, London (1971)

[4] Y Tanabe and S Sugano, J. Phys. Soc. Japan, **9**, 753 (1954) and **9**, 766 (1954)

[5] "Disorder and the Non-Radiative Decay of Cr^{3+} Doped Glass", M Yamaga, Y Gao, K O'Donnell and B Henderson, Journal of Luminescence, **53**, 457 (1992)

[6] "Quantum Efficiencies of Chromium Doped Glasses", M J Payne and N Lowde, Physics and Chemistry of Glasses, **32**, (5), 222 (1991)

[7] "Spectroscopy and Photokinetics of Chromium (III) in Glass", L J Andrews, A Lempicki and B McCollum, J. Chem. Phys., **74**, (10), 5526 (1981)

[8] "On the Quantum Efficiency of Chromium Doped Glasses", G Imbusch, T Glynn and G Morgan, Journal of Luminescence, **45**, 63 (1990)

[9] "Near Infrared Emission at 1.35μm in Cr Doped Glass", U Hommerich, H Eilers, W Yen, J Hayden and M Aston, Journal of Luminescence, **48 & 49** 574 (1991)

[10] "Glasses and the Vitreous State", J Zarzycki, Cambridge University Press (1991)

[11] "Amorphous Materials", R Elliot, Wiley (1990)

[12] "Glass", G O Jones, Chapman and Hall (1971)

[13] "Gallium Lanthanum Sulphide Based Glasses for Mid-Infrared Optical Fibres" PhD Thesis by D Brady, University of Southampton (2000)

[14] "Glass", G O Jones, Chapman and Hall (1971) pg30

Chapter 3

Spectroscopic Techniques

The range of experimental techniques used in this project has been very broad. Details of the fabrication methods employed and experiments investigating the fibre samples are left to later chapters. This chapter, though, provides the details of the equipment and methods used in the spectroscopic characterisation of the bulk samples.

Absorption spectra, fluorescence spectra, upper state lifetimes and radiative quantum efficiency were the key characteristics investigated. The fluorescence tended to be weak, have extremely broad spectral emission and fast decay. These characteristics imposed tough requirements for the choice of apparatus. Because both Cr^{3+} (700-1100nm emission) and Cr^{4+} (0.8-1.7μm emission) were investigated in this project, different types of detector were needed in each case.

3.1 Absorption

The absorption spectra of the bulk samples were investigated with a commercial spectrophotometer (Perkin-Elmer Lambda 9). This was a white-light dual-path instrument in which the polished bulk sample was placed in one beam. The dual light path configuration allowed for automatic correction for the spectral response of the detector and the source. The samples were polished on two parallel sides and were 3mm thick. Absorption cross-sections could be calculated from knowing the dopant concentration of the sample.

3.2 Fluorescence Spectra

The emission spectra in this project were recorded using the experimental setup shown in Figure 3.1. The pump lasers used to pump the Cr^{3+} samples were an Ar ion laser running on a single emission line (488nm) and a He Ne laser (633nm). For the Cr^{4+}

samples, the excitation source was an Ar ion pumped Ti sapphire laser with a wavelength range of 700nm to 860nm.

The fluorescence was collected and focussed into a monochromator, after which the signal was detected. In the case of the Cr^{3+} samples, the spectra were recorded by a liquid nitrogen cooled CCD array (Princeton Instruments LN-CCD-512TK). This device required no pump modulation, incorporated its own monochromator (Acton Spectrapro 275) and the Si material was sensitive from 400nm to 1μm. The liquid nitrogen cooling acted to reduce the thermal noise for the CCD and the electronics. Narrowing the entrance slits to the device improved the spectral resolution but reduced the detected signal. However, the finite size of the individual CCD pixels limited the resolution when narrowing the slits beyond a certain point. The problem of pump light and its higher diffracted orders was removed by using an appropriate long-pass filter in front of the slits. The beauty of the CCD array was that it could collect all the spectral information in parallel without needing a time consuming scan to obtain a satisfactory signal to noise ratio.

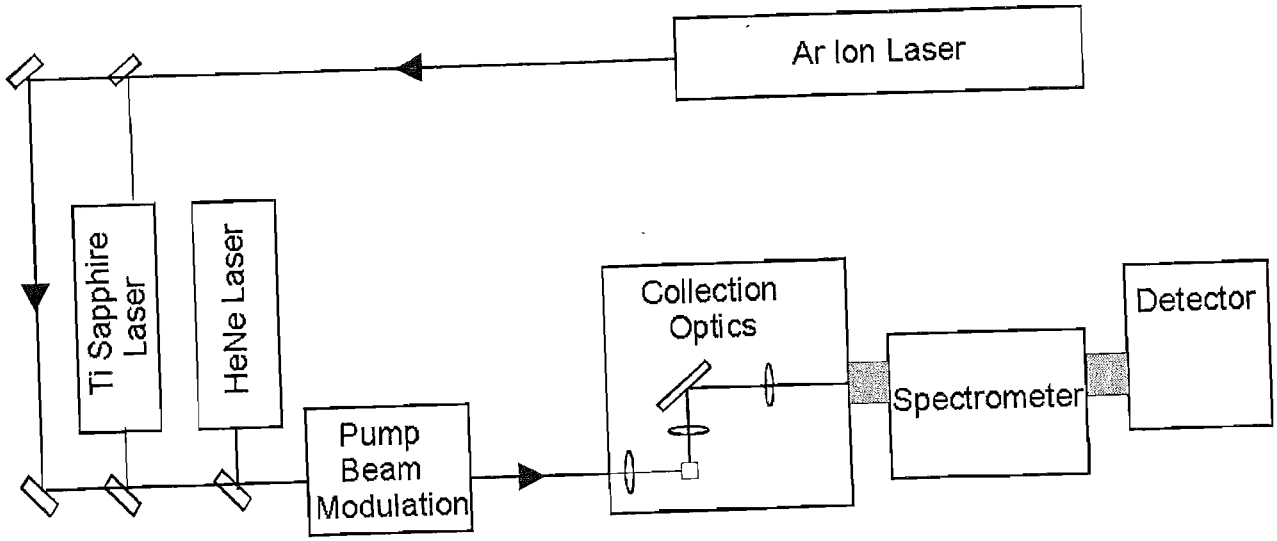

Figure 3.1: Block Diagram for the Experimental Arrangement Used for Fluorescence Measurements

For the case of the Cr^{4+} samples, the fluorescence exiting the monochromator (Chromex 250 IS/SM) was focussed onto an indium gallium arsenide (InGaAs) diode detector (New Focus 2011). The InGaAs diode detector had a wavelength response of 800nm to 1.9μm. The pump beam was mechanically chopped and an electrical signal was sent to the lock-in amplifier so that noise with a differing frequency to the modulation rate could be filtered out. A spectrum was created by the computer controlling the monochromator, scanning through the wavelengths and recording the data. For both these experiments, corrections had to be made for the spectral response of the detector and the collection optics.

3.3 Fluorescence Lifetimes

3.3.1 Experimental Technique

The decays were recorded with the same general scheme shown in Figure 3.1. The modulation technique was chosen so that the pump beam turn off was short compared to the lifetime being measured. Using a mechanical chopper with a focussed pump beam (two x10 microscope objectives), a turn off time (90% to 10%) of 2μs could be achieved; this was used for the Cr^{3+} samples with lifetimes of about 35μs. For the Cr^{4+} samples with much quicker lifetimes of about 1μs, a quicker turn off was required. Here, an acoustic-optic modulator with a focussed pump beam was used which could achieve a turn off of about 80ns.

Again, the type of detector depended upon the wavelength of emission. The CCD array could not be used for decays since it is not intended for temporal resolution. Instead a photo-multiplier tube (PMT) (Hamamatsu R3236 with S1 photocathode) was used for the Cr^{3+} samples. This device was sensitive between 300nm and 1.1μm and had a time response of about 10ns. It was configured for single-photon counting and was thermoelectrically cooled to limit thermally induced noise. The signal from the PMT was amplified with a preamplifier (Stanford SR445) and then recorded with a multi-channel scaler (Stanford SR430). Because there was no shortage of optical signal and the PMT was so sensitive, the monochromator could be retained in the setup to investigate how the lifetime depended upon emission wavelength.

The multi-channel scaler (MCS) can discriminate against PMT thermionic dynode noise and only counts the pulses large enough to represent a genuine photon event at the photocathode, after the laser has turned off. This device has the ability to count current pulses that corresponds to the number of photon events in a user-defined time, the bin width. After this bin width time has elapsed, the MCS starts counting the number of events in the subsequent bin and so on. The total length of time the MCS counts for after the trigger is simply the product of the number of bins and the bin width. The MCS was triggered by a portion of the modulated laser beam incident upon a photodiode and the counting process was averaged over many repeated pump cycles.

Figure 3.2

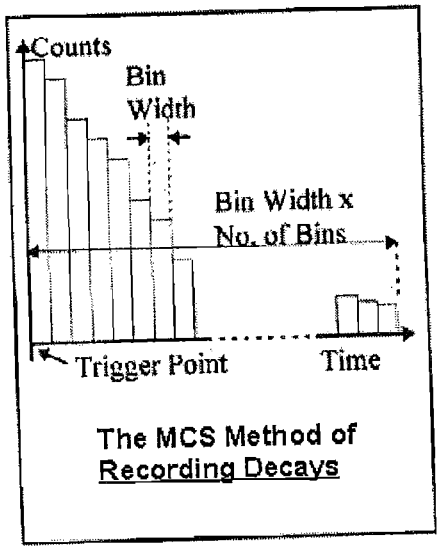

As for the Cr^{4+} samples, much of the weak IR fluorescence (0.8-1.7μm) was beyond the sensitive range of the PMT. However, the InGaAs diode, although having variable gain with an integrated transimpedance amplifier and a very small diameter (300μm) for speed of response, did not have the required sensitivity for a satisfactory signal to noise ratio. Instead, the PMT was used to detect the signal albeit only the short wavelength emission below 1.1μm. In order to maximise the signal strength, the monochromator was removed from the setup and a long-pass filter was used block to block out the pump light.

3.3.2 Fitting the Non-Exponential Decays

The decay profiles were treated with software performing non-linear least-squares fitting and were found to be highly non-exponential. Non-exponential decays are found frequently in the study of both rare earth and transition metal spectroscopy, and it is

commonly acknowledged that accurate fitting and characterisation of these profiles is difficult.

The problem of settling on a single exponential for a non-exponential decay is that the fit can be very poor and accounts badly for the slower radiative contribution at the end of the profile[2]. Importantly, the characterisation of the fit can significantly depend upon the length of the profile taken. For instance, it was found fitting to five e-folds of the Cr^{3+}:LLS decays instead of using 10 e-folds could change the characterised lifetime by 10%. It follows that errors and false comparisons can easily be brought about, making single exponentials poor functions to fit non-exponential decays. Often in the literature, 1/e fall times are taken as a measure for these decays. However, this again takes no account of the more slowly varying latter part to the decay and gives no idea to the degree of non-exponentiality.

One of the better decay characterisations used in the literature is to take the average lifetime:

$$\tau_{av} = \frac{\int_0^\infty tI(t)dt}{\int_0^\infty I(t)dt} \qquad 3.1$$

This method does take into account the latter part of the decay but gives no idea to the degree of non-exponentiality, which is not ideal when comparing decays.

In this thesis, the stretched exponential function (see Equation 3.2) has been used to fit to the decays. Figure 3.3 shows a typical decay. Not only did this function provide excellent fits over many e-folds (less than 2% deviation from the data) but it also gave just two numbers that characterised the decay. There is firstly a decay rate, k, enabling comparison with other decays. Secondly, it provides a stretch factor, p, which describes the degree of non-exponentiality of the decay, enabling comparisons of the deviation from exponentiality to be made between different systems.

$$I(t) = I(0).e^{-(k.t)^p} + \text{offset} \qquad 3.2$$

The principal problem of fitting stretched exponentials is that the characterisation is no longer independent of the time the decay was started because the exponent is no longer linear. Efforts must be made to ensure that the decay data have a time scale that really does start when excitation of the system ceases.

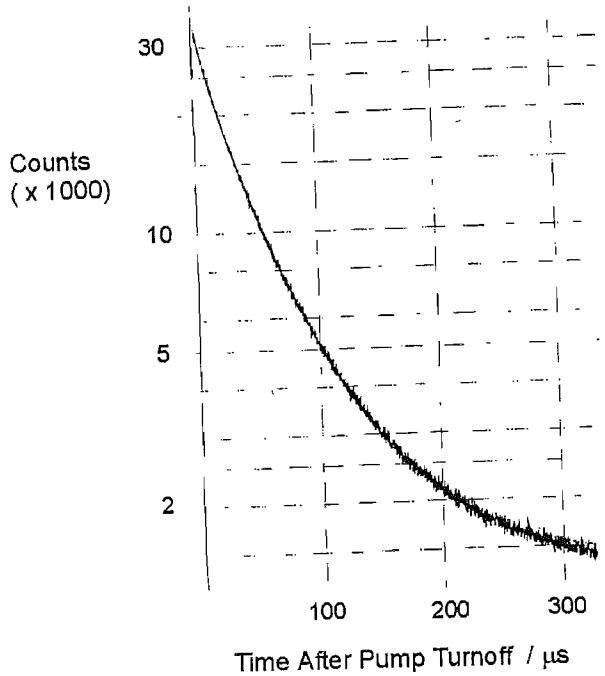

Figure 3.3: Decay for the LLS C(0.1) Sample

(The stretched exponential fit is shown as a dotted line, which in the figure is almost completely obscured by the data. This was typical of all the decays.)

The stretched exponential is a frequently occurring function used in physics and chemistry to describe non-exponential behaviour[1]. Although this function is immensely useful as a means of comparison for the decays of different systems, care should be taken before assigning the stretched exponential decay rate with a vast amount of physical meaning. This should be the case until the function is mathematically linked to some physical process in these systems and to date this has not been done. However, it has been shown empirically that a collection of emitting ions with a continuous range of lifetimes following a gaussian distribution produces a decay profile that corresponds excellently with that of a stretched exponential[2]. Interestingly, this is likely to be the situation for Cr^{3+} ions within a glass host sitting in a continuous range of sites experiencing different rates of non-radiative decay. It should always be remembered, however, that the effective lifetimes obtained from the stretched exponential will tend to be slightly higher than lifetimes calculated by other fitting methods. This will have an effect, legitimately or illegitimately, on the calculated values of emission cross-section.

3.4 Cryogenic Experiments

An important element of the experimental investigation was to carry out fluorescent spectra and lifetime measurements when the samples were cooled, to reveal the effects of the thermal quenching. This was not only for scientific interest but also to obtain the spectroscopic parameters that could be used to determine the advantages of cooling a fibre to liquid nitrogen temperatures.

The samples were cooled using a closed cycle refrigeration unit (CTI Cryogenics – Model 22). This device incorporated a heating element so that its cold finger could be warmed from its 15K minimum to any temperature required up to room temperature. Despite being relatively simple to use, its major drawback was temperature measurement and control. The bottom face of the thin samples (3mm thick) had good thermal contact with the cold finger being attached with GE varnish but there existed an enormous temperature difference (up to 60K) across the glass samples due to their poor thermal conductivity. To monitor this gradient, temperature sensors were placed upon the cold finger and the top of the sample. In order to minimise the uncertainty in the temperature in the relevant part of the glass, the pump beam was aimed as close to the top of the sample as possible. Additionally, it was important that the pump power was kept to minimum (<20mW) so that laser heating did not become a problem. This was particularly important at very low temperatures when the heat capacity was small. When the cold emission spectra were recorded, the spectral response correction for the apparatus included the effects of the glass window of the refrigeration unit with which the fluorescence passed.

As a definite fixed point, some of the lifetime experiments were carried out with the samples immersed in liquid nitrogen. As the nitrogen boiled away, the bubbles of gas scattered the pump beam and fluorescence, increasing the noise in the detected signal. However, the signal was so strong that this was not a problem.

3.5 Room Temperature Quantum Efficiency

The radiative quantum efficiency was an important spectroscopic parameter for this project. Although there are many approaches of direct determination of QE described in the literature[3,4,5], this type of investigation is notoriously difficult to carry out accurately as compared with lifetimes and emission spectra. This is likely to be the reason why the QE of transition metal doped glasses has rarely been reported in the literature.

3.5.1 Fundamental Concept

An integrating sphere technique was the chosen method of QE evaluation for this work. Although the inside of the sphere (Labsphere model FM-040-SF) was coated with highly reflecting paint, the idea was not to collect all the fluorescence but to simply give a constant geometry for collection. This straightforward technique[6] compared the amount of fluorescence of the sample in question with a reference sample of known QE. The accuracy of this method critically depended on the care taken during the experiment to make many different corrections.

Figure 3.4 shows the basic setup. The pump laser was chopped and sent through the sample with a known input power. The unabsorbed pump was measured when it emerged on the other side of the integrating sphere. The difference between these two values allowed the absorbed power to be calculated. The integrating sphere's interior was covered in a highly reflective white paint ("Spectraflect") which gave multiple diffuse reflections producing a spatially isotropic radiation field. A fraction of the sample's luminescence escaped by way of the output port and passed through long-pass filters blocking out the pump light. A baffle obstructed the direct light path from the sample to the output port and the signal was detected by a photodiode and a lock-in amplifier. The measured voltage, after being scaled for the absorbed pump light and the necessary corrections, was compared to the voltage measured for the reference sample (scaled and corrected) with known QE that calibrates the setup.

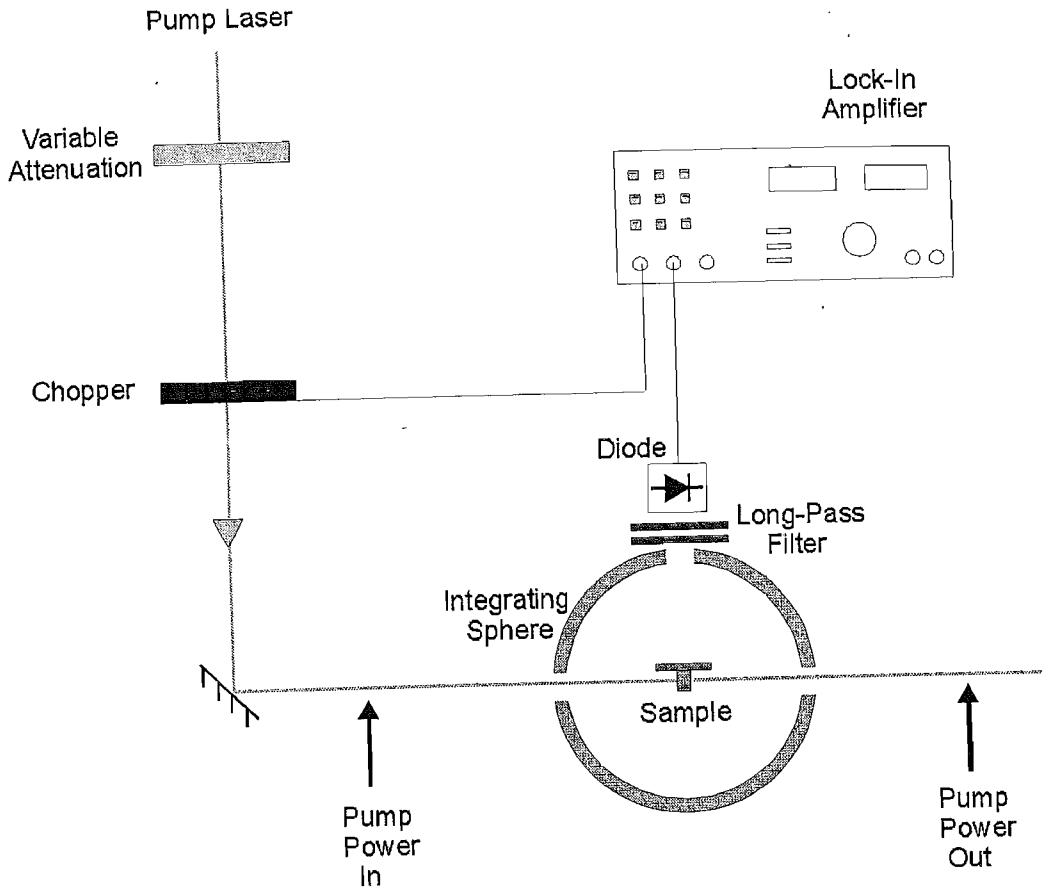

Figure 3.4: Experimental Arrangement for the Radiative Quantum Efficiency Investigation

3.5.2 Corrections and Important Considerations

Spectral Response of Detector and Integrating Sphere

Because the emission lineshapes of the samples were different to the reference sample, it was important to correct for the spectral response of both the photodiode and the integrating sphere (including the long-pass filter). The correction simply involved the normalised overlap integral for the system's response and the sample's emission spectrum.

Correction for Reflected Pump Power

To accurately estimate the absorbed power, it was important to consider the non-absorbed reflected power. Ignoring this would have misleadingly increased the absorbed power and lowered the measured QE. There were reflections from both the front and back face but light from the latter would have passed through the

doped sample twice and be partially absorbed. This reflected power was determined by measuring it with a power meter. Great care had to be taken with this correction as it could be a big source of random error. This was especially true if the optical thickness of the sample was small so that the reflected power was comparable to the absorbed power.

Correction for Scattered Pump Power

Again, to accurately estimate the absorbed power, it was important to consider the scattered pump light from the sample. This scattered light would have gone in all directions but should not have influenced the detected signal because of the long-pass filters. The scattered power, if ignored, would misleadingly increase the absorbed power and lower the measured QE. Great care had to be taken with this correction as it could be a big source of random error especially if the optical thickness of the sample was small. It is for this reason that it was very important that the samples were well cleaned for this experiment. During the experiment, a large diameter beam was passed through the sample averaging out the scattering differences over the sample, making the precise beam position less critical.

The Problems of Reabsorption

Because there was overlap between the absorption and emission bands for these transition metal doped glass samples, the measured QE would be misleadingly lowered owing to reabsorption. To reduce the effect of this problem, the sample was chosen to be as small as possible and have as low dopant concentration as possible. Additionally, it was important that the cuboid was polished on all six faces to avoid scattering of luminescence back into the sample. When the optical thickness of the sample is small, not only does an emitted photon not have to travel far through the sample to emerge but there is little chance of photons within the integrating sphere passing through the sample multiple times. It is for this reason that the integrating sphere should be as big as possible relative to the sample. For the QE experiments in this project, the sample size was (5x5x3)mm and the diameter of the integrating sphere was 10cm.

Where the error due to reabsorption was significant, it could be corrected for. As a reasonable estimate of the reabsorbed fraction for each sample, the absorption coefficients for the relevant wavelengths were calculated from the absorption results and it was assumed that the average emitted photon would have to travel 2mm to reach the surface of the sample. Multiple scatterings, re-emission, and fluorescence re-entering the sample from light travelling inside the integrating sphere were all assumed to be improbable.

Photodiode Linearity

Obviously it was important that the electronic signals remained in proportion to the original optical signals. Consequently the photodiode had to be in its linear region for the optical powers used. For these experiments, the photodiodes' linearity was extended by applying a reverse bias and including a transimpedance amplifier.

Pump Chop Rate

If the pump beam was chopped too fast it could distort the measured output voltage because of the limited time response of the photodiode.

Laser Power Stability

Instability of pump laser power was one of the major sources of random error for these experiments. Care was taken to minimise this instability by optimising the pump laser.

3.5.3 Details of the Cr^{3+} QE Experiment

A large area (10mm diameter) Si photodiode with a transimpedance amplifier was used as the detector. The setup's spectral response was determined using a Ti sapphire laser beam steered into the integrating sphere whose range of wavelength covered that of the luminescence of the samples'. The scattered power fraction for each sample was determined using a green He Ne for which wavelength the samples had negligible absorption. The difference between the reflection-corrected input power and the output power was assumed to be scattered. The reference sample used was a piece of gadolinium scandium gallium garnet (GSGG) whose QE was taken to be 95% [6].

3.3.4 Details of the Cr^{4+} QE Experiment

A large area (5mm diameter) InGaAs photodiode with a transimpedance amplifier was used as the detector. The setup's spectral response was determined by sending white light through a monochromator and then into the integrating sphere, covering the important wavelengths. The reference sample used was a piece of Cr^{4+} doped YAG whose QE was taken to be 11%[7].

3.5.5 Random and Systematic Error for the QE Investigation

Further to some of the considerations mentioned above, random error was reduced by taking repeat results for the same sample and changing both the beam position through the sample and the pump power. An estimate of the random error for the Cr^{3+} was made by taking the standard deviation of the repeat results, and for most samples this was found to be less than 0.2%. Considering all the various measurements that were made in determining the QE, the random error has been reduced effectively.

Within the results, there will undoubtedly be systematic error, the size of which was much harder to estimate. One obvious example might be error in the known QE of the reference sample. If more than one reference sample had been available, this would be a good way to reduce this.The important thing for this project was that, because the random error was low, the relative QE of the sample glasses can be confidently compared, even if systematic error shifts their measured absolute values.

---

[1] "Optical Spectroscopy of Glasses", A Blumen, ed. I Zschokke Reidel, Netherlands, (1986) p199

[2] J R Lincoln, "Spectroscopy of Rare Earth Doped Glasses", PhD thesis (1992) Southampton University.

[3] "Quantum Efficiency Measurement in Solids by Photoacoustic and Luminescence Experiements", E Rodriguez, L Nurez, J Tocho and F Cusso Journal of Luminescence, **58**, 353 (1994)

[4] "Spectroscopy and Photokinetics of Chromium (III) in Glass", L J Andrews, A Lempicki and B McCollum, J. Chem. Phys., **74**, (10), 5526 (1991)

[5] "Spectral Characteristics and Fluorescence Quantum Efficiency of Cr(III) in Phosphate and Silicate Glasses with Li and Be Modifiers", A Kisilev and R Reisfeld, Solar Energy, **33**, (2), 163 (1984)

[6] "Quantum Efficiencies of Chromium Doped Glasses", M J Payne and N Lowde, Physics and Chemistry of Glasses, **32**, (5), 222 (1991)

[7] "Performance of YAG:Cr^{4+} Laser Crystal", A G Okhrimchuk and A Shestakov, Optical Materials, **3**, 1 (1994)

Chapter 4

Bulk Spectroscopy of a Range of Cr^{3+} Doped Lithium Lime Silicate Glasses

4.1 Introduction

Although there have been many examples of transition metal lasers operating with a crystalline host, there have been no successful demonstrations of a transition metal lasers using a glass host. The fundamental spectroscopic parameters which characterise a gain medium are the cross-section of emission (σ_e) and the measured lifetime (τ). For a given pump power and geometry, it is their product, $\sigma_e\tau$, that relates to the amount of gain. The problem for transition metals in glass, however, is that this product is dramatically reduced when compared to crystals; σ_e is diminished due to the broader emission profile and τ is much smaller from the effects of non-radiative decay. Overall the consequence is that the pump thresholds for bulk transition metal glass lasers are infeasibly high.

The main aim of this project was to try to develop a Cr^{3+} fibre laser where the pump might be confined to an extent where the threshold becomes practical. Much of the work within the project may be thought of as a search for a glass that both maximises $\sigma_e\tau$ and also has the potential to be made into a low loss fibre.

The subject of this chapter is the spectroscopy of a great range of Cr^{3+} glasses that were thought to represent the best candidates. Although it is primarily the values of σ_e and τ that were important for the determination of an optimum fibre composition, a more extensive set of results was obtained to try to understand the physical system as fully as possible.

4.2 Problems in Determining σ_e

The value of cross-section of emission is notoriously hard to measure. Often it gets estimated indirectly from the absorption strength and lineshape through Judd-Ofelt (only applicable to rare earths) and McCumber[1] theories (applicable to rare earths and transition metals).

Another method to assign indirectly a value to σ_e is to use the Fuchtbauer- Ladenburg[2] equation

$$\sigma_e(\lambda) = \frac{\lambda^5 I(\lambda)}{8\pi n^2 c \tau_r \int \lambda I(\lambda) d\lambda} \qquad 4.1$$

where τ_r is the radiative lifetime, n is the refractive index and $I(\lambda)$ is the measured emission spectrum. This equation can be applied to any transition without the worry of fulfilling certain assumptions e.g. homogeneous broadening only. It can be seen that compared to the spontaneous fluorescence spectrum, the stimulated emission spectrum is weighted to long wavelengths by a factor of λ^5. Now if the top and the bottom of the equation is multiplied by the measured lifetime τ_m,

$$\sigma_e(\lambda) = \frac{\eta \lambda^5 I(\lambda)}{8\pi n^2 c \tau_m \int \lambda I(\lambda) d\lambda} \qquad 4.2$$

This is true since the radiative quantum efficiency (QE), $\eta = \tau_m / \tau_r$. This new equation gives a simple method of determining the emission cross-section using quantities that can be measured by fairly straightforward experiments. Additionally, Equation 4.2 emphasises that it is the QE that is the most critical spectroscopic parameter for a device, since the others vary less markedly between different glass hosts.

There will be further problems if it is needed to make an estimate of σ_e at temperatures other than room temperature, for instance when modelling gain at low temperatures. Quantum efficiency is easiest to measure at room temperature (e.g. using an integrating

sphere) and although τ_m is simple to measure at different temperatures it will not be a good guide for QE. This is because the radiative lifetime will also be dependent on temperature due to dynamic odd parity distortions as explained in the Section 2.7.3.

4.3 Cr^{3+} Doped Glass in the Literature

There are a great many past papers since the early 1980's that have looked at Cr^{3+} in a wide variety of glasses[3,4,5]. Most of these carried out initial investigations of glass hosts, establishing the principal spectroscopic features using typical absorption and emission experiments. Often after confirming that it was Cr^{3+} sitting in a low crystal field and assigning the various transitions, the investigations focused upon using the spectroscopy to yield information about the amorphous local environment. Since the energy levels are in part determined by the interaction of the ligands' crystal field, the chromium ion can be used as an optical probe to reveal details of the strength and symmetry of the electrostatic field and the range of different sites.

There is also a selection of papers[6,7,8,9] that, rather than concentrating on gaining a deep understanding of the local environment, have thought of the Cr^{3+} luminescence as the basis for a future device. Recognising that the key requirement for the development of successful devices would be finding a glass host with acceptable quantum efficiency, the papers most relevant to this project have together undertaken a wide-ranging investigation of many different glasses. There have been attempts to explain not only why glasses have low QE but also why it is that the QE is so strongly dependent upon the specific glass host.

Interestingly, the devices envisaged at the time were not just near infrared lasers. Much of the research was aimed at the development of luminescent solar concentrators. These devices are designed to absorb the visible solar radiation effectively and then convert the energy, by means of the fluorescence, to longer wavelengths where semiconductor solar cells work more efficiently. Despite these excellent spectroscopy papers in the 1980's, the work was never followed up and translated into working devices. It was concluded that along with the problem of reabsorption, the QE in glasses was too low for solar concentrators and the research moved on to glass ceramics. Similarly, there was no demonstration of a Cr^{3+} doped glass laser or report in the literature of anyone having tried.

There has been quite a wide investigation of the room temperature QE of many different families of glass, including phosphates, fluorophosphates, silicates, borosilicates, borates, tellurites and germanates. The result of the survey was that most glasses have a QE of much less than 10%, some almost without any luminescence at all, whilst there are a few very special glasses with QE of around 20%. Although it is clear that the network former is the primary factor determining the strength of the crystal field[10], the family of glass plays little part in controlling electron-phonon coupling and QE. What does seem to be important is the stiffness of the site where small, highly-charged modifying cations seem to be the common link between the good glasses[6,7]. Trying to establish what other characteristics are beneficial for QE is difficult, especially sometimes when similar glasses with only slightly different ratio of composition can have such different QE.

Table 4.1: Glass Hosts with the Best Cr^{3+} Radiative Quantum Efficiency

Glass Composition	QE	Ref
Lithium Lanthanum Phosphate	22%	11
Aluminium Phosphate	19%	6,10
Lithium Lime Silicate	19%	6,10
Lithium Beryllium Silicate	19%	10
Barium Sodium Germanate	25%	9

Some comments on Table 4.1 are in order. The best result here was the barium sodium germanate but this paper pointed out that the glasses were prone to crystallisation. If their sample did contain microcrystals making it at least partially glass ceramic in nature, then the QE could have been misleadingly increased. Besides an unstable glass would be of little use for fibre drawing. Systematic error will be a major problem in any QE experiment that uses a reference sample of known QE for calibration. The authors of this germanate paper used a lithium lime silicate sample as their reference, relying heavily upon an earlier glass QE result.

The lithium lanthanum phosphate reference[11] mention this high QE result only in passing but the paper describing the details of the composition used could not be found – it was probably never published. The element beryllium as used in the lithium beryllium silicate glass is one of the most toxic chemicals known and would have needed extremely careful safety measures for its fabrication.

4.4 The Selection of Glass Hosts for Investigation

With the difficulty in predicting glasses with good Cr^{3+} radiative quantum efficiency, it seemed logical to follow the work of past papers using the glasses that have already been shown to be successful. However, barium sodium germanate and lithium beryllium silicate were ruled out for reasons given in the last section. One sample of aluminium phosphate was fabricated following Reference 6 and one sample of lithium lanthanum phosphate was melted with a stoichiometric composition in the absence of composition details for the result in Reference 11.

Noting the barium sodium germanate result, a sample of lead germanate was fabricated. This was particularly interesting to investigate since it has already been used for effective optical fibres[12]. Additionally, as a host, it has low phonon energy[12] compared to other oxide glasses and has been used to raise the radiative quantum efficiency for rare earths.

From an early stage it was anticipated that lithium lime silicate (LLS) would make the best glass for fibre drawing. A range of sixteen glasses were melted based upon Reference 6 but making small, carefully chosen changes to search for a composition with improved spectroscopy and to find the glass with the best thermal properties for fibre drawing. The various compositions were chosen so that only one factor was changed at a time from the basic composition of Reference 6, so conclusions would be easy to draw. Here is a summary of the strategy:

- *Dopant Concentration*

  Four samples of the basic composition were melted but with different Cr_2O_3 concentration.

Sample Code		
C(0.3)	0.3wt% Cr_2O_3	
C(0.1)	0.1wt% Cr_2O_3	
C(0.05)	0.05wt% Cr_2O_3	(Basic Composition)
C(0.015)	0.015wt% Cr_2O_3	

- *Changing the Modifier Ratio*

  Four samples were melted with the network formers unchanged from the basic composition but the ratio between the modifiers (Li and Ca) was varied.

A	Li↑↑	Ca↓↓
B	Li↑	Ca↓
C	Li↓	Ca↑
D	Li↓↓	Ca↑↑

- *Changing the Former Ratio and Substituting the Former*

  Four samples were melted with the network modifiers unchanged from the basic composition. In two of the samples the ratio between the formers (Si and Al) was varied. In the other two, the Al_2O_3 was substituted for either La_2O_3 or B_2O_3.

X	SiO_2↑	Al_2O_3↓
Y	SiO_2↓	Al_2O_3↑
Z	Al_2O_3	→ La_2O_3
R	Al_2O_3	→ B_2O_3

- *Changing the Ratio of Formers to Modifiers*

  Two samples were prepared where the overall ratio of formers to modifiers was varied compared to the basic composition.

M	Formers↓	Modifiers↑
N	Formers↑	Modifiers↓

- *Substituting the Modifying Cations*

  Two samples were melted with the network formers unchanged from the basic composition. In one of the samples sodium was substituted for lithium and in the other barium was substituted for calcium.

O	Li_2O	→	Na_2O
P	CaO	→	BaO

4.5 Glass Fabrication

Table 4.2 shows the exact compositions of all the samples prepared, which were all 25g in mass. All the starting materials were powders of at least 99% purity. The Li, Ca, Na and Ba starting components were all in the form of carbonates. In the case of the phosphates, P_2O_5 was in the form of $NH_4H_2PO_4$. During melting, these compositions underwent some alterations owing to volatilisation of components, especially P_2O_5. No special measures were taken to remove water from the starting powders following the procedures used in Reference 6 that yielded good results.

Both References 6 and 10 used As_2O_3 in the preparation of lithium lime silicate so that Cr^{6+} would be reduced to form Cr^{3+} and also to help remove bubbles from the glass. However, As_2O_3 being volatile at the melting temperature was thought to be too much of a health hazard. Instead Sb_2O_3, which has a similar effect, was used as a substitute.

The chromium was added in the form of Cr_2O_3 and was weighed out accurately to within 10% of the intended mass. All the samples had 0.05wt% doping (about 1.15 x 10^{19} ions/cm^3) except those specifically investigating varying Cr concentration. All the compositions were well mixed and then melted in alumina crucibles. The electric furnace had molybdenum disilicide elements and no option other than an air atmosphere. The glass compositions, which are given in mole %, are shown in Table 4.2.

Table 4.2: Cr^{3+} Doped Glass Compositions

All compositions doped with 0.05wt% Cr_2O_3 unless otherwise stated.

Glass Type	Code	Composition (mole %)		Melt Temperature (°C)
Aluminium Phosphate	AlP	Al_2O_3 – 25.0 Cr_2O_3 – 0.1wt%	P_2O_5 – 75.0	1500
Lithium Lanthanum Phosphate	LLP	Li_2O – 23.0 La_2O_3 – 10.0	P_2O_5 – 67.0 Cr_2O_3 – 0.1wt%	1400
Lead Germanate	PbG	GeO_2 – 55.0 BaO – 10.0 K_2O – 5.0	PbO – 20.0 ZnO – 10.0	1100
Lithium Lime Silicate (LLS)	C(0.05)	Li_2O – 22.9 SiO_2 – 63.3 Sb_2O_3 – 0.6	CaO – 10.5 Al_2O_3 – 2.7 Cr_2O_3 – 0.05wt%	1400
	C(0.015)	Li_2O – 22.9 SiO_2 – 63.3 Sb_2O_3 – 0.6	CaO – 10.5 Al_2O_3 – 2.7 Cr_2O_3 – 0.015wt%	
	C(0.1)	Li_2O – 22.9 SiO_2 – 63.3 Sb_2O_3 – 0.6	CaO – 10.5 Al_2O_3 – 2.7 Cr_2O_3 – 0.1wt%	
	C(0.3)	Li_2O – 22.9 SiO_2 – 63.3 Sb_2O_3 – 0.6	CaO – 10.5 Al_2O_3 – 2.7 Cr_2O_3 – 0.3wt%	

LLS	A	Li_2O – 29.4	CaO – 4.0	1400
		SiO_2 – 63.3	Al_2O_3 – 2.7	
		Sb_2O_3 – 0.6		
	B	Li_2O – 26.4	CaO – 7.0	
		SiO_2 – 63.3	Al_2O_3 – 2.7	
		Sb_2O_3 – 0.6		
	C	Li_2O – 18.4	CaO – 15.0	
		SiO_2 – 63.3	Al_2O_3 – 2.7	
		Sb_2O_3 – 0.6		
	D	Li_2O – 13.4	CaO – 20.0	
		SiO_2 – 63.3	Al_2O_3 – 2.7	
		Sb_2O_3 – 0.6		
	X	Li_2O – 22.9	CaO – 10.5	
		SiO_2 – 66.0	Al_2O_3 – 0	
		Sb_2O_3 – 0.6		
	Y	Li_2O – 22.9	CaO – 10.5	
		SiO_2 – 61.0	Al_2O_3 – 5.0	
		Sb_2O_3 – 0.6		
	Z	Li_2O – 22.9	CaO – 10.5	
		SiO_2 – 63.3	La_2O_3 – 2.7	
		Sb_2O_3 – 0.6		
	R	Li_2O – 22.9	CaO – 10.5	
		SiO_2 – 63.3	B_2O_3 – 2.7	
		Sb_2O_3 – 0.6		
	M	Li_2O – 27.0	CaO – 12.4	
		SiO_2 – 57.6	Al_2O_3 – 2.5	
		Sb_2O_3 – 0.6		
	N	Li_2O – 18.8	CaO – 8.6	
		SiO_2 – 69.0	Al_2O_3 – 2.9	
		Sb_2O_3 – 0.6		
	O	Na_2O – 22.9	CaO – 10.5	
		SiO_2 – 63.3	Al_2O_3 – 2.7	
		Sb_2O_3 – 0.6		
	P	Li_2O – 22.9	BaO – 10.5	
		SiO_2 – 63.3	Al_2O_3 – 2.7	
		Sb_2O_3 – 0.6		

The glasses were kept at their final temperature (shown on Table 4.2) for 30 minutes and then cast on a prewarmed stainless steel plate with stainless steel moulding blocks. All the samples were immediately annealed after the casting. The annealing regime was to hold the glass at 500°C for 60 minutes and then ramp down to room temperature at 25°C/hour. All the samples were cut into cuboids (5mm x 5mm x 3mm) and polished on six sides for the spectroscopy experiments (the small size especially was important for the quantum efficiency investigation).

During melting it became clear that aluminium phosphate was unlikely to be suitable for fibre drawing. Even at 1500°C, this melt was very viscous and consequently the resulting glass was full of bubbles.

4.6 Results and Discussion

4.6.1 Room Temperature Absorption Spectra

Figure 4.1 shows the absorption spectra for lithium lanthanum phosphate, aluminium phosphate and the lead germanate glasses. The spectra all have a logarithmic scale and were taken with 5nm resolution; higher resolution revealed no extra detail. All the graphs show that there are two very broad vibronic bands, except for the lead germanate whose UV-edge stretches into the visible region at about 520nm obscuring the higher energy absorption. The broad bands are approximately gaussian in shape indicating a large Huang-Rhys factor. This is no surprise for a glass, since the bonds will have a strong covalent character and electron-lattice coupling will be more effective. The positions of the transitions were consistent with Cr^{3+} in an octahedral site, and they can be attributed to $^4A_2 \rightarrow {}^4T_2$ (660nm) and $^4A_2 \rightarrow {}^4T_1$(450nm).

Although the 660nm absorption peaks are apparently a lot broader than the 450 peaks, the energy widths scaled by the absolute energy values of each band are actually very similar. This indicates that the parabolas of the Single Configuration Coordinate Model for the $^4T_2$ and $^4T_1$ levels have a very similar shape. Another feature common to all these glasses is the structure in the $^4A_2 \rightarrow {}^4T_2$ absorption band. The possibility

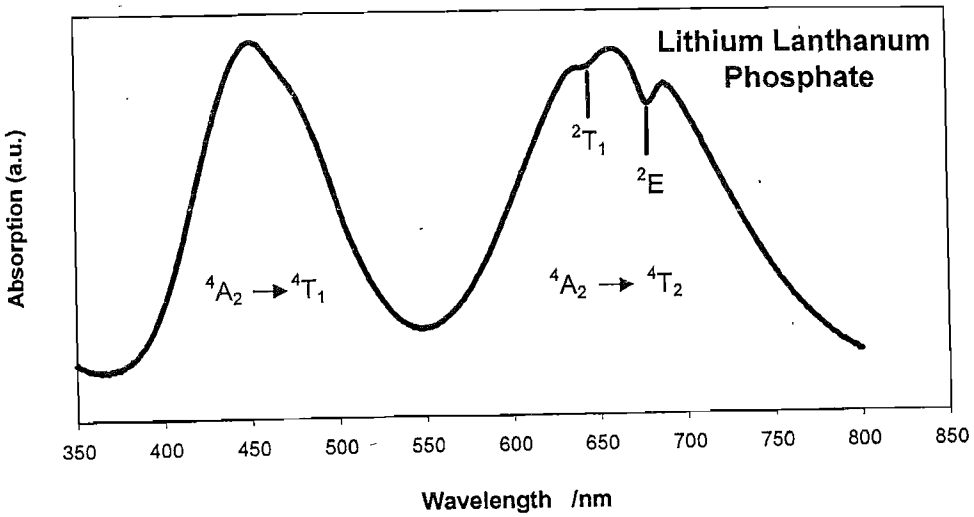

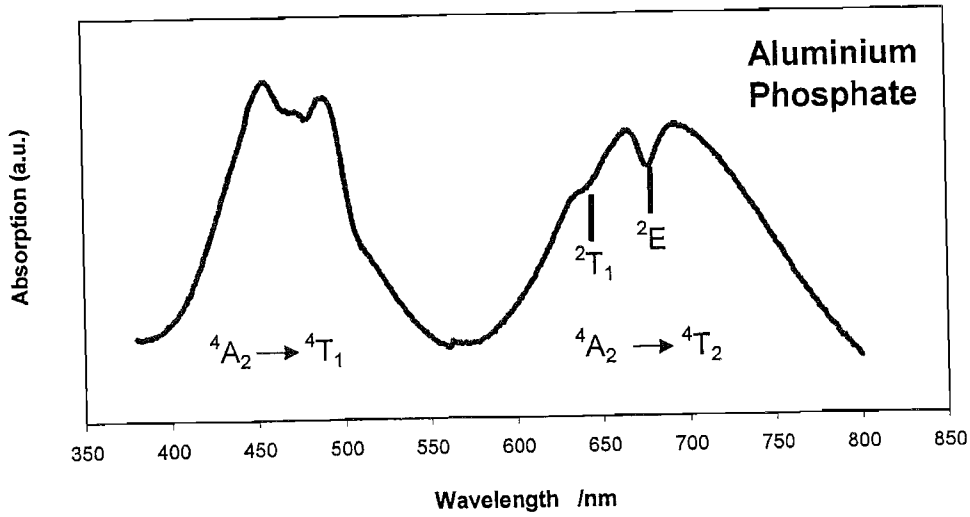

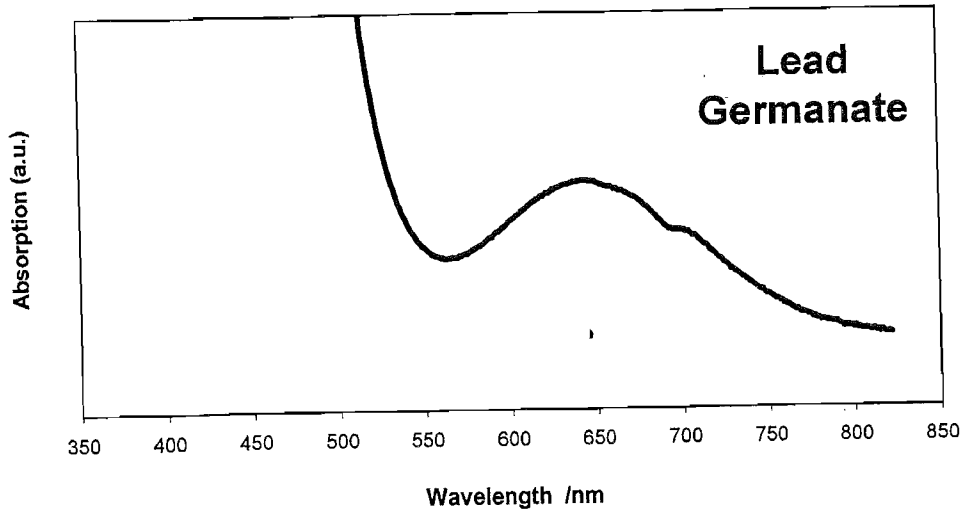

Figure 4.1: Absorption Spectra for Lithium Lanthanum Phosphate, Aluminium Phosphate and Lead Germanate Glasses

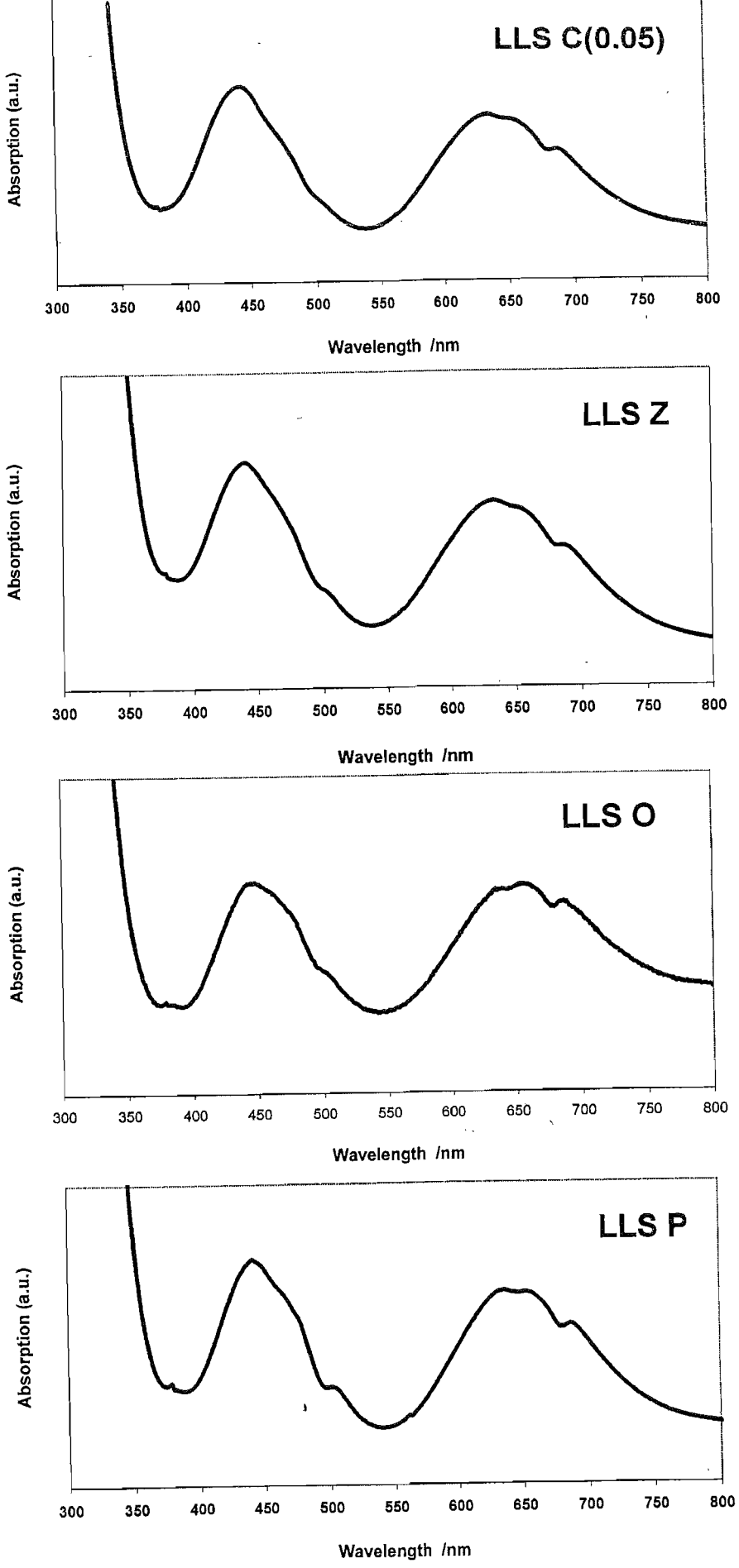

Figure 4.2: A Selection of Absorption Spectra for the Lithium Lime Silicate Samples

of fluorescence distorting the spectra during measurement could be rejected partly because the radiative quantum efficiency was low and partly because the effective solid angle to the measurement optics was small. This structure can be attributed to the sharp and non-phonon assisted transitions to the ^2E and $^2T_1$ transitions superimposed upon the broader one. Following the Fano-antiresonance interpretation[13,14], the fine structure are dips caused by destructive interference between the sharp transitions and the $^4T_2$ vibronic quasi-continuum. The result is a cancellation of observed intensity as well as a change of the original peak shape and position for the ^2E and $^2T_1$ transitions. The structure just below 500nm in the case of aluminium phosphate is unexpected when compared to results in previous papers. It is difficult to pinpoint the cause but one explanation might be a rare earth contaminant in the glass. The precise cause was not investigated further as the problems of melting bubble-free aluminium phosphate ruled it out as being a straightforward candidate for low loss fibre.

The absorption spectra for the sixteen LLS samples were all very similar to one another. Figure 4.2 shows a selection of the absorption results displaying what differences there were. The basic features are similar to the glasses in Figure 4.1 and the Cr^{3+} transitions are denominated in exactly the same way. One difference between the LLS absorption spectra was that as the size of the modifying cation was increased, the feature close to 500nm became more prominent.

It is notable that there was no broad absorption at about 370nm[10] that would have indicated the presence of Cr^{6+}. This strong band in the UV having a tail in the blue is due to electron charge transport from the oxygen to the chromium. This absorption does not lead to fluorescence and can be considered a parasitic process.

The absorption spectra may be used to determine the octahedral crystal field strength, Dq, and the Racah parameters, B and C, by a method[15] originally determined by Tanabe and Sugano. In octahedral symmetry the energy difference between $^4A_2$ and $^4T_2$ during absorption is equal to 10Dq which is measured from the peak of the $^4T_2$ band. The value of B, determined from the energy separation, Δ, between the $^4A_2 \rightarrow {}^4T_1$ (ν_2) and the $^4A_2 \rightarrow {}^4T_2$ (ν_1) absorption peaks, is given by

$$B = \frac{(2\upsilon_1 - \upsilon_2)\Delta}{3(9\upsilon_1 - 5\upsilon_2)} \qquad 4.3$$

The C Racah parameter is calculated from the position of the $^4A_2 \rightarrow {}^2E$ absorption peak using the equation

$$C/B = \frac{1}{3.05}\left(\frac{E(^2E)}{B} + 1.8\left(\frac{B}{Dq}\right) - 7.9\right) \qquad 4.4$$

When trying to discriminate between the $^2T_1$ and ^2E peaks that make up the fine structure it is helpful to realise that the ^2E peak will always be at lower energy; this is obvious from consideration of the Tanabe-Sugano diagram. It is conventional to think of the results of these formulae in terms of energy units cm^{-1}.

These equations give values accurate to about 5% for Dq/B and C/B within the ranges 1.5 - 3.5 and 3.0 – 5.0 respectively. The real error comes about in determining the position of transition peaks which can be quite difficult sometimes as the Fano antiresonances can distort the shape of the transition. For instance in the case of LLS, not only was the exact position of the ^2E peak uncertain but the $^2T_1$ transition obscured the exact position of the $^4T_2$ peak. It is important to realise that the values of these parameters calculated for a glass will be averages over all the sites.

Table 4.3 shows the results of calculations for the crystal field strength and the Racah parameters for the glasses. The Racah parameters for the lead germanate could not be calculated from these results since $^4A_2 \rightarrow {}^4T_1$ transition was obscured by the UV-edge. The value of Dq/B is a measure of the strength of the crystal field and the table shows that the LLS C(0.05) has the highest crystal field. The Racah parameter B can be regarded as a measure of the interelectronic repulsion in the d-shell and can be useful when considering the ionic / covalent properties of Cr^{3+}-ligand bonding[14]. The greater B, the greater the ionic content of the bond. Decreasing B means a larger covalent character. These result show that the LLS C(0.05) sample had the most covalent character.

Table 4.3: Calculated Crystal Field and Racah Parameters

	DQ	B	DQ/B	C/B
ALP	1460	795	1.83	3.82
LLP	1510	735	2.06	4.26
PbG	1550	-	-	-
LLS C(0.05)	1560	729	2.13	4.27
LLS O	1520	761	2.00	4.04
LLS P	1550	749	2.07	4.11

Using the absorption spectra for the four LLS samples with differing Cr concentrations, calculations of the size of the absorption cross-section were made. This was done by calculating that the density of LLS to be 2.91g/cm^3, therefore 0.05wt% Cr_2O_3 concentration corresponded to (1.15 +/- 0.04) x 10^{19} ions/cm^3. Then using the Beer-Lambert Law,

$$I(L) = I(0)\exp(-\alpha L) \qquad 4.5$$

where I is the intensity, L is the sample thickness and α (the absorption coefficient) is equal to the product of the Cr concentration and the absorption cross-section, $N\sigma_a$. Figure 4.3 shows that the peak cross-section for the $^4A_2$ to $^4T_2$ transition was 5.6 x 10^{-20}cm^2 at a wavelength of 635nm. The largest source of error in this measurement was the removal of an offset caused by Fresnel reflections or a portion of the beam not passing through the small sample. This systematic error would have been no larger than 0.5 x 10^{-20}cm^2.

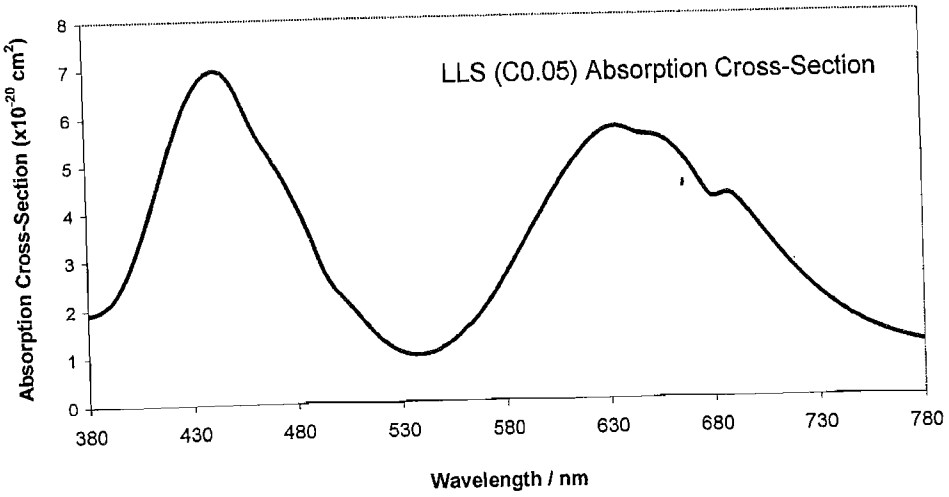

Figure 4.3: Absorption Cross-Section for the Basic Composition of LLS

4.6.2 Room Temperature Emission Spectra

Room temperature emission spectra were taken for all the glass samples for both red (633nm) and blue (488nm) pump light. Figure 4.4 show examples of these spectra for the red pump. The spectra, which have been corrected for the spectral response of all the measurement optics, were taken with CCD spectrometer and the resolution was never worse than 10nm. This device was sensitive only up to 1μm, which explains the slightly truncated spectra at long wavelengths.

All the spectra corresponded well to the vibronic $^4T_2$ to $^4A_2$ transition in a low crystal field host. The fluorescence was extremely broad with a width of about 180nm in the near infrared. The gaussian-shaped emission again indicated strong electron-lattice coupling, as does the large Stokes Shift of about 160nm.

Glass Sample	Emission Peak /nm	Stokes Shift /nm	Emission Width (FWHM) /nm
LLP	828	166	180
AlP	847	160	178
PbG	819	176	202
LLS C(0.05)	803	162	175

Table 4.4: Comparisons of the Glasses' Emission Spectra

Table 4.4 displays the emission peak wavelength, the Stokes Shift and the width of emission for a selection of the glasses. It is interesting to note that lead germanate, which had significantly the largest Stokes shift, had noticeably the broadest emission. It was also notable that AlP, which had the lowest crystal field strength as measured from the absorption spectrum, emitted at the longest wavelength. Similarly, LLS C(0.05), experiencing the largest crystal field, emitted at the shortest wavelength.

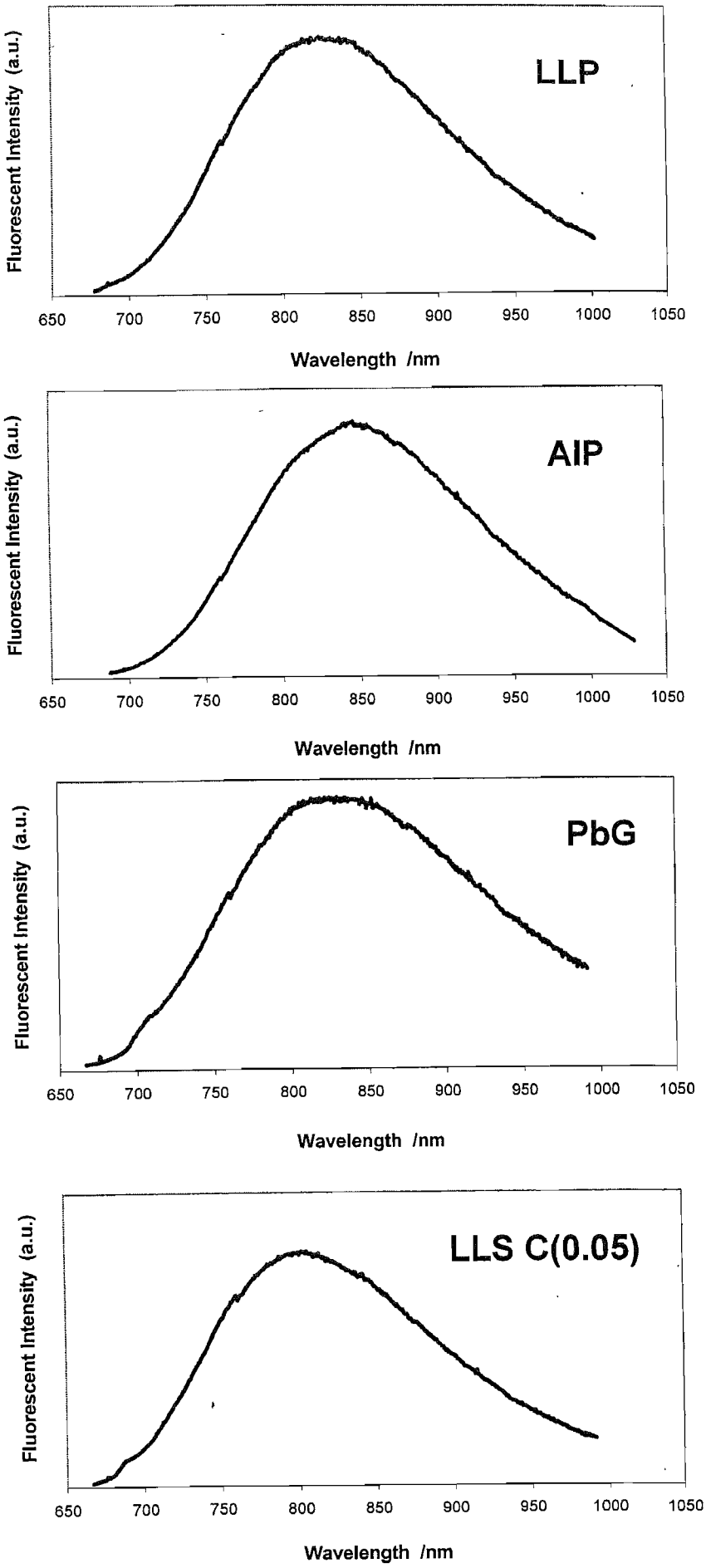

Figure 4.4: Room Temperature Fluorescecnce Spectra

For each host the emission spectra were very similar except for small shifts of the emission peak. For all the samples the emission peak was at longer wavelengths for the blue pump light than it was for the red. This shift was about 5nm for the LLS and PbG samples and about 10nm for the AlP and LLP samples. This effect is simply explained by inhomogeneous broadening and looking back at the absorption spectra of Figure 4.1 and 4.2. As explained in Section 2.5, most of the transition broadening will be caused by the vibronic mechanism which is homogeneous but there will also be an inhomogeneous element which is caused by the different glass sites. For all of the samples, the 488nm pump light excited the low field sites but the 633nm light will have excited average crystal field sites in the LLS and PbG, and high field sites in the cases of LLP and AlP.

The sharp R-line was visible in the room temperature emission spectra for the lead germanate and lithium lime silicate samples. The R-line was at a longer wavelength for lead germanate but this would not have been related to this host's lower crystal field since ^2E energy level is independent of crystal field strength. It is likely that this effect was caused by the hosts' differing Racah parameters.

4.6.3 Temperature Dependent Emission Spectra for LLS

For the LLS C(0.05) sample, emission spectra were taken at different sample temperatures for both red (633nm) and blue (488nm) pump light. The sample was cooled with a closed cycle refrigeration unit (CTI Cryogenics – Model 22). A number of precautions were taken to accurately monitor and control the sample temperature. Firstly, the sample temperature was measured on both the top and bottom sides. Next, the sample was quite thin (3mm) to minimise the temperature difference across it. Lastly, the pump beam had low power so that there was little heating effect and it was aimed towards the top of the sample so that the relevant temperature was close to that measured by the top sensor.

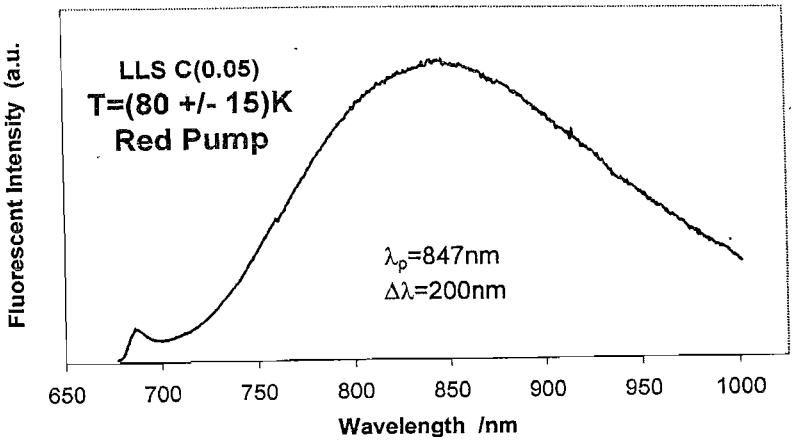

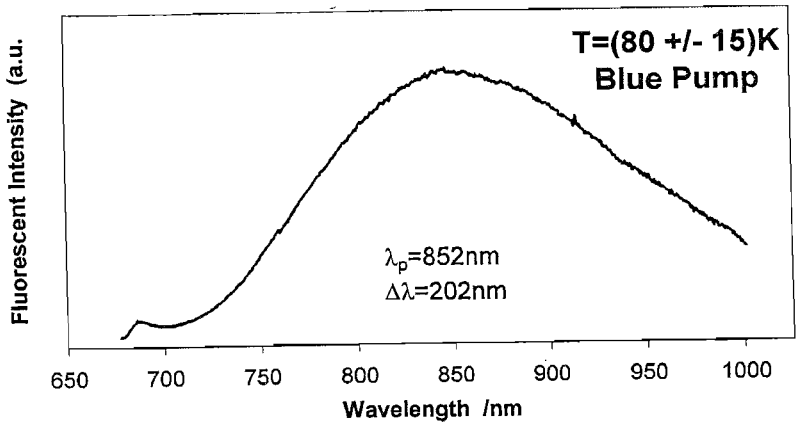

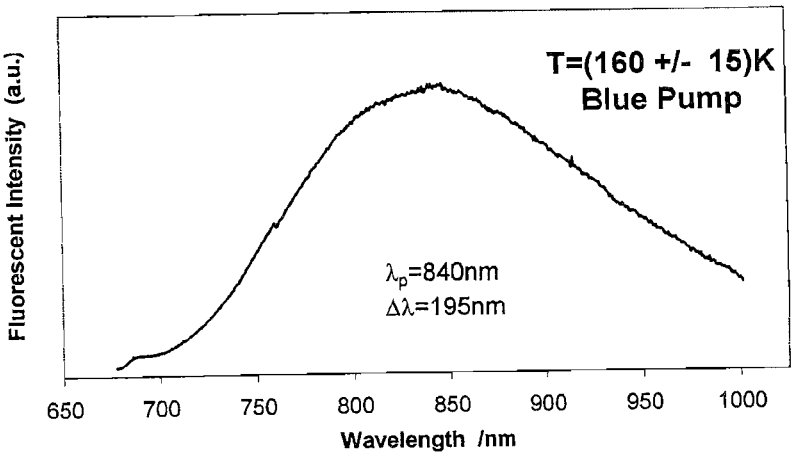

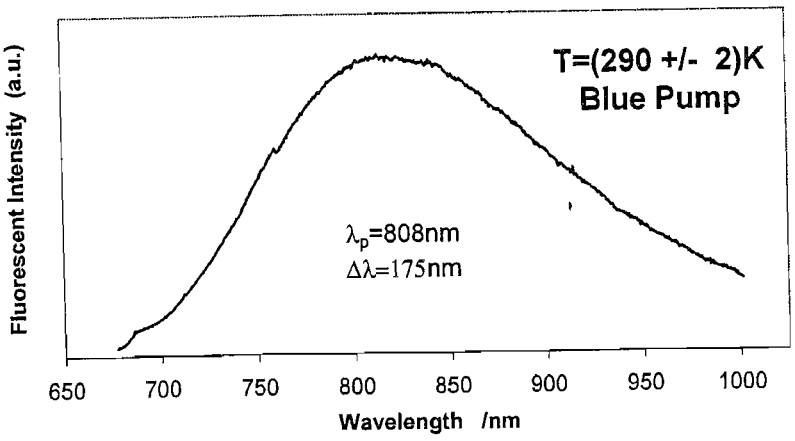

Figure 4.5: Temperature Dependent Emission Spectra

Figure 4.5 shows a selection of the temperature dependent emission spectra taken. It can be seen that the emission remained gaussian in shape for all the temperatures and the R-line at 689nm became more distinct at lower temperatures. The reason for this reduced R-line radiative decay as the temperature increases was due to phonons assisting electrons across the potential barrier from the ^2E level to the $^4T_2$ level depleting the original ^2E population.

As with the room temperature emission spectra, there was little difference between spectra pumped with red or blue light except that emission peak for the blue pump was shifted by about 5nm to a longer wavelength. Additionally, the R-line, which could be seen more clearly at lower temperatures, was more distinct for the red pump. Again, the inhomogeneous broadening argument explains this.

What is not shown explicitly in Figure 4.5 is the degree to which the amount of fluorescence diminished as the temperature increased from 77K to room temperature. Taking great care to keep the experimental conditions constant (especially laser power, sample position and CCD array slits) the amount of fluorescence for the two temperatures could be compared. The result was that the room temperature fluorescence was 0.2 times as strong as the fluorescence at liquid nitrogen temperature. Using the room temperature QE result from later in the chapter, this gives a liquid nitrogen temperature QE estimate of about 75%. Remember that, for transition metals, it is not possible to estimate the QE at 77K using lifetime results for the two temperatures and the room temperature QE because of the presence of dynamic odd parity distortions (see Section 2.7.3).

Interestingly, as the temperature increased, the emission peak shifted towards the blue. In the case of crystalline hosts, there is often a red shift with increasing temperature[16] since thermal expansion of the lattice leads to a reduced crystal field (see Equation 2.4). The blue shift experienced here can be attributed to the preferential non-radiative decay of the glass sites with low crystal field or large electron-lattice coupling. These sites, which intrinsically emit at the longer wavelengths, have a smaller energy barrier for non-radiative decay by level crossing. As the temperature increased, the non-radiative decay rate increased, reducing the fluorescence particularly at longer wavelengths. It was also for this reason that the emission width decreased with increasing temperature.

4.6.4 Temperature and Emission Wavelength Dependent Lifetimes for LLS

For the basic composition of LLS – C(0.05) – radiative lifetimes were measured for a range of different emission wavelengths for the $^4T_2$ to $^4A_2$ band and the R-line. This process was repeated for many different sample temperatures.

(A more complete exposition of the experimental method and stretched exponential fits is included in Chapter 3). The blue (488nm) pump beam, which was chopped mechanically, had a power of 10mW and a turn-off of 2μs. The thin sample (3mm) was held on a cold finger in a closed-cycle He refrigerator. The temperature was measured on the top and bottom of the sample in order to monitor and control the temperature gradient across it. The collected fluorescence was sent through a monochromator, and the final signal was detected by a photomultiplier tube (PMT). The decay profiles were fit with regression software but were found not to be single or double exponentials. Stretched exponentials worked particularly well and were used for the results.

The error in the lifetime should be small because PMTs have fast time response (10ns), the pump turn-off was short (2μs) compared to the lifetime and the fit was good. The monochromator slits were closed so that the wavelength resolution was 10nm. The greatest source of error undoubtedly lay in determining the sample temperature. This was particularly true for low temperatures where the temperature difference across the top and bottom of the sample could be 60K. However, the effective temperature error was much less than this. The position of the pump beam within the sample remained the same right the way through the experiment, giving rise to a systematic error depending on what this precise position was. By taking the fixed point of sample immersion in liquid nitrogen this systematic error was diminished.

Figure 4.6 shows the temperature dependence of the R-line (690nm) lifetime. The figures in brackets denote the stretch factor for the fits. Points could not be obtained beyond 170K because the fluorescence became too weak; the point at 190K is thought to be dominated by fluorescence from the $^4T_2$ to $^4A_2$ band. The results show that as the temperature increased, the R-line's lifetime rapidly decreased. This effect was likely

Figure 4.6

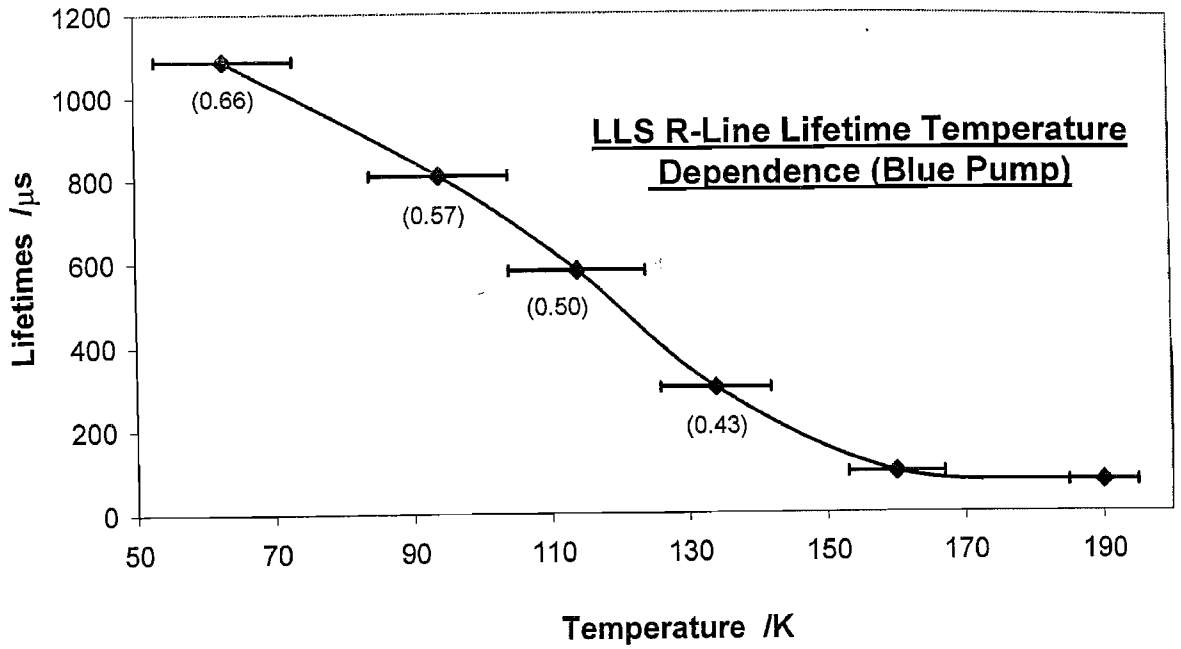

Figure 4.7

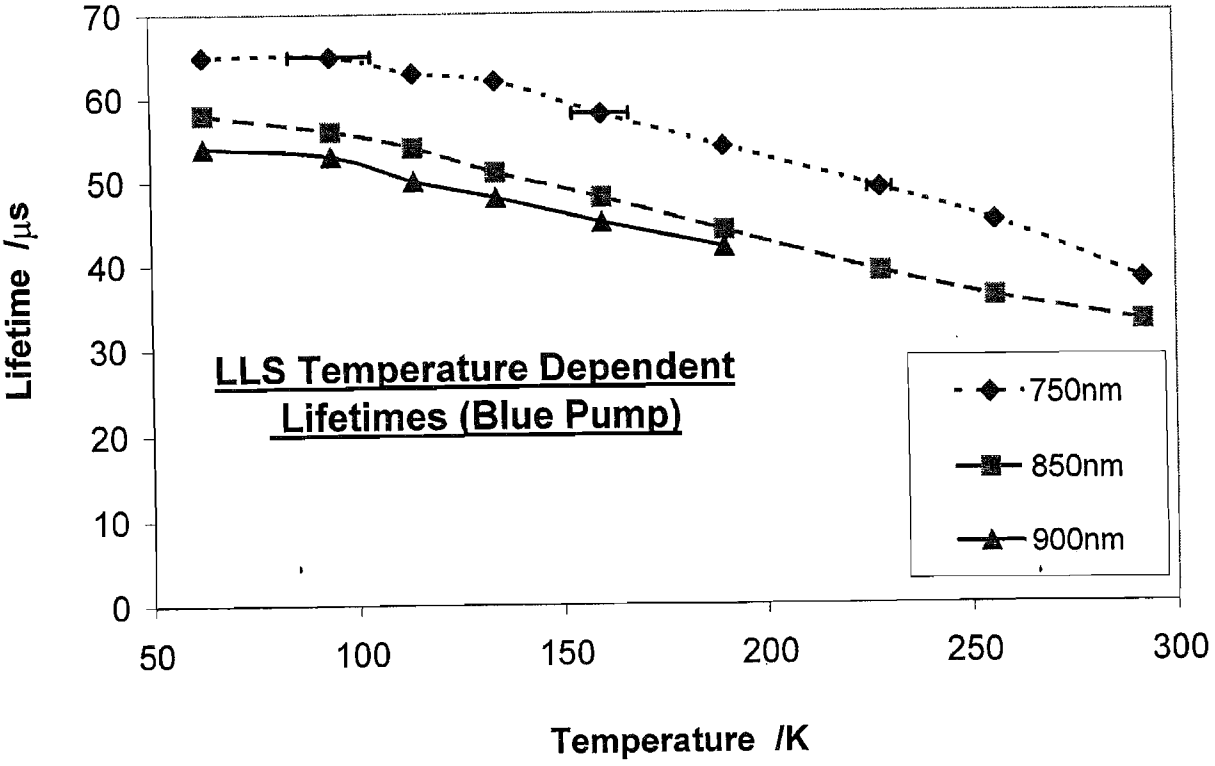

(In these figures the lines have been added as a guide to the eye)

to be caused by presence of dynamic odd parity distortions, increasing the radiative rate, and the increased occupancy of phonons assisting electrons over the potential barrier to the $^4T_2$ level. It is interesting to note how the stretch factor decreased so dramatically with temperature. This is showing that the decay was becoming increasingly non-exponential and stretched.

Figure 4.7 shows how the lifetimes of three wavelengths of emission for the $^4T_2$ to $^4A_2$ band, 750nm, 850nm and 900nm, were dependent upon temperature. Again it shows that non-radiative decay was stronger at higher temperatures and the lifetime was shorter. The longer the wavelength, the more likely it was emitted by an active ion from a site with a low crystal field or stronger electron-lattice coupling. These sites will have stronger non-radiative decay by the mechanism described in Section 2.6, explaining why the longer emission wavelengths have shorter lifetimes.

4.6.5 Room Temperature and Liquid Nitrogen Lifetimes

Room temperature lifetimes were investigated for all the samples using both red (633nm) and blue (488nm) pump light. Additionally, the lifetimes for the LLS samples immersed in liquid nitrogen with red pump light were measured.

The pump light, with less than 10mW in power, was chopped mechanically having a turn-off of 2μs. The collected fluorescence was sent through a monochromator (resolution = 10nm) set to a wavelength close to the emission peak (780nm) and was then detected by a PMT. Again single and double exponentials were found to fit very badly and stretched exponentials were used.

These results are displayed in Table 4.5 along with the QE. The stretch factor for a fit, which is a measure of the decay's non-exponentiality, is shown in brackets where it deviates from the value of 0.79. The lifetime measurements for the $^4T_2$ to $^4A_2$ band for Cr^{3+} in a LLS glass agreed well with the past literature but the values were significantly lower than that for crystalline hosts with lifetimes typically between 100 and 250μs[17]. The reason why glass has such a substantially shorter lifetime than crystals is twofold. Firstly, there is an increased non-radiative decay rate owing to smaller Dq (more open structure and covalent bonding) and an increased S (less rigid sites and covalent

bonding). Secondly, there will also be increased radiative decay due to the presence of odd parity static distortions.

The liquid nitrogen results show that the measured lifetime increased dramatically as the temperature decreased – in this case by about 60% compared to room temperature. Because the lifetimes correlate so well to the QE, the full analysis of room temperature lifetimes for different sample compositions is left to the next section.

4.6.6 Room Temperature Quantum Efficiency

The room temperature quantum efficiency was investigated for both red (633nm) and blue (488nm) pump light using the integrating sphere method described in detail in Section 3.5. The technique gave a consistent geometry for the collection of fluorescence and the setup was calibrated with a sample of known QE (GSGG). In order to have confidence in the result, a number of important corrections needed to be made. One of these corrections was for the reabsorption of fluorescence that would otherwise tended to lower the measured QE. The estimated corrections were 2.5% for the 0.015wt% Cr_2O_3 doped sample, 10% for the 0.05wt% doped samples, 15% for the 0.1wt% doped sample, and 20% for the 0.3wt% doped sample.

These results are displayed along with the lifetimes in Table 4.5. The first thing to note is that the QE correlated well to the measured lifetimes, which makes good sense considering Equation 4.2 and knowing the emission spectra and refractive indices were very similar. The second thing is that these QE values were lower than expected compared to the past literature (see Table 4.1). This was particularly true for the LLP sample although the exact composition in the reference was not known. During melting no special precautions were taken to remove water, following Reference 6 which got good results. (Section 4.6.6 investigates the concentration of OH within the samples.) As described in Section 3.5, determination of absolute value of QE is problematic. Many precautions had to be taken and corrections were made in order to minimise the error. There can be good confidence that the random error was effectively minimised by these measures as was demonstrated by a calculation of the standard deviation for the repeat results. This estimate of random error was found to be 0.2%. However, if the sample quality was poor or there was less fluorescence as was the case for AlP, LLS O, and LLS C(0.015) the random error was more like 0.5%. This indicates that the relative

QE results within this study can be accurately compared. It is much more difficult, however, to estimate the effect of systematic error. Since the reference sample had a QE approaching unity, it would not have been possible for an incorrect reference value to misleadingly raise the measured QE in this experiment.

Looking at the past literature, it is difficult to know whether all the corrections and precautions were made in these previous QE investigations. The effect of neglecting these corrections, in all the cases except reabsorption, would tend to misleadingly increase the measured QE. It is also possible that the discrepancy may have been caused by systematic error as an effect of QE measurement technique. Reference 8 used the integrating sphere QE measurement technique and investigated a soda-lime-silicate glass almost identical to the LLS O sample in this study. They measured a QE value of 9% - between 1 and 2% higher than LLS O sample measured here. However, they apparently made no correction for scattering and they would have had more severe problems with uncorrected reabsorption. These effects would tend to bring our results into line.

The QE for samples was found to be greater for the red pump than the blue pump. This is, of course, assuming that GSGG's QE remained constant for both pump wavelengths. This agreed with past papers[6] and was attributed to small non-radiative losses from the $^4T_1$ level.

There is no report in the literature of a measurement for the QE of Cr^{3+} in lead germanate. This was an interesting glass to investigate since it was known to make good fibre[12], it is a low phonon energy glass and barium sodium germanate had been reported as having good Cr^{3+} QE. However, these results reveal that $PbGeO_2$ glass has a QE of only 6% - a very ordinary value compared to the best glasses. This is further evidence that the non-radiative decay mechanism for transition metals in glass is quite different in nature from the multiphonon decay experienced by rare earths. It is notable from Table 4.4 that PbG had larger electron-lattice coupling than the other glasses, contributing to greater non-radiative decay.

	QE (%) Room Temp Red Pump (+/- 0.2)	τ (μs) Room Temp Red Pump (+/-0.5)	τ (μs) Liquid N_2 Red Pump (+/-0.5)	QE (%) Room Temp Blue Pump (+/- 0.2)	τ (μs) Room Temp Blue Pump (+/-0.5)
AlP	15.8 (+/-0.5)	27.1 (0.76)	-	12.0 (+/-0.5)	27.8
LLP	7.4	22.2 (0.73)	-	5.9	21.5
PbG	6.2	16.3 (0.72)	-	4.8	15.0
C(0.015)	15.3 (+/-0.5)	38.7 (0.79)	60.5	12.4 (+/-0.5)	37.8
C(0.05)	15.1	36.1 (0.79)	58.7	11.4	35.7
C(0.1)	14.7	34.2 (0.78)	57.3	11.5	34.0
C(0.3)	11.3	27.6 (0.76)	52.5	9.2	28.3
A	13.4	35.7	59.8	10.6	34.9
B	14.1	37.2	58.9	10.9	35.7
C	15.0	37.6	58.0	11.7	36.8
D	12.1	36.3	56.7	9.1	35.9
X	15.5	36.6	60.0	11.0	36.5
Y	14.0	37.5	58.0	10.8	35.7
Z	12.4	36.6	55.7	9.1	35.3
R	16.1	35.8	56.8	11.9	35.4
M	14.7	36.3	56.7	11.9	35.6
N	13.8	36.3	60.3	10.9	36.5
O	6.9 (+/-0.5)	29.6 (0.76)	58.3	8.6 (+/-0.5)	28.6
P	11.9	33.5	58.9	9.6	31.9

Table 4.5: Lifetimes and Quantum Efficiencies for the Cr^{3+} Glasses

It was evident from the results that for the most part, the QE did not change dramatically for the range of LLS samples chosen. This indicated that the original composition was quite close to being optimised. Originally, the compositions of the sixteen LLS samples were carefully chosen to form five groups, where each group investigated the effect of varying one particular element of composition. The following is an analysis of how these alterations affected QE and lifetime.

Samples C(0.015) – C(0.3)

These samples are the original composition of LLS with a range of Cr_2O_3 concentrations measured in weight %. These results show the effect of concentration quenching. Figure 4.8 shows a number of graphs: (i) Red-pump QE against Cr concentration, (ii) Red-pump lifetime against concentration and (iii) Red-pump rate of decay against concentration. The first graph shows that the effect of increasing the Cr density within the glass leads to concentration quenching, lowering the radiative QE. This quenching takes place even at very low Cr concentrations. It is important to note that when graphs (i) and (ii) are compared, the relative overall changes in QE and lifetime are not all that different, confirming the close relationship between the two.

The process of concentration quenching takes place because it is possible for energy to migrate from an excited ion to a non-excited ion by resonant dipole-dipole interaction[18]. The probability of this energy transfer process is proportional to R^{-6} where R is the distance between neighbouring active ions. The quenching process takes place by cooperative upconversion, by migration to an OH ion, or by migration to sites with large S or small Dq where there would be increased probability of non-radiative decay. Since the quenching rate is proportional to R^{-6}, this implies that the rate is proportional to the concentration, N, squared (since $R \sim N^{-1/3}$). This quenching is additional to the radiative decay giving a decay rate $\sim A_{21} + CN^2$ where A_{21} is the Einstein coefficient and C is a constant. Graph (iii), which shows the radiative rate against the concentration, can be interpreted as being consistent with this theory, where the constant C is relatively small. To be certain it would have been useful to have had an additional very high concentration point on the graph.

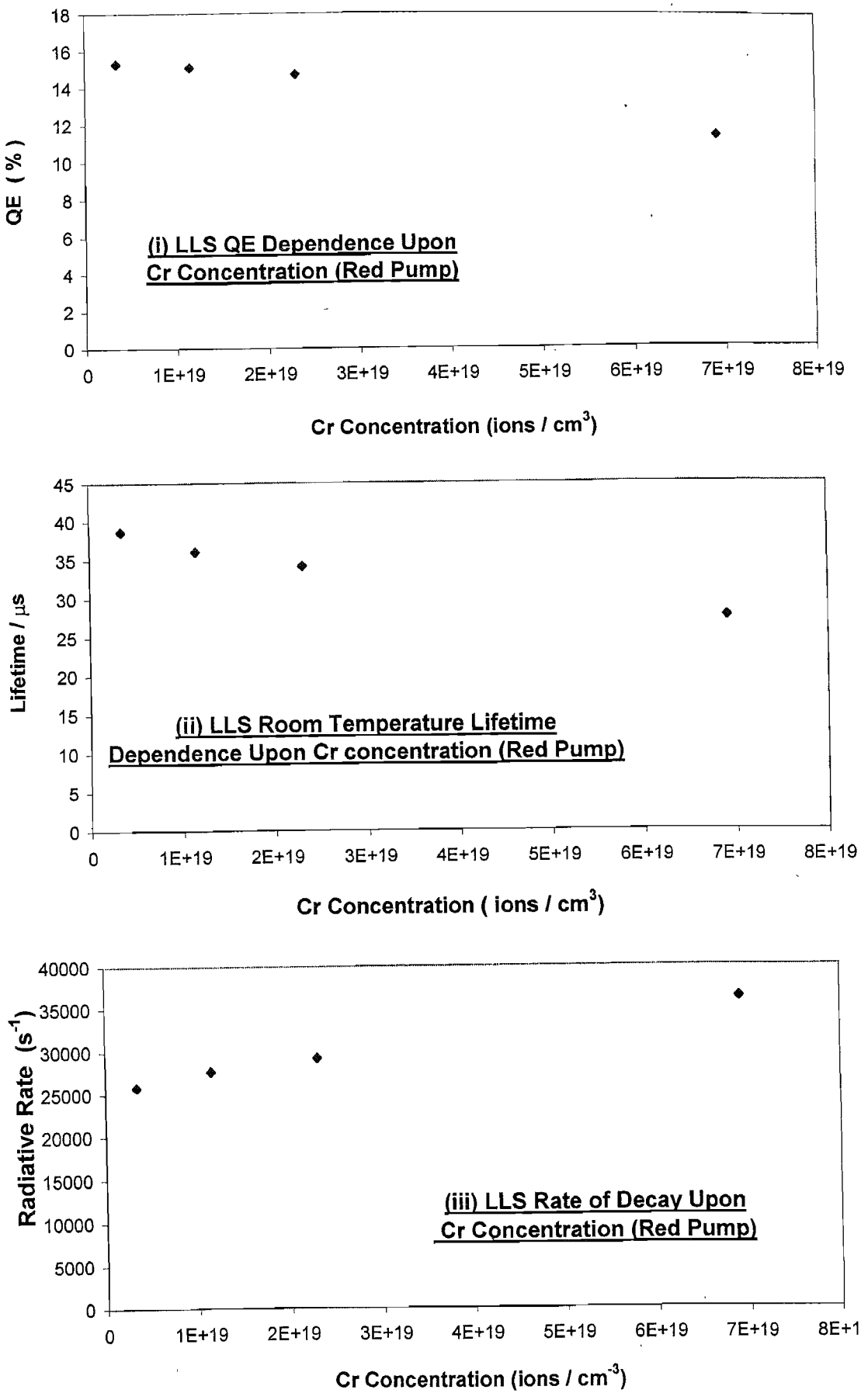

Figure 4.8: The Effect of Cr Concentration Upon LLS Lifetime and Quantum Efficiency

Sample A-D

Samples A to D varied the ratio of Li to Ca, with the original composition falling between B and C. The results show that C was the best for QE and τ, showing that the optimal composition will be close to the original LLS but with a bit more Ca and slightly less Li.

Samples X and Y

Samples X and Y varied the ratio of the Al and Si network formers. The results show that X had the best QE and τ, which suggest the optimal composition would contain no Al_2O_3.

Samples Z and R

Samples Z and R substituted La and B for the Al respectively. The results demonstrate that, in terms of QE, substituting to La is not a good idea but substituting to B may well be beneficial.

Samples M and N

These samples varied the overall ratio of network modifiers to formers. Here the results showed that the original composition was well optimised, with the small addition of modifiers having little detrimental effect on the spectroscopy.

Samples O and P

Sample O substituted the larger Na ion for Li, and sample P substituted the larger Ba ion for Ca. The results seem to confirm that the size of the modifying cation is very important for QE as put forward by Kisilev et al. in Reference 6. The idea here is that small, highly charged cations lead to a more rigid glass structure, reducing the non-radiative decay. Additionally, these two glasses were found to have the lowest crystal field strength out of the LLS samples (Table 4.3) which would also lead to a reduced potential barrier for non-radiative decay by level-crossing. The refractive index results (Section 4.6.8) suggest that there might have been some loss of Na_2O during the melting, changing the composition from the one intended.

4.6.7 Comparison of OH Content within the LLS Samples

It is well known that the presence of H_2O in oxide glasses can lower the radiative quantum efficiency owing to hydroxyl ions acting as traps[18]. The quenching rate will depend not only upon the concentration of Cr for energy migration as explained in the last section but will also be proportional to the concentration of OH. The coefficient of proportionality will depend upon the details of the host composition controlling how efficiently energy couples between the Cr and OH. Because of the lower than expected QE in the samples, an investigation into the OH content was carried out. Without knowledge of the coefficient of proportionality for the host, it was not possible to obtain an estimate of the quenching rate. However, it was still important to know that OH concentration did not vary across the LLS samples since any such variation could mean the samples' QE and lifetimes could not be compared without OH quenching giving misleading results.

Figure 4.9: OH Absorption for an LLS Sample

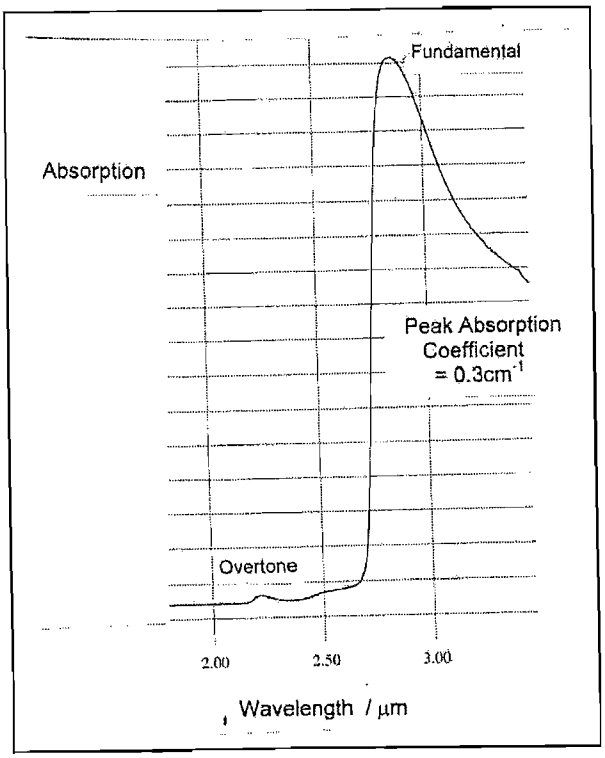

The OH content within the LLS samples was compared by measuring the strength of the fundamental OH absorption peak at 2.8µm[19]. This experiment was done with a Fourier Transform Infrared Spectrometer with the 5 x 5 x 3mm polished samples used for the QE investigation. Care was taken to avoid surface moisture on the samples, as H_2O also has absorption peaks close to 2.8µm[19].

The molar concentration of OH could be calculated by dividing the peak absorption coefficient by a known molar absorption coefficient of $20cm^{-1}$ for a similar soda lime silicate glass[20]. The OH concentration was found to be approximately $1x10^{19}$ ions/cm^3 which as expected for a glass melted in an open atmosphere is high. Despite the OH concentration being comparable to that of the Cr, it does not necessarily mean the OH quenching is strong – this depends on the details of the coupling strength between the two ions. However the OH concentration

for the samples was found to vary by only 5% of its absolute value. This shows the OH content varied by only 5% between the different LLS glasses, giving confidence that variations in the number of hydroxyl traps have not distorted the QE results.

4.6.8 Refractive Indices of the LLS Samples

Before any attempt at fibre fabrication could be made, it was important to know the refractive index of the glass that will become the core. This needed to be known in order to choose the cladding glass to give the desired numerical aperture, as well as being a parameter in the Fuctbauer-Landenburg equation for emission cross-section.

The refractive indices of all the LLS samples were measured using an Abbe Refractometer using light from a sodium lamp (589nm). This device required the samples to have a polished face and made use of the principle of total internal reflection. The results are displayed in Table 4.6.

Sample	Refractive Index (+/- 0.01)	Sample	Refractive Index (+/- 0.01)
C(0.015)	1.558	X	1.556
C(0.05)	1.560	Y	1.559
C(0.1)	1.558	Z	1.587
C(0.3)	1.557	R	1.557
A	1.550	M	1.570
B	1.551	N	1.538
C	1.563	O	1.533
D	1.567	P	1.571

Table 4.6:Refractive Indices of the LLS Samples

Understanding that refractive index depends in part on the mass of the ions within the glass, these results make good sense. The basic composition with different Cr concentrations, C(0.015) etc, have very similar refractive indices. The small differences give an idea of the random error caused either by the measurement technique or by the melting / quenching process. The samples' compositions were chosen so that there was always a logical progression, which explains the refractive index results. For instance,

for the samples A-D there is a monotonic increase in refractive index corresponding to the exchange for the light Li ion for the heavier Ca ion. Likewise sample Z, with the very heavy La ion, stands out as having by far the largest refractive index. There is, however, one anomalous result which is the O sample. Substituting Na for Li, this sample should have a larger refractive index than the basic composition C(0.05). This result is explained by the fact that NaO_2 sublimes at temperatures above 1275°C and would have at least in part boiled away during melting.

4.7 Calculation of the Cross-Section of Emission and the $\sigma_e\tau$ Product

For a given pump power and geometry of a gain medium, it is the product of the emission cross-section and the upperstate lifetime, $\sigma_e\tau$, that determines the overall gain of an amplifier. Using the results from this chapter it was possible to get a good estimate of this product as a function of wavelength which could then be used in a gain model presented in Chapter 7.

Using the Fuchtbauer-Ladenburg equation (Equation 4.2),

$$\sigma_e(\lambda) = \frac{\eta\lambda^5 I(\lambda)}{8\pi n^2 c\tau_m \int \lambda I(\lambda) d\lambda}$$

and using the relevant parameters for the original LLS glass C(0.05), the function for the cross-section of emission can be found. Results from Section 4.6.4 revealed that the measured lifetime was actually a function of wavelength. This dependence was ignored here on the assumption that the QE had a similar dependence on wavelength, which together cancel out. It should be noted that the figure for the measured lifetime used the stretched exponential fit and the refractive index was for 589nm rather than the near infrared.

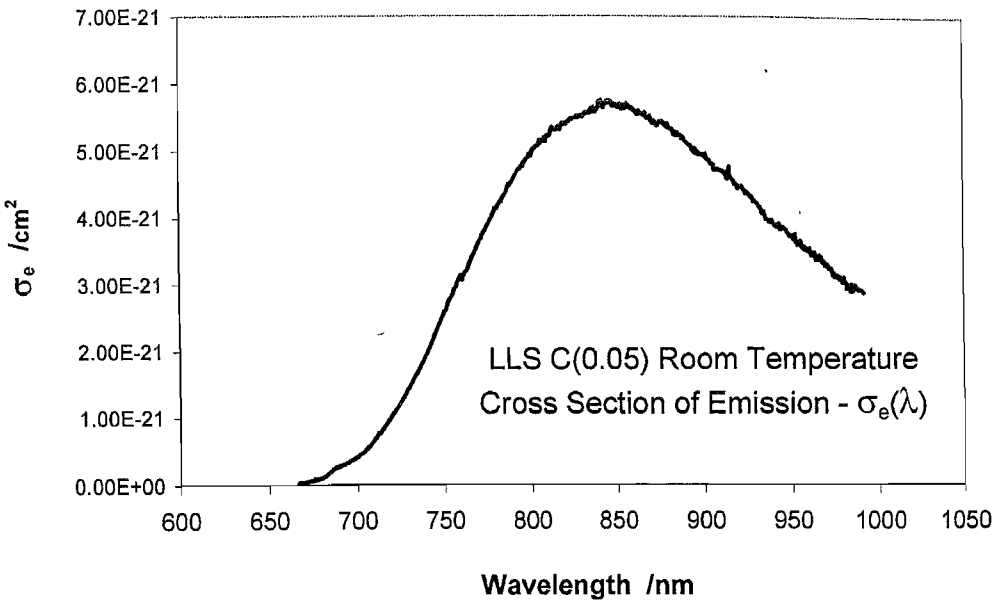

Figure 4.9

Figure 4.9 shows the calculated emission cross-section at room temperature. The peak is skewed 50nm to longer wavelengths compared to the emission profile by the λ^5 factor in the Fuchtbauer-Ladenburg equation. The value of the peak of emission cross-section for this LLS sample is $6 \times 10^{-21}cm^2$, which compares to typical crystalline values[17] of between $6x10^{-21}cm^2$ and $20 \times 10^{-21}cm^2$. LLS falling at the lower end of this range is explained by the slightly broader emission profile for the glass.

It is interesting to note that the absorption cross-section has been measured as being about nine times bigger than the emission cross-section. One might expect only a factor of three due to the three-fold degeneracy of the triplet $^4T_2$ state. However, the width of the absorption transition is substantially narrower than the emission transition in frequency terms, indicating a steeper parabola for the ground state. This will have the effect of decreasing the peak value of emission cross-section. Additionally, although the parameters taken for the calculation of the emission cross-section were the best available they are likely to lead to an underestimate. For instance, the refractive index, which is squared in the Fuchtbauer-Ladenburg formula, was for 589nm instead of the longer emission wavelengths. Normal dispersion will mean the actual value is somewhat smaller as well as varying across emission profile. The lifetime was measured with a stretched exponential and it is even possible that the QE is slightly higher in line with some of the past literature.

Calculating the $\sigma_e\tau$ product gives a coefficient of merit with which potential gain media can be fundamentally compared. Here, the peak value of $2 \times 10^{-25}cm^2s$ for LLS C(0.05) can be compared to typical crystalline values[17] of between $8 \times 10^{-25}cm^2s$ and $14 \times 10^{-25}cm^2s$. Because the upper state lifetime is dependent on wavelength (Section 4.6.4 showed that the shorter the emission wavelength the longer the lifetime) the profile for $\sigma_e\tau(\lambda)$, similar to the gain profile, will be slightly skewed towards shorter wavelengths when compared to $\sigma_e(\lambda)$. However, all this assumes the absence of signal excited-state absorption (ESA) which would lower the effective value of emission cross-section and distort its profile (see Section 7.4).

4.8 Summary

The first stage of development of a Cr^{3+} fibre laser was the selection of promising host glasses. Generally, the radiative quantum efficiency of Cr^{3+} doped glass is very poor (often less than 5%) due to a thermal quenching mechanism. This chapter reports the spectroscopic investigation of Cr^{3+} doped lithium lime silicate glass (LLS) – a particularly promising glass for a fibre laser. Relatively easy to melt, LLS was reported in the literature as having one of the highest QEs amongst glasses, which will lead to an increased $\sigma_e\tau$ product.

A large range of bulk samples was fabricated, based upon the LLS composition from the literature. The compositions were carefully selected so that the QE could be optimised, the effect of Cr concentration could be investigated, and the Kisilev's theory for the effect of the modifying cations' size on the QE could be tested.

The spectroscopic evaluation included absorption and temperature dependent emission spectra, temperature dependent and emission wavelength dependent radiative lifetimes, quantum efficiency and refractive index measurements. Wherever possible the results were linked to transition metal theory and the important parameters for a potential fibre device have been found. These include QE of 15%, lifetime of 36μs, refractive index of 1.56 for the basic composition of LLS. These numbers lead to a calculated value for the peak cross-section of emission of $6 \times 10^{-21}cm^2$.

One of the most notable features of the results was that the basic composition of LLS was already quite close to being optimised. Only small changes in certain elements of the composition brought benefits to the spectroscopy, but more often quite large changes had little effect on the QE.

---

[1] "General Procedure for the Analysis of Er^{3+} Cross Sections", W J Miniscalo and R S Quimby, Optics Letters, **16**, (4), 258 (1991)

[2] "Vibronic Interactions in Nd:YAG Resulting in Nonreciprocity of Absorption and Stimulated Emission Cross Sections", B F Aull, H Jenssen, Journal of Quantum Electronics, **18**, (5), 925 (1982)

[3] "Disorder and Optical Spectroscopy of Cr^{3+} Doped Glass: I Silicate Glasses", F Rasheed, K O'Donnell, B Henderson and D Hollis, J. Phys. Condens. Matter, **3**, (12) 1915 (1991)

[4] "The Optical Spectroscopy of Chromium in Ed-2 Silicate Glass", F J Bergin, J Donegan, T Glynn and G Imbusch, Journal of Luminescence, **34**, 307 (1986)

[5] "Optical Properties of Chromium (III) in Fluoride Glasses", M A Illarramendi, R Balda and J Fenandez, Journal of Luminescence, **48 + 49**, 579 (1991)

[6] "Spectral Characteristics and Fluorescence Quantum Efficiencies of Cr(III) in Phosphate and Silicate Glasses with Li and Be Modifiers", A Kiselev and R Reisfeld, Solar Energy, **33**, (2), 163 (1984)

[7] "On the Quantum Efficiency of Chromium Doped Glasses", G F Imbusch, T Glynn and G Morgan, Journal of Luminescence, **45**, 63 (1990)

[8] "Quantum Eficiencies of Chromium Doped Glasses", M J Payne and N Lowde, Physics and Chemistry of Glasses, **32**, (5), 222 (1991)

[9] "Germanate Glasses as Hosts for Luminescence of Mn^{2+} and Cr^{3+}", A Van Die, A Leenaers, G Blasse and W Van der Weg, Journal of Non Crystalline Solids, **99**, 32 (1988)

[10] "Spectroscopy and Photokinetics of Chromium (III) in Glass", L J Andrews, A Lempicki and B McCollum, J. Chem. Phys., **74**, (10) 5526 (1981)

[11] "Luminescent Solar Concentrators for Energy Conversion", R Reisfeld and C Jorgensen, Structure and Bonding, **49**, 1 (1982)

[12] "New Class of Fibre Laser Based on Lead Germanate Glass", J R Lincoln, C Mackechnie, J Wang, W Brocklesby, R Deol, A Pearson, D Hanna and D Payne, Electronics Letters, **28**, (11), 1021 (1992)

[13] "Antiresonance in the Optical Spectra of Transition Metal Ions in Crystals", M D Sturge and J Guggenheim, Physical Review B, **2**, (7), 2459 (1970)

[14] "Spectroscopic and Laser Properties of Ce^{3+}-Cr^{3+}-Nd^{3+} Co-Doped Fluoride Phosphate and Phosphate Glasses", W Seeber, D Ehrt and H Ebendorff-Heidepriem, Journal of Non-Crystalline Solids, **171**, 94 (1994)

[15] "Disorder and the Optical Spectroscopy of Cr^{3+}Doped Glasses: I. Silicate Glasses", F Rasheed, K O'Donnell, B Henderson and D Hollis, J. Phys. Condens. Matter, **3**, 1915 (1991)

[16] M Yamaga, Y Gao, K O'Donnell and B Henderson, Journal of Luminescence, **53**, 457 (1992)

[17] "Quantum Electronic Properties of the $Na_3Ga_2Li_3F_{12}$:Cr^{3+} Laser", J Caird, S Payne, P Randall Staver, A Ramponi, L Chase and W Krupke, Journal of Quantum Electronics, **24**, (6), 1077 (1988)

[18] P M Peters and S Houde-Walter, Journal of Non-Crystalline Solids, **239**, 162 (1998)

[19] "Fluoride Glass Optical Fibres", P France, Blackie p135

[20] "The Determination of Hydroxyl by Infrared Absorption in Quartz, Silicate Glasses and Similar Materials", M Paterson, Bull. Mineral, **105**, 20-29 (1982)

Chapter 5

Theory of Passive and Active Fibre Devices

The first section of this chapter gives a brief summary of passive waveguide theory, leading to a description of the optical modes that propagate along a fibre. The second section introduces a simple model for the small-signal single-pass gain for a four level system.

5.1 Passive Waveguide Theory

The solutions to Maxwell's equations for a perfectly cylindrically symmetric optical fibre with a core of diameter 2a, with a refractive index n_{core}, surrounded by a cladding of infinite extent and lower refractive index n_{clad} consist of a finite number of guided waves known as modes of the fibre. Each mode will, in general, have different phase and group velocities. While exact mathematical solutions to the equations do exist, they can be greatly simplified[1,2] for the case $n_{core} - n_{clad} << 1$ (which is known as the weakly guiding approximation and is applicable here to optical fibres). The result is linear polarised modes, or LP_{lm} modes, where the positive integers l and m denote the order of the modes. These modes are to a good approximation transversely polarised, with each dominated by one transverse electric field component and one transverse magnetic field component. The normalised intensity profiles for the LP_{lm} modes are f(r, θ) =

$$AJ_l^2\left(\frac{ur}{a}\right)\cos^2(l\theta) \qquad A\frac{J_l(u)}{K_l(w)}k_l^2\left(\frac{wr}{a}\right)\cos^2(l\theta)$$

$$\text{for } r < a \qquad \text{for } r > a \qquad 5.1$$

where J_l is a Bessel function, k_l is a modified Hankel function (both of order l) and A is a normalising coefficient. The parameters u and w are solutions of the characteristic equation[1],

$$\frac{uJ_{l+1}(u)}{J_l(u)} = \frac{wK_{l+1}(w)}{K_l(w)} \qquad 5.2$$

and are defined as

$$u = a(k^2 n_{core}{}^2 - \beta^2)^{1/2} \qquad w = a(\beta^2 - k^2 n_{clad}{}^2)^{1/2} \qquad 5.3$$

where β is the propagation constant of the mode and k is the free space wavenumber ($2\pi/\lambda$). The condition on the propagation constant β of a confined mode is that

$$n_{core}k > \beta > n_{clad}k \qquad 5.4$$

which indicates that the effective refractive index experienced by the mode is β/k, and it lies between that of the core and the cladding. The normalised frequency, or V-number, of the fibre is given by

$$V^2 = u^2 + w^2 \qquad 5.5$$

All the properties of the fibre modes are determined by the value of this parameter and in particular the number of guided modes that are supported by the fibre. Combining 5.3 and 5.5 gives

$$V = ka(n_{core}{}^2 - n_{clad}{}^2)^{1/2} = \frac{2\pi a}{\lambda}(\text{N.A.}) \qquad 5.6$$

where N.A. is the fibre numerical aperture. For V values less than 2.405, only one solution – the LP_{01}- is allowed to propagate and the fibre will be single mode for that wavelength. Above this, the fibre is multimode, supporting an increasing number of modes at high V-values. As each transverse mode approaches cut-off (corresponding to the V parameter approaching 2.405), the radial intensity distribution of that mode spreads further out into the cladding of this fibre and therefore experiences a higher loss through bends and core-clad interface imperfections. Although the LP_{01} mode does not have a cut-off wavelength, V values smaller than about 1.7 are impractical for supporting low-loss propagation. This therefore defines a range of V values for which single-mode operation can occur effectively.

While LP_{lm} solutions can be solved for particular fibre geometries and signal wavelengths, the calculation is very involved. For the purposes of the modelling of active fibres described later, it is more convenient to make some simplifications regarding the waveguide modes. When just considering the fundamental mode, which experiences the least loss, the resemblance of the LP_{01} mode profile to a gaussian function enables a further simplification to be made. For a step index fibre the equivalent spot size can be approximated by a gaussian distribution[3] as

$$\omega = \frac{a}{(\ln V)^{1/2}} \qquad 5.7$$

and the intensity distribution for the LP_{01} mode can be written as

$$f(r) = \frac{2}{\pi\omega^2}\exp\left(\frac{-2r^2}{\omega^2}\right) \qquad 5.8$$

The fraction of mode power confined within the core is given by

$$\eta_p = \int_{\theta=0}^{2\pi}\int_{r=0}^{a} f(r)\,r\,dr\,d\theta = 1-\exp\left(\frac{-2a^2}{\omega^2}\right) \qquad 5.9$$

However, at high V-values, the large number of modes supported by the waveguide allows the intensity distribution across the core of a fibre to be taken as a top hat function with a width equal to the core diameter[4].

5.2 Active Waveguides

When investigating gain, the pump intensity will be large enough to be comparable with the saturation intensity

$$I_s \approx \frac{h\nu_p}{\sigma_a \tau} \qquad 5.10$$

where σ_a is the absorption cross-section and τ is the upper level lifetime, so that there is a significant depletion of the ground state. This will mean the absorption length within the fibre will be much longer than the bulk absorption length. Consequently, the effect of non-uniform absorption and gain (occurring only in the doped core and not in the cladding) can be treated as a small perturbation to the waveguide equations of the last section and they are still valid for active fibres.

The small-signal single-pass gain in a four-level lossless amplifier of length L can then be written as[4]

$$\frac{P_s(L)}{P_s(0)} = \exp\left(\frac{\sigma_e \tau P_{abs}}{h\nu_p A_{eff}}\right) \qquad 5.11$$

where P_s is the power of the signal, σ_e is the emission cross-section, τ is the observed fluorescence lifetime, $h\nu_p$ is the pump photon energy and P_{abs} is the usefully absorbed pump power within the core. A_{eff} is the effective area, which corresponds to the transverse overlap between the dopant profile, pump and signal modes. Approximations exist to calculate A_{eff} for single mode fibre[5]. However, for a highly multimode fibre, such as the one fabricated in this project, a good approximation is to use the area of the core. Interestingly, for this lossless fibre model, the gain is independent of the fibre length and depends purely on the pump power absorbed.

5.3 Potential For Gain in LLS Fibre

Using the $\sigma_e\tau$ results for LLS C(0.05) glass reported in Section 4.7, this simple model for gain (Equation 5.11) can be used to confirm that the fundamental idea of a Cr^{3+} doped glass fibre laser is reasonable and worthy of further investigation. Table 5.1 shows the calculated single pass gain for a variety of usefully absorbed pump powers and fibre core diameters. The effective area was taken to be the core area, the pump wavelength was assumed to be 600nm and $\sigma_e\tau$ was $2 \times 10^{-25} cm^2 s$.

		Usefully Absorbed Power		
		10mW	50mW	100mW
Fibre Core Diameter	3μm	9%	53%	230%
	5μm	3%	17%	36%
	10μm	1%	4%	8%

Table 5.1: Calculated Gain for a LLS Fibre with Various Core Diameters and Usefully Absorbed Pump Powers

Table 5.1 shows clearly that the small signal gain increases profoundly as the fibre core diameter decreases or the usefully absorbed pump power increases. This simple model gives a good indication that a Cr^{3+} fibre laser could have a feasible threshold pump power. However, in reality the situation is not as simple as this and the single pass gain could be expected to be somewhat lower.

The pump power used in the calculation was that usefully absorbed after fibre loss and excited state absorption (ESA) at the pump wavelength. Importantly, what has been neglected are the mechanisms that bring about loss of signal photons which include fibre loss, reabsorption of emission and ESA at the signal wavelengths. Excited state aborption, particularly, can often be a significant problem for gain media using transition metals because of the broad transitions. If the ESA is strong in the fluorescent region then the anticipated gain will be much reduced and maybe rule it out all together. Section 7.4 reports an ESA investigation in a section of LLS fibre.

[1] D Gloge, Appl. Opt., **10**, 2252 (1971)
[2] "Optical Electronics", A Yariv, Holt-Saunders, 3rd edition (1985)
[3] "Optical Waveguide Theory", A W Snyder and J D Love, Chapman and Hall, (1983)
[4] "Theoretical Analysis of Optical Fibre Laser Amplifiers and Oscillators", M J F Digonnet, and C Gaeta, Appl. Opt., **24**, 333 (1985)
[5] "An Investigation of Laser Action in Single Mode Fibre Lasers", M W Philips, PhD thesis, University of Southampton, (1989)

Chapter 6

Lithium Lime Silicate Fibre Fabrication

6.1 Introduction

There are no reports in the literature of any group pulling lithium lime silicate fibres, and it is certainly not the case that one can draw a core-clad optical fibre from any glass with promising spectroscopic characteristics. It is vital that the glass under consideration has the right thermal properties and also has a compatible cladding glass for drawing to be possible. The reason for this is that there must be a temperature for drawing where firstly the viscosity of both core and cladding is in the right range for forming a fibre and additionally both glasses must not crystallise at or below this temperature. Figure 6.1 shows diagrammatically how these conditions must be satisfied simultaneously.

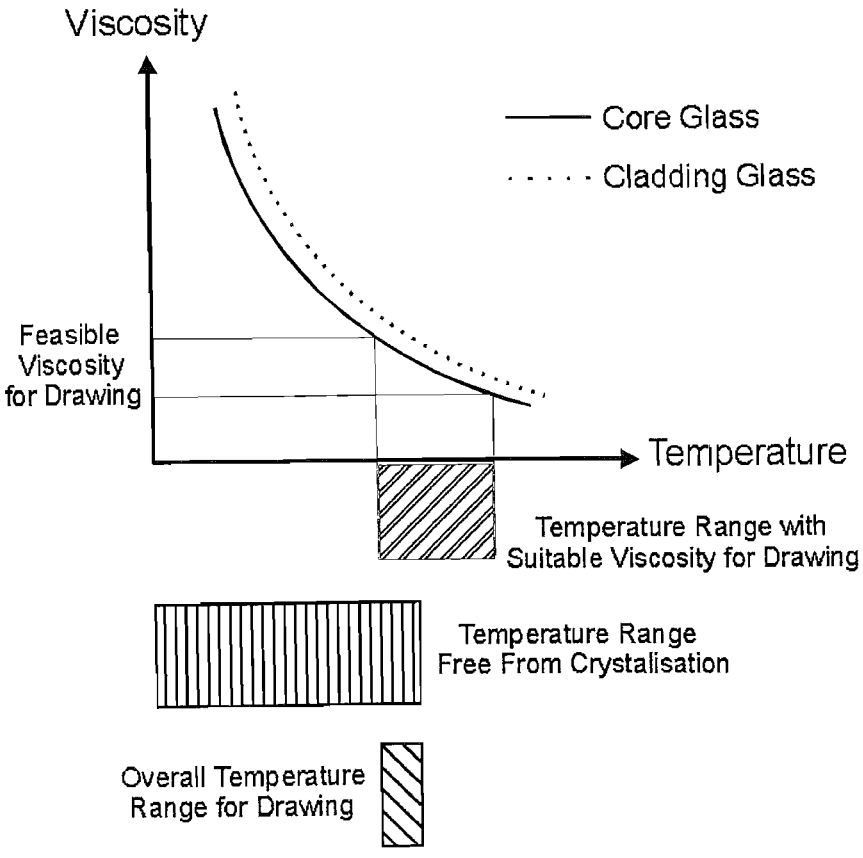

Figure 6.1: Constraints for Fibre Drawing

These conditions are very constraining and fibre drawing tends to be easily possible only for stable glasses resistant to crystallisation. Note that on Figure 6.1 that although the viscosity of core and cladding are similar, the core viscosity is slightly lower at the pulling temperature. This ensures a good collapse where the core does not get left behind with the preform. Moreover, a strong optical fibre, which is resistant to fracture, has a core glass with a slightly larger expansion coefficient than the cladding, so that upon cooling the fibre is under compression and cracks do not easily propagate.

For this project, it was obviously every bit as important to ensure that glasses had these correct thermal characteristics as well as to optimise the spectroscopy. It was partly for the expected ease of fibre drawing, that lithium lime silicate was initially favoured over the other glass candidates with good Cr^{3+} quantum efficiency (see Table 4.1).

Once the thermal properties of the core and cladding glasses are found to be suitable and a fibre can be drawn, there are still important decisions to be made for parameters influencing the prospect of gain. The first important variable is the composition of the core glass affecting its spectroscopy and refractive index. Secondly, the refractive index of the cladding glass must be chosen determining the numerical aperture of the fibre. Thirdly, the dimensions of the core and cladding must be selected. Finally, there will be different options for the techniques during the various stages of fabrication having consequences for the overall fibre loss. All these considerations are dealt with in the first half of this chapter and then there is a detailed account of the rod and tube method used to fabricate the fibre.

6.2 Thermal Properties

6.2.1 Thermal Expansitivity of LLS

The expansion coefficients for the LLS glass samples were measured using a commercial thermo-mechanical analyser[1] (Perkin-Elmer TMA7) with a high displacement sensitivity (up to 50nm) and a temperature range up to 1000°C. The samples were 5x5x3mm cuboids and they were held between two parallel plates of inconel, 0.1mm thick and 8mm in diameter. The thickness as a function of time and temperature was recorded as the temperature was increased at a rate of 10°C /min under

a constant force of 10mN. The procedure was to first measure the expansion coefficient of the inconnel plates before that of the sample and plates together so that the expansion coefficient of the sample alone could be extracted. The expansion coefficient was calculated directly from the TMA software. Figure 6.2 shows a typical curve for this expansion measurement and Table 6.1 gives the expansion coefficients at about 450°C for a selection of the LLS samples.

Figure 6.2

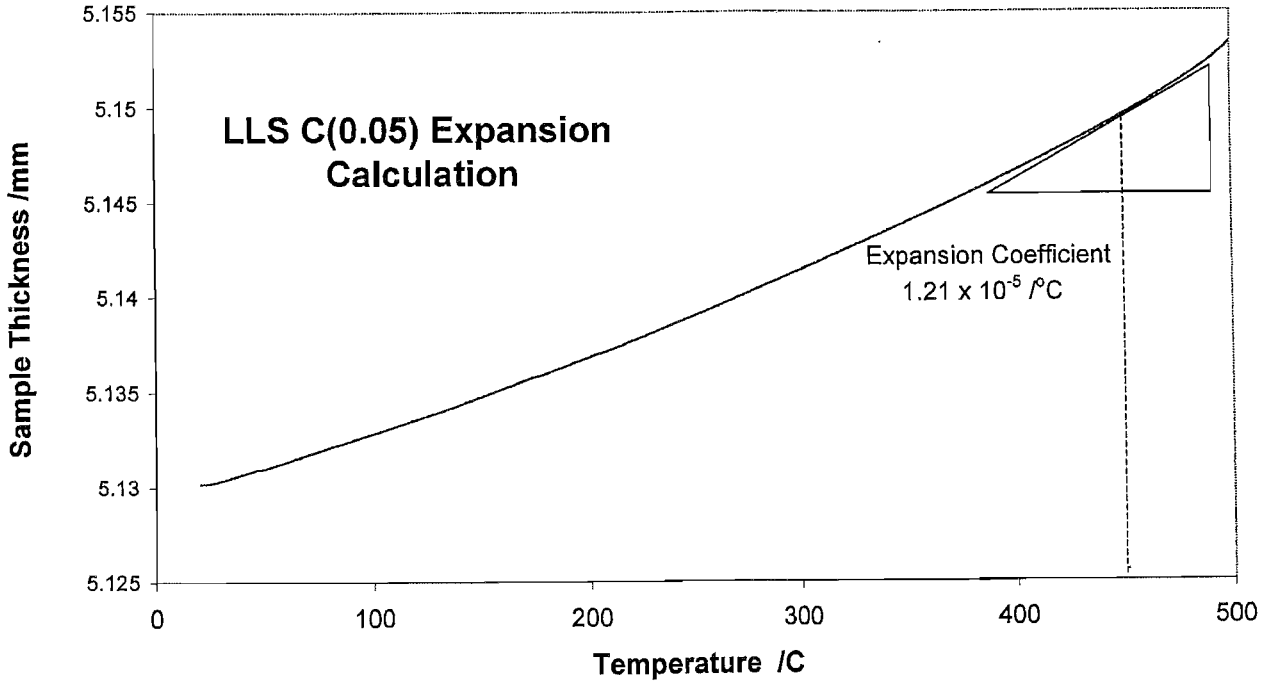

LLS SAMPLE	*EXPANSION COEFFICIENT @ 450°C*
LLS C(0.05)	1.21×10^{-5} /°C
LLS C	1.04×10^{-5} /°C
LLS X	1.36×10^{-5} /°C
LLS M	1.20×10^{-5} /°C
LLS R	1.21×10^{-5} /°C

Table 6.1: Expansion Coefficients at 450°C for a Selection of LLS Samples

Apart from the consequences for fibre strength, the expansion coefficient affects the difficulty of annealing samples. Table 6.1 shows that the interesting LLS compositions for fibre fabrication all had similar expansion coefficients.

6.2.2 The Glass Transition and Crystallisation Temperatures

The method used to determine the key temperatures for the glass transition and the onset of crystallisation was Differential Thermal Analysis[1] (DTA). This technique is based on measuring the difference in temperature between two alumina cups, both of which are at the centre of a uniform temperature furnace. One cup holds an inert material (alumina powder) and the other holds a small piece of glass of known mass, contained in alumina powder to provide good thermal contact. As the furnace's temperature is ramped up, any changes in the glass that require the release or absorption of latent heat are recorded as a function of temperature.

From a DTA trace various important temperatures can be found: the *glass transition* (T_g), the *onset of crystallisation* (T_x), the *peak of crystallisation* (T_p) and the *melting point* (T_m). Good indicators[1] for whether a glass is suitable for fibre drawing are that the separation of T_g and T_x should be large and the width of the crystallisation peak T_p-T_x should also be large. These criteria can be explained as follows:

Fibre drawing needs to take place at a temperature greater than T_g where the glass is in its liquid phase and able to be worked. If T_x-T_g is small, the material will tend to crystallise at or before drawing, and may not draw at all. Where drawing is possible, the suitable temperature range will be small making it difficult to find a cladding glass with compatible thermal and optical properties. When the width of the crystallisation peak is large, if some crystallisation does take place it will continue only slowly whereas a small T_p-T_x results in fast crystallisation making the fibre difficult to draw, particularly if T_x-T_g is small.

An approximate guide[7] for the pulling temperature of an oxide glass is $T_g + 2/3(T_x-T_g)$. Obviously, the greater the separation between the pulling temperature and T_x the easier it will be to find a suitable cladding glass and avoid fibre crystallisation.

Figure 6.3

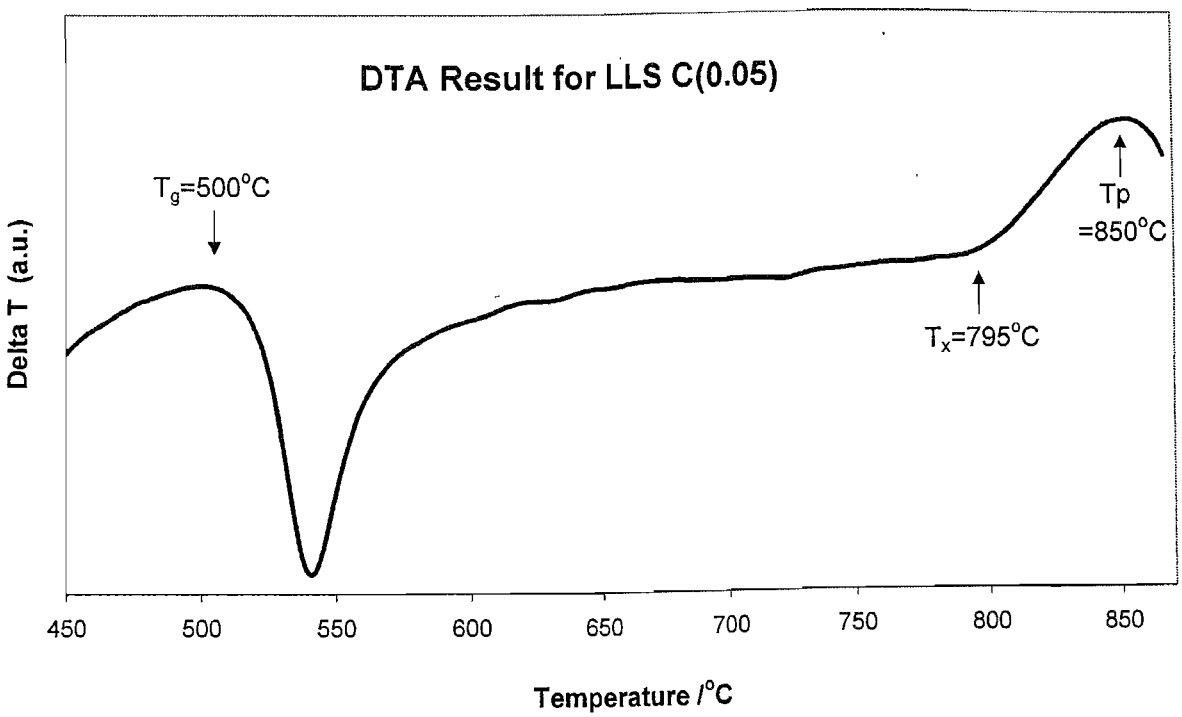

Figure 6.3 shows the DTA result for the basic composition of LLS C(0.05) which was representative of all the LLS samples. It showed the position of T_g as a kink in the DTA trace at about 500°C. A knowledge of T_g was important for the process of annealing. The onset of crystallisation was revealed as being at 795°C. This made LLS, with its T_x-T_g approaching 300°C, a particularly stable glass and an excellent prospect for fibre drawing.

6.3 Optimising the LLS Core Composition

Given that the thermal properties for LLS were so favourable for fibre drawing, it brought a great deal of flexibility in the exact composition for the core without concern over its drawability. The major theme of Chapter 4 was the spectroscopic investigation of a number of LLS samples with subtle variations in composition from the original one. The most important results of that chapter were how the value of $\sigma_e\tau$ product, the spectroscopic parameters in the model for gain, depended upon composition. It was found that the basic composition was already quite close to being optimised. Only small changes in certain elements of the composition could bring benefits to the spectroscopy, but more often quite large changes had little effect on the QE.

6.3.1 Overcoming the Problems of Extrinsic Scattering Loss

Successful fibre fabrication trials confirmed that LLS was an excellent glass for drawing without big problems of crystallisation. However, it quickly became apparent that fibre loss was a major problem for small-cored fibre and improvements would need to be made. There are many different causes of fibre loss and they can be separated into four broad categories as shown in Table 6.2.

Table 6.2: Mechanisms of Fibre Loss

Intrinsic Absorption	***Extrinsic Absorption***
e.g. UV-Edge Lattice Vibrations and Overtones	e.g. Transition Metals Rare Earths OH
Intrinsic Scattering	***Extrinsic Scattering***
e.g. Rayleigh Scattering	e.g. Bubbles Crystals Particulate Contaminants Undissolved Constituents

Extrinsic losses will vastly dominate the intrinsic ones for LLS in the near IR. Intrinsic loss mechanisms, governed purely by the composition, could not be mitigated, but important precautions could be taken to minimise the effects of the extrinsic loss mechanisms and reduce the overall fibre loss.

Extrinsic absorption due particularly to unwanted TM ions, which will have very broad absorption bands, could be reduced simply by using very high purity starting constituents. Additionally, OH content could be reduced simply by taking the precaution of evaporating the water content from the powders at the start of melting. The biggest extrinsic losses, though, were thought to be scattering caused primarily by

bubbles and also scattered losses associated with the core-clad interface. Certainly studying pieces of bulk LLS, there were clearly tiny bubbles within the glass, perhaps tens of microns in diameter.

The Mie theory of scattering[2] describes the scattered power in circumstances such as these. In the relevant case where the scattering centres are larger than 2μm and have a refractive index close to 1, the scattering loss will be proportional to the number of scattering centres, inversely proportional to the fibre's core radius squared and independent of wavelength for visible and near IR light.

Towards the end of the project much of the work was directed towards developing a technique to produce bubble-free LLS as the precursor to a low loss fibre. The technique finally used, involved a two pronged approach. First of all, a careful refining schedule was employed during the glass melting, which is described in detail later in Section 6.5. Secondly, there was an adjustment in the composition, knowing that there was a degree of latitude in the thermal and spectroscopic properties. The idea behind this modification is now explained.

Bubbles in glass are created during melting by the decomposition of the starting materials (e.g. Li_2CO_3 to Li_2O and CO_2) releasing gas, or by the condensation of dissolved gas within the melt[6]. Once bubbles have formed during melting, they have to escape to the surface otherwise they will remain when the glass is cast. At the casting temperature of 1400°C, LLS was still quite viscous (about 100 poise - a consistency similar to engine oil). If by subtly changing the composition so that the viscosity was lowered, without detrimentally affecting the other thermal or spectroscopic characteristics, the bubbles could escape more easily. This strategy was achieved by increasing the overall ratio of modifiers to formers, like the LLS M sample in Chapter 4, and partially substituting B_2O_3 for Al_2O_3 similar to the LLS R sample. The reason this last change worked, was that the melting and boiling point of B_2O_3 is significantly lower than that of Al_2O_3.

Looking back at Chapter 4, it can be seen that the spectroscopy of samples LLS M and LLS R was at least as good as the basic composition LLS (C0.05). Small additional changes were made taking the basic composition towards LLS X and LLS C as the

results from Chapter 4 indicated marginal benefits in the spectroscopy. A further DTA experiment was performed revealing that these compositional alterations could be made with only minor changes in T_x (775°C) and T_g (495°C). It followed that these changes could be met without detrimental effects for fibre drawing.

6.3.2 The Dopant Concentration in the Core

Chapter 4 included an investigation of the dopant concentration of Cr^{3+} on the quantum efficiency for the basic LLS composition. It revealed that concentration quenching began to reduce the radiative quantum efficiency even at quite low dopant concentrations such as 0.05wt%. Although the $\sigma_e\tau$ product would be maximised when the concentration was low enough so that quenching does not take place, this would not be the best dopant concentration to choose for a useful fibre. The lower the dopant level, the longer the fibre required to absorb a certain fraction of the pump power because of the reduced absorption coefficient. However, the longer the fibre, the bigger the overall fibre loss, so in practice there is a trade-off between minimising the device length and optimising the spectroscopic parameters. This would be true, to different extents, for both gain experiments and optimising a fibre laser.

If it had been possible to know the fibre loss before it was fabricated, it would have been possible to optimise the dopant concentration to maximise the absorbed pump power. As it was, the Cr_2O_3 dopant concentration was chosen to be 0.07wt% - a little bit higher than where concentration quenching starts taking effect (see Figure 4.8).

6.4 The Choice of Cladding Glass and Fibre Geometry

6.4.1 Cladding Glass

As explained in the introduction to this chapter, it was vital that the thermal properties of the cladding glass were compatible with the core glass so that the process of fibre drawing was feasible. Apart from this, the choice of refractive index for the cladding controlled the fibre's numerical aperture (N.A.) according to the formula,

$$N.A. = (n_{core}^2 - n_{clad}^2)^{1/2} \qquad 6.1$$

The N.A. was important as its value plays a role in:

i) Setting the number of transverse modes that can propagate along the fibre.

ii) Controlling the degree of pump and signal confinement within the core.

iii) The ease with which light can be coupled into the fibre.

A commercial glass was chosen for the cladding. The advantage here was that the glass quality was very good, and the thermal and optical properties were well known. Table 6.3 compares the key optical and thermal properties of the composition of LLS finally chosen for the core (see Section 6.5.1) and LLF2 – the Schott glass selected for the cladding.

Table 6.3: Optical and Thermal Properties of the Core and Cladding Glasses

	LLS Core Glass	Schott LLF2 Cladding Glass[3]
Refractive Index (λ=589nm)	1.563	1.541
Expansion Coefficient ($x10^{-5}$ /°C)	1.0 (T=300°C)	0.91 (T=300°C)
Glass Transition Temperature (°C)	495	440
Fibre Caning Temperature (°C)	670	675

Using Equation 6.1, the numerical aperture (at 589nm) could be calculated as 0.26. Such a fibre will be strongly guiding, giving a good margin for error, as each glass's dispersion characteristics will be different; the important N.A. values are actually for the emission and pump wavelengths. Table 6.3 shows a higher expansion coefficient for the core glass than for the cladding, so the fibre should be strong. Also the temperatures required for caning of each glass, found during trials of fibre drawing, were quite well matched with the core glass value slightly lower.

This N.A. value was quite high giving excellent pump and signal pump beam confinement of the fundamental mode to the core (~99% for 600nm pump light in a 5μm diameter core)[4] but both beams will be multimode for a sensibly sized core (6 modes for 600nm pump light in a 5μm diameter core)[4]. Ideally one might choose a single mode fibre because the triple overlap between the pump beam, signal beam and dopant profile will be at a maximum. Coupling into the higher order modes will mean that a greater fraction of the light will not be confined to the core. However, to create monomode fibre at these wavelengths, either the N.A. must be much lower or the core diameter would need to be less than 2μm. Both of these options would mean effective pump coupling into the fibre would become problematic.

6.4.2 Fibre Geometry (Core Diameter and Fibre Diameter)

Right the way through the fibre fabrication, precautions were taken so that the loss was minimised, particularly reducing the bubble scattering centres within the core glass and reducing the interface loss. However, before the fabrication it was impossible to be sure what the final fibre loss would be or indeed which loss mechanism now dominated. For instance, if extrinsic scattering losses still dominated, the exact loss would depend not only on the number of scattering centres but also fibre core diameter. The scattering loss, in this case, can be shown to be inversely proportional to the core radius squared [2]. Similarly, interface losses will increase with decreasing core size.

Apart from the loss, there were additional uncertainties at the planning stage of what excited-state absorption (ESA) there might be and how efficiently light was coupled to the more lossy higher order transverse modes within the fibre. The important consequence of this uncertainty is that it would be impractical to model the gain taking account of the loss so that fibre geometry, dopant concentration and fibre length could be accurately optimised in advance. (Chapter 7, however, does include a simple model for the fibre gain ignoring the consequences of fibre loss.) Instead the strategy taken was to make a number of fibres that varied the core diameter, selected in such a way to give the best possibility of gain. The range of core diameters chosen for fabrication was from 3μm to 8μm. Additionally, a very large core highly-multimode fibre (30μm diameter core) was fabricated to make ESA measurements and to determine the material loss for the core glass. Table 6.4 summarises the important considerations that are affected by the fibre geometry.

Table 6.4: The Consequences of the Choice for Fibre Geometry

Consideration	***Important Parameters***
Effective Area / Triple Overlap of Pump and Signal beams and the Core	*Core Diameter* / N.A. / λ_p / λ_s
Fibre Loss Dominated by Extrinsic Scattering and Interface Losses	*Core Diameter* and Fabrication Technique
Dopant Concentration	*Core Diameter* and Fibre Loss
Fibre Strength and Manageability	*Fibre Diameter* and Relative Expansion Coefficients of Core and Cladding

6.5 Details of Fibre Fabrication

The method chosen to manufacture the preforms in this project was the rod-in-tube technique because of its simplicity and versatility. Here, a polished rod of the core glass is inserted into a glass tube with a lower refractive index that forms the cladding. The composite is then drawn into a fibre using a specialised fibre drawing tower. If the rod and tube are fed into the furnace at the same speed, the fibre maintains the relative area ratio between the core and cladding. The fibre diameter depends upon the drawing speed, the preform feeding speed and the temperature. The major disadvantage of this method is that imperfections on the inner surface of the tube and outer surface of the rod result in core-cladding interface irregularities, which can cause high scattering losses.

The rest of this section gives the full details of the fibre fabrication.

6.5.1 Melting the LLS Core Glass

The composition of the LLS glass chosen for the core is shown in Table 6.5. The lithium and the calcium starting constituents were in the form of carbonates. All the starting constituents were of high purity (99.99%) so that the extrinsic absorption loss would be low. 1wt% of Sb_2O_3 was included in the composition for two reasons. Firstly, although Cr^{6+} is rarely a problem in Li silicates[5], the presence of the Sb_2O_3 or As_2O_3[4,6] will act to reduce the Cr^{6+} to form Cr^{3+}. Secondly, because the Sb_2O_3 is volatile above 500°C, it will form gas bubbles and help to make the existing bubbles bigger, facilitating their escape[6].

Table 6.5: Core Glass Composition

Starting Component	Mole %
Li_2O	24.1
CaO	12.5
Al_2O_3	0.9
B_2O_3	0.9
SiO_2	61.6

+ 1.0 wt% Sb_2O_3 + 0.07 wt% Cr_2O_3

After carefully weighing out enough starting components for a 100g ingot, the powders were very thoroughly mixed to aid the final glass homogeneity. The glass was melted in 250ml alumina crucibles following the melting scheme shown in Figure 6.4. The oven was an air-atmosphere, molybdenum disilicide element furnace - the same used for the melting of bulk LLS samples of Chapter 4.

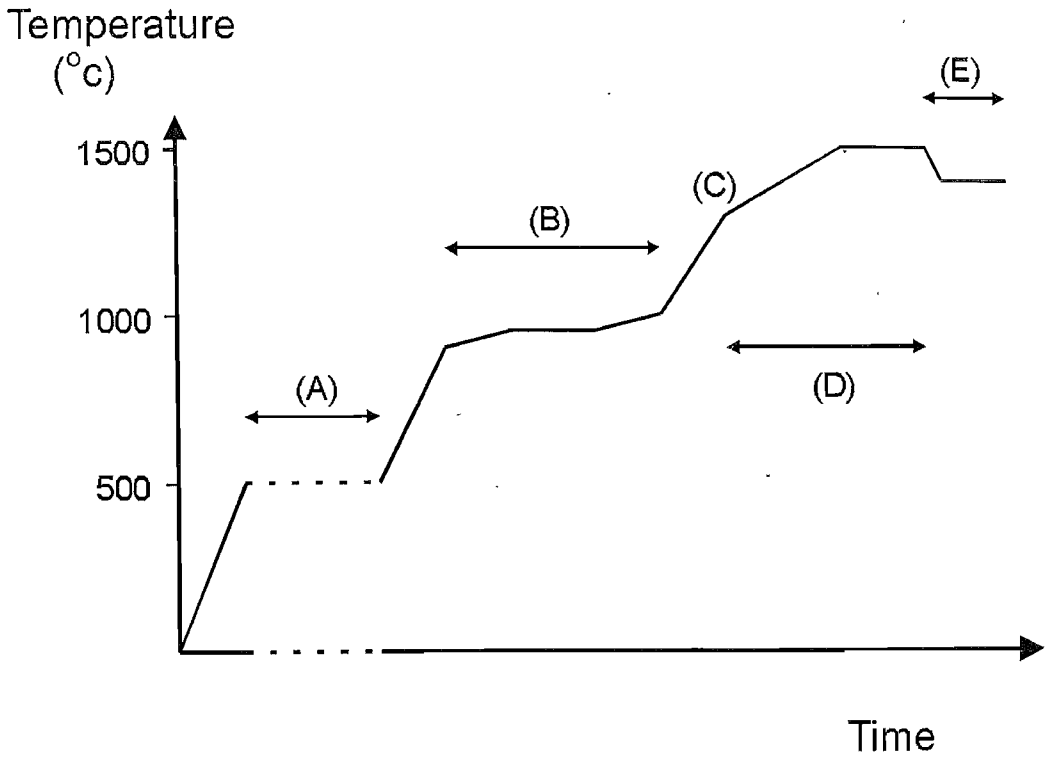

Figure 6.4: Diagramatic Melting Schedule for Bubble Free LLS

Some explanation of the various stages is in order:

(A) The powder was held at 500°C for 10hrs to remove as much of the water as possible. This precautionary measure to remove OH was especially important after the slightly lower than expected QE results for the LLS samples investigated in Chapter 4.

(B) The temperature of the oven was increased very slowly (about 3°C/min) between 900°C and 1000°C, and was held at 930°C for 30 minutes. Decomposition of the carbonates takes place within this temperature range and if this takes place too rapidly, the powder will boil over.

(C) When the melt reached 1300°C, the viscosity was low enough to start stirring with a 5mm diameter silica rod. An electric motor turned a drill chuck, outside the oven, which was holding the rod that extended into the oven. The rod was rotated at about 1 rev/sec. The process of stirring was very important, firstly, to thoroughly mix the melt but also to aid the movement of bubbles to the surface. The stirring helps the small bubbles to coalesce, and big bubbles travel quicker through viscous liquids. Stirring too fast may split up bubbles and therefore be counterproductive.

(D) Whilst still stirring the melt, the oven temperature was increased and then held at 1480°C for 30 minutes. The reason for this stage was that the higher the temperature was raised, the smaller the amount of gas dissolved in the melt. Also the viscosity of the melt would have been at its lowest, giving the gas bubbles a chance to escape. This process is known as fining. Because none of the glass components are volatile below 1800°C and the alumina crucibles are resistant to very high temperatures, it would seem to be advantageous to take the melt above 1500°C. However, the silica starts to react with the Al_2O_3 of the crucible above 1400°C and alumina would have been incorporated into the melt increasing the viscosity.

(E) Stirring was stopped to avoid the absorption of air into the melt during the next stage. The temperature was dropped to 1420°C and held for 20 minutes to ensure that the melt had cooled to the oven temperature. The idea was that at this lower temperature, the gases within the melt would be below the saturation limit, much reducing the chance of gas condensation during casting.

The glass was cast onto a prewarmed stainless steel plate using stainless steel blocks on top as a mould. The mould was shaped into a long cuboid suitable for drilling a rod 10cm long and 10mm diameter. Within seconds of casting, while still red hot, the glass was put in the annealing oven that was already up to temperature.

6.5.2 Annealing

In order that the glass ingot could be drilled without fracture, producing the rod for the preform, it was very important that stresses were removed from the glass by effective annealing. Annealing is actually quite a complicated process with many variables. The most important of these are the top temperature, the time the glass is held at this temperature and the rate of cooling back down in temperature.

Where the removal of internal stresses is the primary concern of the annealing process (rather than control of refractive index), the constant-temperature soaking method of annealing is the most effective[7]. Reference 7 reports the results from investigations on the residual stresses, measured by a birefingence technique, whilst adjusting the annealing variables. Instead of holding the glass above its glass transition temperature followed by a slow constant-rate cooling schedule, the constant-temperature soaking method starts by holding the glass just below T_g for a long period. This phase is followed by a slow cooling rate for a limited temperature range, and then a much faster cooling rate down to room temperature. The reason why this method works well is that there is a considerable amount of strain induced when the sample is held above T_g, since the thermal expansion coefficient shows an abrupt increase above the transition. Below the transition point, however, even if the glass from which the strain has been eliminated by the soaking phase is cooled at a fairly rapid rate, the final amount of strain obtained is small. The reference also highlights that the initial amount of stress is proportional to the thickness of the glass squared. Consequently, it is vital that the ingot for drilling is cast as small as possible.

The DTA result for the final core composition revealed that the glass transition (T_g) was about 495°C (Section 6.3.1). The annealing schedule chosen was to hold the glass at 485°C for eighteen hours, then to ramp it down at 5°C/hour to 370°C and finally cool it faster at 50°C/hour until room temperature.

6.5.3 Creating the Rods and Tubes for the Preform

The rod and tube method of fibre fabrication was chosen for this project. Both the rods of LLS and cladding glass tubes were drilled with an ultrasonic milling machine (Branson) from bulk pieces of glass. This machine was a specially designed drill that used diamond-edged, hollow, tubular drill bits in order to cut cylinders out of the glass.

Some important features of this machine is that it jets water through the drill bit, which is also vibrated with ultra-sound, so that the glass swarf is removed from the active surface.

The LLS was cut into a rod of 8mm in diameter and about 10cm in length ready for the caning process. The glass chosen for the cladding, as explained above, was the commercial glass, Schott LLF2. This glass was cut into a selection of tubes with slightly differing outside and inside diameters to cover the different intended core diameters for the fibres. These tubes were typically about 10cm in length, had an outside diameter of 12mm and an inside diameter of 2mm.

6.5.4 Final Preparation of the Tubes and the Rods

The major disadvantage of the rod and tube method of fibre fabrication is that the poor quality of the interface between the core and the cladding can lead to increased fibre loss. The first stage of the drawing process, caning the core glass rod, will fire polish the core glass giving it a good optical finish. Despite this, there will certainly be transition metals on the surface, remaining from the drilling. For this reason it was decided to chemically etch away the surface of the LLS rod.

After an investigation of many etching schedules, one was chosen as being particularly effective. The etch solution was 5% HF acid and 95% deionised water and was used at room temperature. The LLS cylinder was held at its end by a chuck so that it could be spun along its axis at about 3 rev/sec in order to get a better finish. After one hour of etching, the rod was removed and thoroughly rinsed in deionised water. To ensure the glass was clean, the rod had one hour in "Micro" cleaning solution (International Products Corporation) in an ultrasonic bath followed by another hour in methanol, again in the ultrasonic bath. This whole process was done without breaks immediately before the caning process.

It would have been possible to etch the cladding tubes but it was decided that it would be best to just perform the thorough clean with the "Micro" cleaning solution and the methanol. The reason for this was that there was a strong risk that the acid could not be removed effectively from inside the narrow aperture of the tube, so that the process might well be counterproductive.

6.5.5 Fibre Drawing

The drawing tower had been specially designed for the pulling of soft glasses. It had a highly controllable, stable hot zone produced by radio frequency (RF) heating of a graphite ring. The possibility of crystallisation was minimised by the addition of water cooling above and below the hot zone.

In order to make the large core multimode fibre, a single collapse was sufficient. However, to obtain the dimensions of the small-cored fibre, a double collapse was required (i.e. two claddings, both of LLF2). Note that in the following, a lot of the numerical detail is expressed in arbitrary units that only apply to our drawing tower. All the pulls were done in an argon atmosphere (flow rate – left gauge 7L/min, right gauge 2L/min) with a 43mm long graphite susceptor.

To cane the LLS rod the furnace temperature was 670°C (susceptor temperature = 735°C) and there was very little tension on the bottom of the rod (63g mass). The preform feed was 78rpm corresponding to 0.6mm/min.

The caning temperature of the LLF2 cladding glass was only slightly higher than the caning temperature of LLS, which was not quite ideal for a perfect collapse. In order to ensure a good collapse, the caning was done faster, at a hotter temperature with less control. The temperature of the furnace was 690°C (susceptor temperature = 755°C), a 163g mass was used for the tension and the preform feed was 90rpm corresponding to 0.75mm/min.

The second collapse was the final pull to fibre. The full range of narrow-cored fibre was pulled from a single preform, subtlely adjusting the temperature and drum speed to obtain the different fibre diameters. The temperature required for drawing was 730°C (susceptor temperature = 795°C) with the preform feed at 115rpm corresponding to 0.9mm/min and the drum speed at 190rpm corresponding to 8m/min. A 163g mass was used to tension the initial preform feed. Unfortunately, the fibre snapped during the latter stages of the drawing process with the consequence that the smallest core diameter produced was 5μm. For future trials, smaller cored fibre could be pulled by starting with a larger diameter cladding tube, reducing the risk of the risk of the fibre fracturing during drawing.

Notice that the hottest temperature used during the whole of the drawing process was 730°C which was 45°C below the onset of crystallisation temperature (T_x) for the core glass found from the DTA experiment (see Section 6.3.1). It follows that there should have been no problem with crystallisation within the fibre.

6.6 Fibre Evaluation

6.6.1 Cross-Sectional Images of the Fibres

Figure 6.5 shows a microscope image of a cross-section of the large-core highly-multimode fibre. This single cladding fibre collapsed excellently right the way along its length. Examining many cross-sections, there was no obvious sign of crystals or bubbles. However, there is a noticeable ring, 3μm in thickness, at the core-cladding interface and its origin is not known. This feature has been seen before within our group at the Optoelectronic Research Centre when using Schott LLF 2 as a cladding glass and fibre loss has not been a problem[8]. A cutback experiment investigating the fibre loss is reported in Chapter 7.

Figure 6.6 shows a microscope image of a typical cross-section of the narrow core fibre. It can be seen that the first cladding collapsed well around the core glass but there was a problem with collapse between the two claddings. This cavity extended right the way along the fibre affecting the full range of core diameters. Although the cavity will not affect the numerical aperture or the core modes, cladding modes can propagate without meeting the fibre surface. Consequently cladding modes will be extremely difficult to remove causing significant problems for the fibre experiments in Chapter 7. Unfortunately, this was the only opportunity to draw the narrow core fibre but future attempts of drawing the fibre can avoid this problem of poor collapse by using a higher temperature and drawing speed.

Figure 6.5:
Cross-Sectional Image of the Large-Core Highly-Multimode Fibre

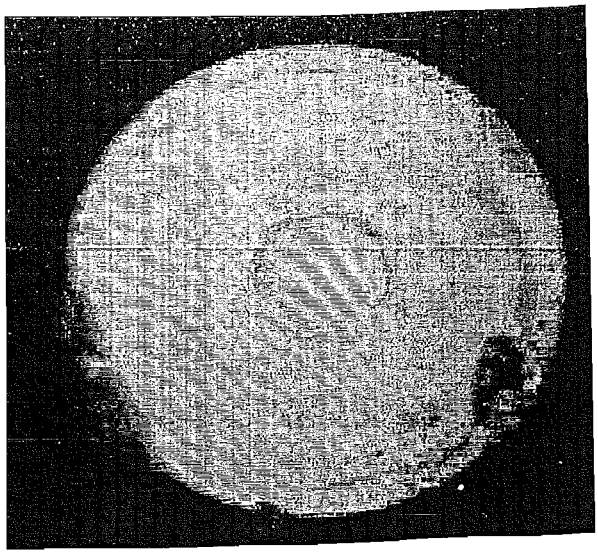

Figure 6.6:
Cross-Sectional Image of the Narrow Core Fibre

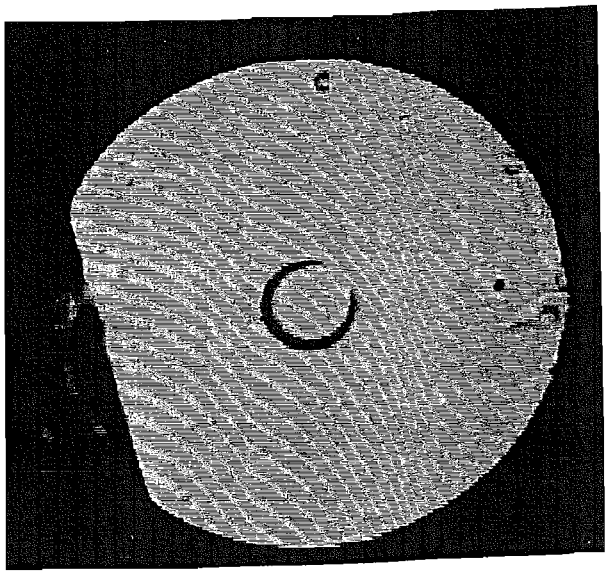

6.6.2 Fibre Strength

For a fibre to be practical, it must be quite strong and resistant to fracture. One of the reasons the Schott LLF 2 glass was chosen for the cladding was that it had a thermal expansion coefficient lower than the LLS core glass (see Table 6.3). The idea is that as the fibre cools after being drawn, the cladding will be under compression hindering the propagation of cracks.

These fibres were very robust. A simple test that attempted to quantify this characteristic was to find the radius of a loop where the fibre fractures. For a 125μm diameter fibre this radius was found to be about 5mm. Any future fibre could be made even stronger if a plastic coating was put over the cladding.

6.7 Summary

A rod-in-tube technique has been developed to fabricate lithium lime silicate fibre. Differential thermal analysis experiments showed that the basic composition of LLS was a very stable glass with T_x at 795°C and T_g at 500°C. Precautions have been taken to reduce the final fibre loss. In particular, modifications were made to the LLS core composition to lower its viscosity, reducing the bubble content within the glass. These modifications could be made in the knowledge that they did not detrimentally affect the quantum efficiency, using the results from Chapter 4. In addition, a glass melting schedule was developed which further aided the removal of bubbles from the glass. It was found that the details of the annealing treatment were critical so that the cast glass was robust enough to drill the LLS cylinders for the preform.

The cladding glass chosen was Schott LLF2, which led to a fibre numerical aperture of 0.26 at 589nm. This commercial glass had a fibre drawing temperature 45°C lower than T_x for the core composition of LLS, reducing the possibility of crystallisation problems. A range of fibre was fabricated with different core diameters to give some flexibility over the fibre experiments of Chapter 7. Unfortunately, there were problems with the final narrow-cored fibre. Firstly, the fibre snapped during the latter stages of the drawing process with the consequence that the smallest core diameter produced was 5μm. Additionally, the outer cladding collapsed poorly onto the inner cladding of the dual clad fibre. Although this feature would not affect the core modes, cladding modes will be extremely difficult to remove during the fibre experiments. However, there was no evidence of problems with bubbles and crystallisation within the fibre and future fibre drawing trials should be able to avoid the difficulties experienced on this occasion.

[1] "Gallium Lanthanum Sulphide Based Glasses for Mid-Infrared Optical Fibres", PhD Thesis by D Brady, University of Southampton, (2000)

[2] "Fluoride Glass Optical Fibres", P W France, Blackie, Chapter 7

[3] Schott Glass Catalogue

[4] "Selene Pro" computer software, BBV Software, Netherlands. (Uses the finite difference method to numerically solve Maxwell's equations)

[5] "Spectral Characteristics and Fluorescence Quantum Efficiencies of Cr(III) in Phosphate and Silicate Glasses with Li and Be Modifiers", A Kisilev and R Reisfeld, Solar Energy, **33**, (2) 163 (1984)

[6] "Spectroscopy and Photokinetics of Chromium (III) in Glass", L J Andrews, A Lempicki and B McCollum, J. Chem. Phys., **74**, (10) 5526 (1981)

[7] "Optical Glass", T S Izumitani, Chapter 3

[8] E. Taylor, ORC, University of Southampton. (Private communication)

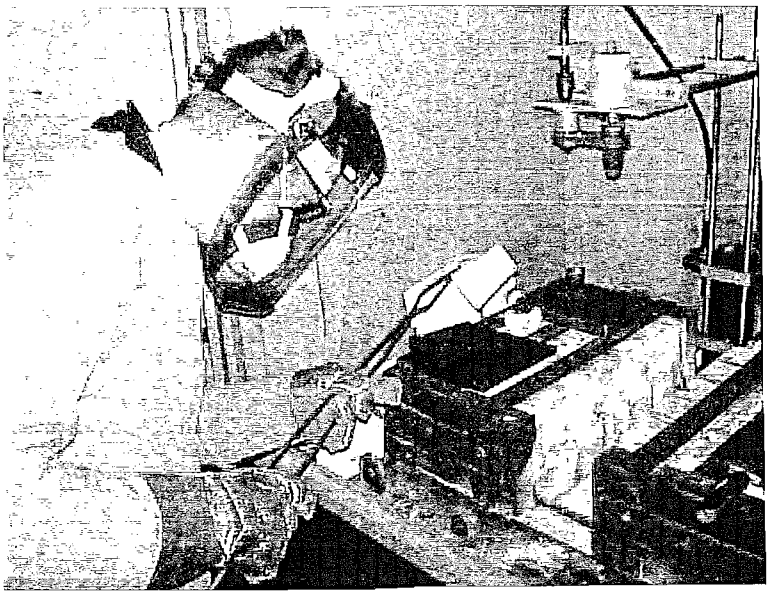

Casting LLS Glass into Stainless Steel Mould

White-Hot Oven at 1400°C

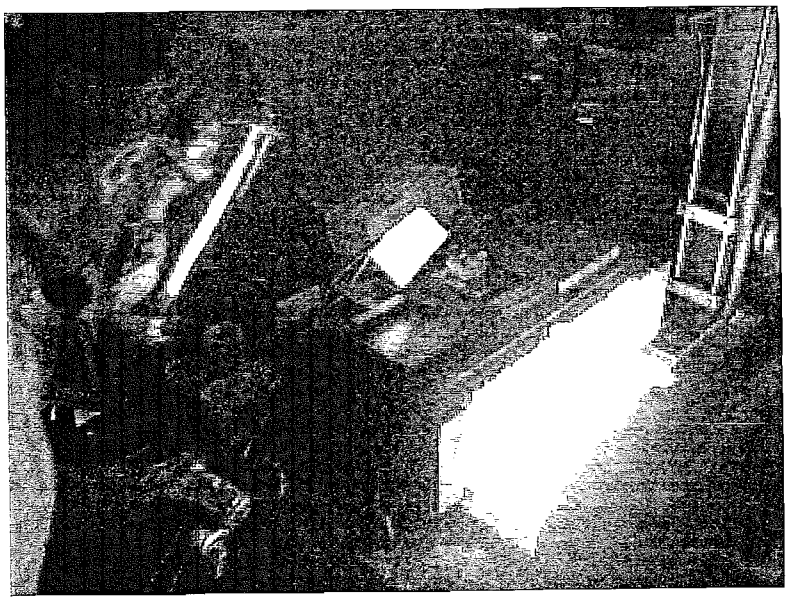

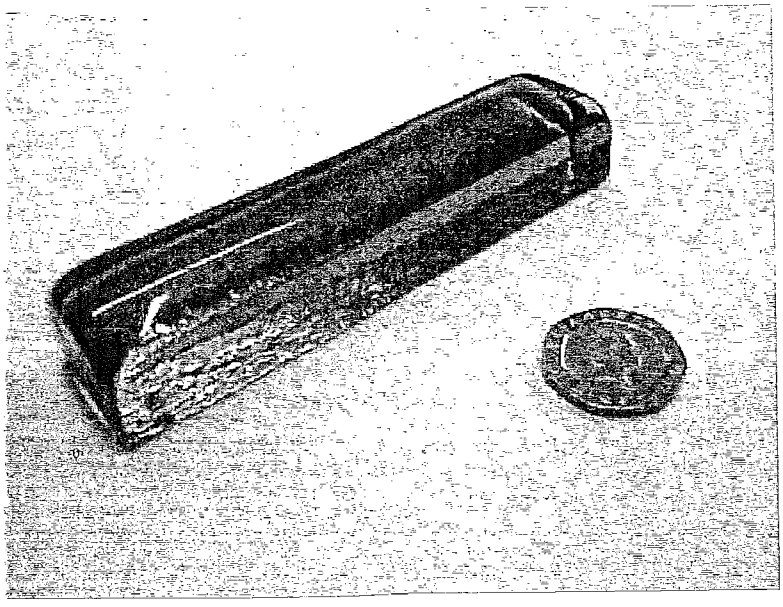

Cr^{3+}:LLS Ingot Ready for Drilling

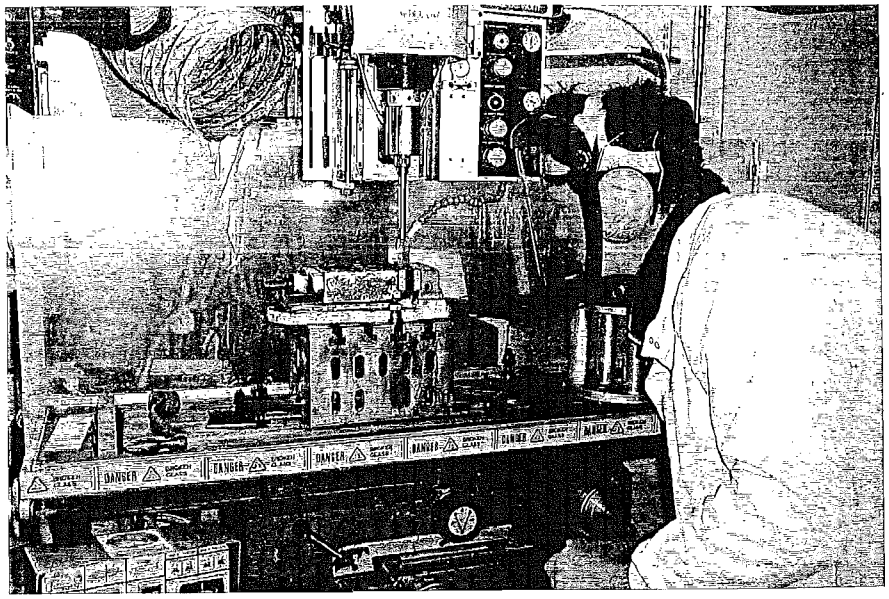

Ultrasonic Drilling of LLS Ingot

LLS Canes for the Preform Rods

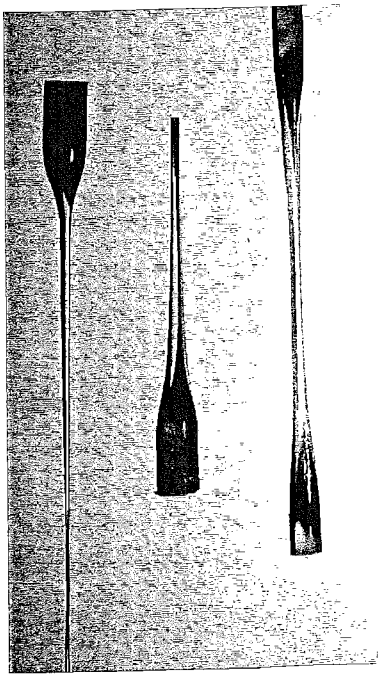

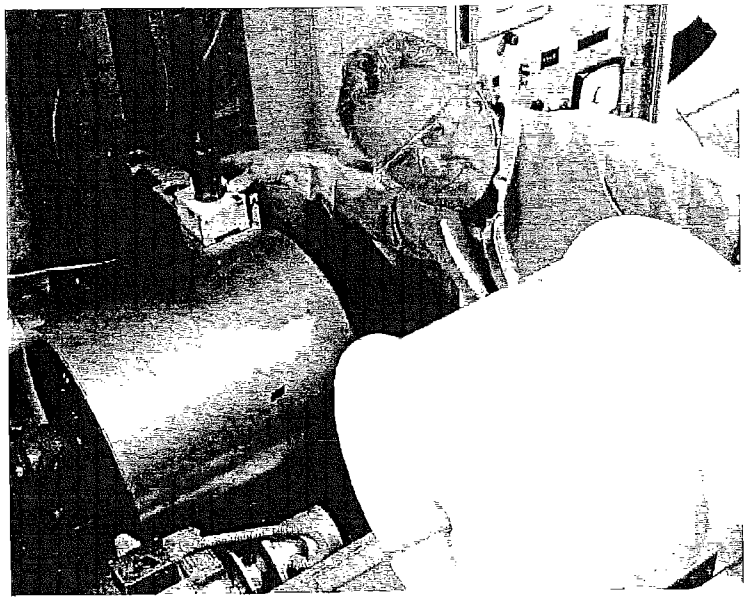

Spooling Fibre onto a Drum

The Gain Investigation

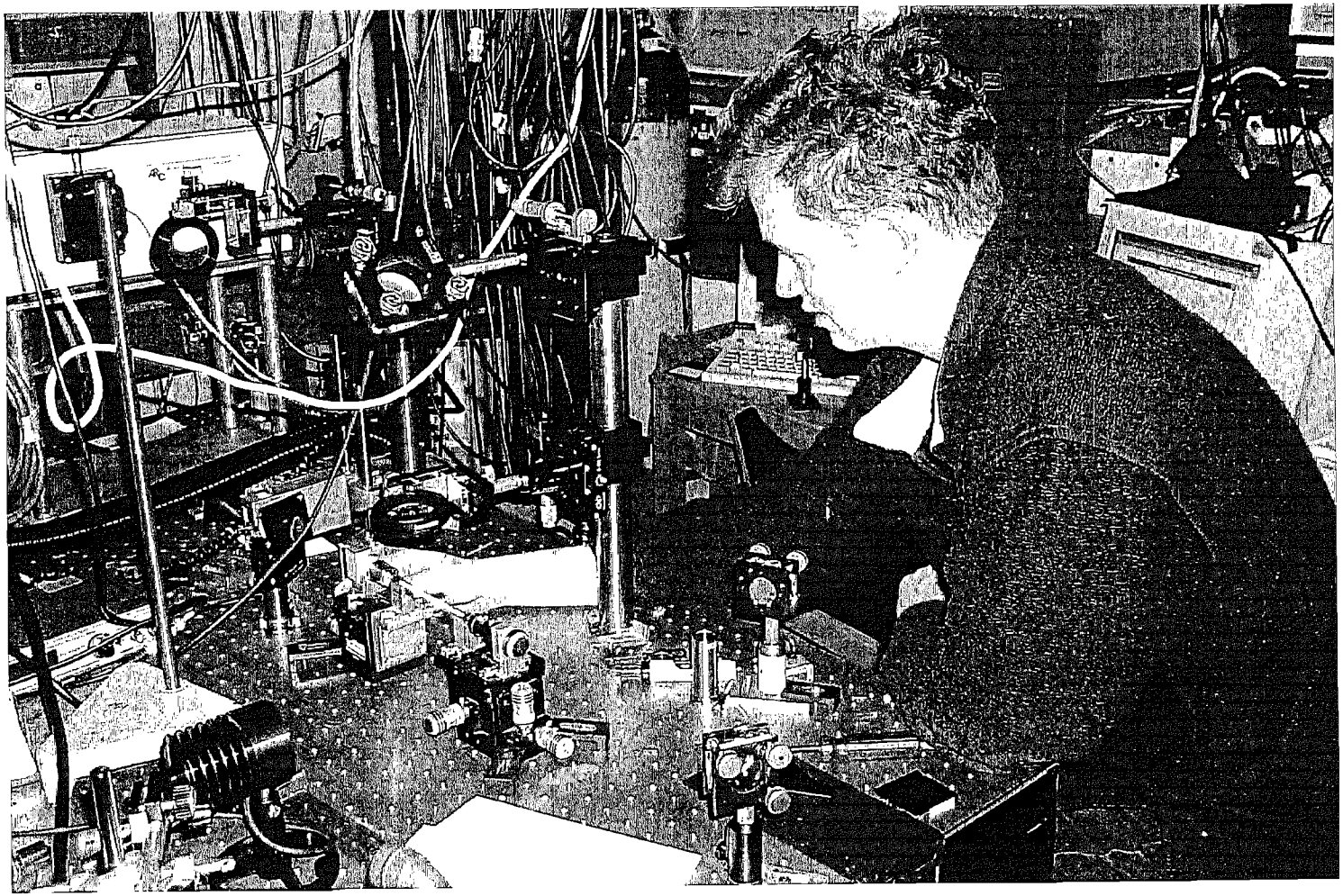

Chapter 7

LLS Fibre Experiments

7.1 Introduction

The major objective of this project was to investigate the feasibility of a Cr^{3+} doped fibre laser. To date there has been no demonstration of optical gain in a transition metal doped glass, with the major obstacle being glass's poor radiative quantum efficiency. Using the geometry of an optical fibre, which can confine the pump and signal beams to a small cross-sectional area, the threshold pump power will be brought down, hopefully to a practicable level.

Chapter 4 explained why the glass lithium lime silicate (LLS) was chosen as an excellent prospect for a Cr^{3+} fibre laser. The chapter investigated a wide range of LLS based compositions and reported the results of spectroscopic investigations. Conclusions were drawn for small improvements in composition that could be made.

Chapter 6 investigated the thermal characteristics of the range of LLS samples. The results for the thermal properties and the spectroscopy were applied to develop a technique of fabricating a LLS fibre. A commercial cladding glass, Schott LLF2, was selected as being compatible with the LLS core glass for fibre drawing, and its refractive index led to the fibre having a numerical aperture of 0.26. The subject of much of Chapter 6 was the development of fabrication techniques minimising the eventual fibre loss. Various fibre core dimensions were fabricated to give some flexibility for the fibre evaluation stage. These fibres were,

- Large core (~30μm) highly-multimode fibre.

  This fibre gave the best geometry for evaluation of material loss and the ESA.

- A selection of narrow core fibres: 5-8μm diameter cores.

  This selection of narrow cored fibres was fabricated with the intention of understanding the nature of fibre loss and cover what were thought the best options for measuring gain. Ideally, some fibre with even smaller cores would have been fabricated but unfortunately the fibre snapped towards the end of the drawing process before the very small cores could be produced.

This chapter reports the experiments investigating these fibres. The experiments included fibre loss, excited state absorption (ESA) and gain investigations. The characteristics of ESA are extremely important to know. Difficult to measure in bulk samples, ESA plays a key role in any transition metal laser's characteristics and may well rule out the possibility of gain altogether despite otherwise promising spectroscopic parameters. To our knowledge this is the first report of an ESA measurement for a transition metal doped glass.

7.2 Fibre Quality

As explained in Chapter 6, both lithium lime silicate and Schott LLF2 are in principle excellent glasses for fibre fabrication. They are very stable and can be drawn in a very controlled and predictable manner. However, on this occasion there were problems with drawing the narrow-cored fibre, which had a double cladding. Here, the outer cladding did not fully collapse around the inner one leaving a cavity in between, which is shown in Figure 6.6. In future drawing trials the problem of a poor collapse can be avoided by drawing at a slightly higher temperature.

The consequence of this inadequate collapse was that strongly guided cladding modes could propagate within the inner cladding with little attenuation. Normally, cladding modes can be removed from a bare fibre by methods such as applying either index-matching liquids or thick black ink to the surface of the fibre. However, in this case it was extremely difficult to remove the cladding modes, as they never met the air-cladding interface. This made all the fibre experiments much more difficult to perform than would otherwise have been the case since it was always difficult to discriminate between light exiting the fibre core and the cladding modes.

7.3 Fibre Loss

The rate at which the pump and signal wavelengths were attenuated along the fibre (acting passively) was a very important parameter to understand. Obviously, it was important that pump light did not get scattered out of the fibre or absorbed by an unwanted impurity before the Cr^{3+} had absorbed it. Similarly, losses for the signal beam were undesirable because the gain must exceed all the losses in order for the fibre to lase.

During fibre fabrication, precautions were taken to reduce the extrinsic losses. By using high purity starting chemicals (particularly low in transition metal impurities) and etching the LLS rod before caning so as to remove the residual transition metal fragments left over from drilling, extrinsic absorption was greatly reduced. Choosing a composition and melting scheme that made bubble-free LLS, and drawing at a temperature well below the onset of crystallisation temperature (T_x), were steps taken to reduce the extrinsic scattering.

Apart from the desire to know the magnitude of the fibre loss, it would also be good to know which loss mechanism was dominating so that further improvements in the fibre fabrication technique could be made in the future. As explained in Section 6.3.1, the extrinsic scattering loss is inversely proportional to the core radius squared. By measuring the loss of the large-cored highly multimode fibre, this should give an idea of the material loss with only a small effect due to the scattering. Measurement of the loss for smaller cored fibres would reveal not only the magnitude of the gain that a laser or amplifier would have to exceed but also the extent to which extrinsic scattering was still a problem.

7.3.1 Cutback Method of Fibre Loss Measurement

In this method a white light source was coupled into a length of the fibre. The principle was to measure the transmitted optical power, $P_B(\lambda)$, as a function of optical wavelength for the fibre of length L_B. Next, the fibre was cut back to a new length, L_A, and the

transmitted power was measured again. The attenuation, A(λ), measured in dB/m may be calculated from the simple relation,

$$A(\lambda) = \frac{10}{L_B - L_A} \log_{10}\left(\frac{P_A(\lambda)}{P_B(\lambda)}\right) \qquad 7.1$$

For this experiment to work well, it was critical that the input conditions remained unchanged. To reduce the error, it was important that the length of fibre removed, (L_B-L_A), was large enough to measure a significant difference in the measured optical powers. Additionally, the cladding modes had to be removed so that they did not influence the result. Applying black ink from a thick felt tip marker to the surface of the first 10cm of the 30μm core fibre did this very effectively. As explained in Section 7.2 it was not possible to remove the cladding modes from the narrow cored fibre. As a result, the attenuation of the light travelling along the LLS core was comparable to the attenuation experienced by the cladding modes over the length of fibre. This made cutback experiments impossible for the narrow cored fibre.

Error in the result may originate from differences in the quality of the output end's cleaves or variation in the fibre loss along the length of the fibre. In order to reduce the significance of these effects, multiple results were taken with many different sections of fibre. In this experiment a spectrum analyser (Ando) was used to detect the transmitted light.

7.3.2 Results and Discussion

Figure 7.1 shows the a typical cutback result for the 30μm core fibre over the wavelengths relevant for the fluorescent signal and away from the strong Cr^{3+} absorption bands. The result was achieved for a cutback of 80cm and it showed the material background loss to be (3.5 +/- 0.3) dB/m. Note the loss increased dramatically as the wavelength decreased showing the tail of the $^4A_2$ to $^4T_2$ transition stretches out a very long way. This reabsorption at signal wavelengths will affect the performance of a device but the effect will not be so strong under saturating conditions.

Figure 7.1: Background Loss for the Large Core Fibre

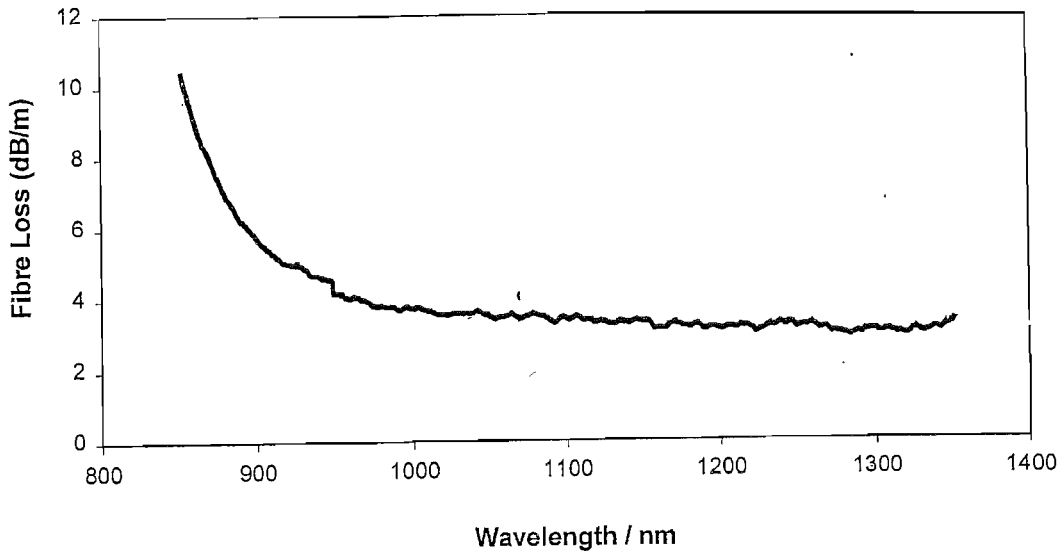

It was unfortunate that loss measurements could not be performed on the narrow cored fibre, as it was this fibre that had the potential for useful devices. Additionally, nothing could be learnt about which loss mechanism now dominated for these important core diameters. What was clear from studying magnified cross-sectional views of the fibre and shining lasers along the fibre, was that there was no problem with crystals along its length and bubble imperfections were very scarce. One thing that was not clear was the effect of the ring around the core-cladding interface (see Section 6.6.1).

7.4 Determination of Excited-State Absorption

The fact that transition metals have such broad optical transitions may be thought of as beneficial for aspects such as wide choice of pump wavelength and the potential broad tunability of a laser. However, there are disadvantages too. Because the cross-section of emission is inversely proportional to bandwidth of the emission spectrum, the threshold pump power required for laser action will be greater. Additionally, there will be an increased probability that there will be absorption for electrons in the excited state, whose energy coincides with the important pump or emission wavelengths.

Excited-state absorption (ESA) can be a major influence in determining the usefulness of a fluorescent material for laser applications. In particular, if strong ESA occurs in the fluorescence region, then the gain may be substantially less than anticipated from the fluorescence measurements. This is because the effective cross-section of emission for

gain is the difference between the emission cross-section and ESA cross-section. In fact, this can be a non-negligible effect even in very successful transition metal lasers, e.g Cr^{3+}:alexandrite[1]. On the other hand, the presence of ESA in the optical pumping region can lead to a reduction in pump efficiency and make it more difficult to populate the upper lasing level.

To accurately assess the possibility of a LLS glass laser and to make the gain model in Section 5.3 more realistic, it was important to measure the strength and location of ESA. To our knowledge no-one has ever reported an ESA investigation for transition metals in a glass. Although it is possible to measure ESA in bulk samples[2], it is technically difficult to do because it requires excellent overlap between pump and probe beams over what is a quite short interaction length. Fibre geometry allows a simpler experiment[3] where the transverse overlap between the guided pump and probe can be very good and the interaction length can be made long.

7.4.1 ESA Experimental Setup

The experimental arrangement allowed pump light and white probe light to copropagate along the fibre under test. Output light passed through a monochromator, after which the light was detected. The general principle of the investigation (shown in Figure 7.2) involved comparing the spectral transmitted power of the probe white light in the presence of the pump light, where there was a controlled population in the excited state, and in the absence of the pump light. The transmission of the pumped fibre differed from the unpumped fibre because the resulting depopulation of the ground state led to bleaching of the ground state absorption (GSA) bands, the population in the excited states leads to ESA and there can also be stimulated emission.

In our version of the experiment, two different pump source / detector setups were required in order to get an ESA spectrum that covered both the blue and red pump bands. To obtain the ESA spectrum between 530-1100nm, an argon ion laser was used as the pump source and a silicon diode was used as the detector. For the ESA spectrum between 400-600nm, a Ti:sapphire laser was used as the pump source and a PMT (S20) was used as the detector (the Si diode was not sensitive enough in the blue). The detected signal was measured by a lock-in amplifier that was triggered by a chopper,

Figure 7.2: Experimental Setup for the ESA Investigation

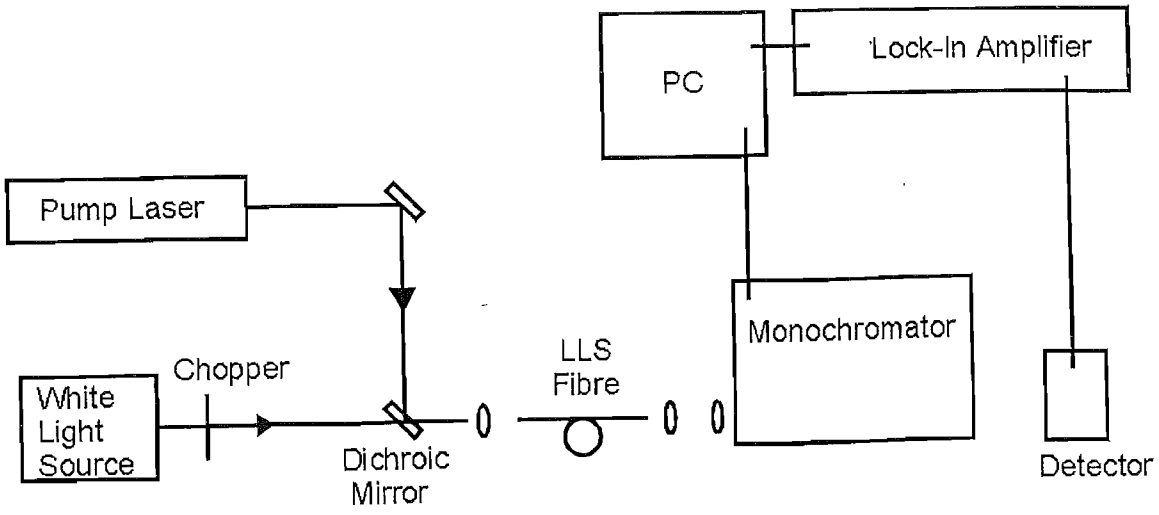

which modulated the white probe light. In each case a different dichroic mirror was required to reflect the different wavelengths of pump light and transmit the appropriate range of the probe light.

A x10 objective was used to focus the two parallel and coincident beams into the section of LLS multimode fibre which had a core diameter of 50μm. The fibre was only 3.5cm long as it was important that there was enough probe light detected at the wavelengths of strongest absorption to obtain acceptable signal to noise. The majority of the power in cladding modes was removed by applying black ink from a thick felt tip marker pen to the outside of the fibre. The short fibre, however, meant that cladding modes were unlikely to be completely attenuated. By conveniently butt-coupling the LLS fibre's output light into a passive multimode fibre also with a 50μm core diameter, the effect of cladding modes was reduced further. The output of this second fibre was collected and focussed into the monochromator by a pair of lenses.

The probe beam was chopped at 120Hz, with the on-period very long compared to the upper state lifetime, so that the populations were in steady state. Filters were placed at the input of the monochromator so that the strong residual pump light could not be scattered through the device and add to the detected background.

A big practical problem with this experiment, which involved lengthy duration of scans, was the elements that led to drift in the pump power that was coupled into the test fibre, changing the upper state population. These elements included instability of pump laser power and drift of the pump beam alignment into the fibre. Similarly, there was the problem of changing the probe beam's coupling into the fibre. This problem could be particularly acute, as the coupling must not have changed when there was laser heating, when the pump was on, and when there was no heating, without the pump. These problems were mitigated by paying close attention to the mechanical stability of all the elements of the optical apparatus and optimising the laser power. One useful technique was to align the pump by chopping it and maximising the detected fluorescence. Then, quickly, the scan involving the pump and the probe was carried out first before the scan for the probe only.

The choice of the pump power was important in order to get good results. If the pump power was not high enough, the effect of the ESA was not clear but if the power was too big, thermal drift became a problem. The pump power selected for both the experimental arrangements was about 1.5W.

In order to extract the ESA spectrum from the results, the following calculation was made,

$$\sigma_{ESA}(\lambda) = \frac{P_{p+w}(\lambda) - P_w(\lambda)}{CP_w(\lambda)} - \sigma_a(\lambda) \qquad 7.2$$

Where $P_{p+w}(\lambda)$ is the transmitted white probe light in the presence of the pump, $P_w(\lambda)$ is the transmitted probe light in the absence of the pump and $\sigma_a(\lambda)$ is the absorption cross-section. The scaling factor of $P_w(\lambda)$ in the denominator has the effect of performing an automatic correction for the spectral response of the apparatus. The value of the parameter C was chosen so that the magnitude of $\sigma_{ESA}(\lambda)$ can be valued in meaningful units. This procedure was based on the somewhat subjective decision as to what appeared to be a reasonable ESA line shape, since an independent means of scaling the ESA spectrum does not seem to exist[4].

7.4.2 Results and Discussion

Figure 7.3 shows the ESA result for the large core LLS fibre. The top curve is the absorption cross-section measured during Chapter 4. The central curve is the data taken for this ESA experiment and is the normalised and scaled change in transmission of the probe light with and without the pump. This curve was scaled by selecting an appropriate constant and corresponds to the value of $\sigma_a + \sigma_e - \sigma_{ESA}$. The final curve is the emission cross-section minus the ESA cross-section and was found simply by subtracting the absorption cross-section from the central curve. There could well be a quite large degree of error due to the problems of the drift and the selection of the constant C and it is not easy to estimate the error's size. The result of the two clear ESA

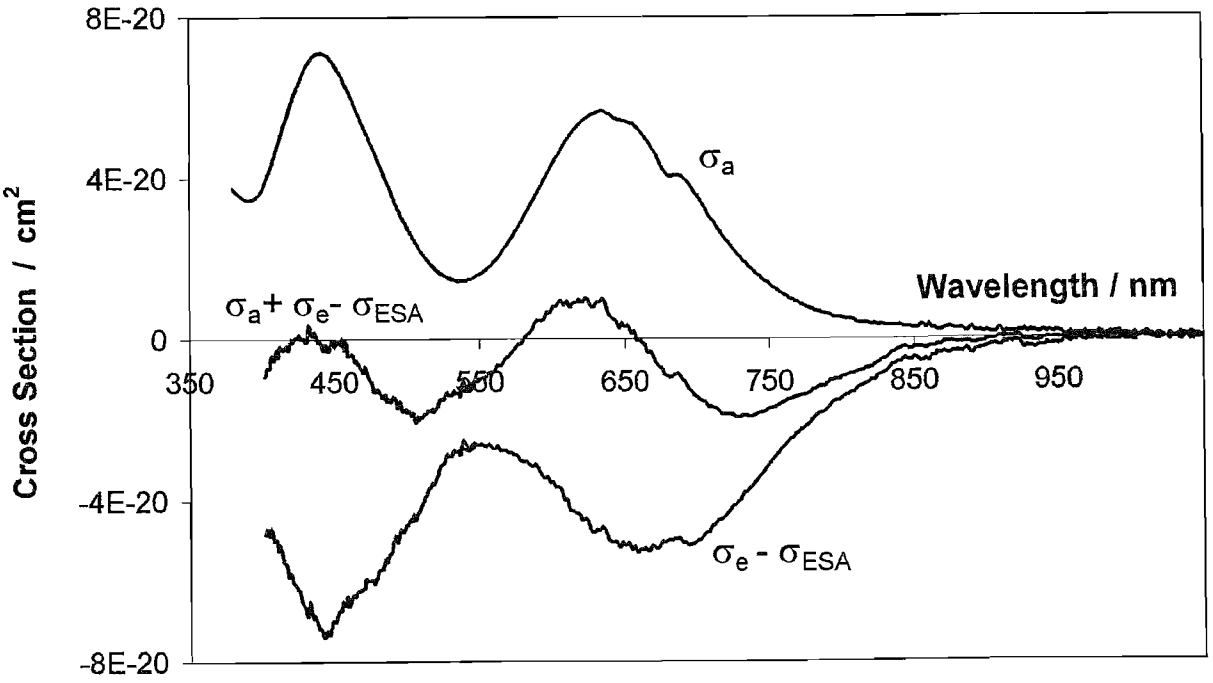

Figure 7.3: Excited-State Absorption in the LLS Fibre

peaks were repeatable and seemed to correspond well with ESA result for a $LaSc_3(BO_3)_4$ crystal[5] which has an almost identical crystal field strength as this LLS glass. However, a reasonable estimate for the error would be 25% of the absolute value.

The results showed that ESA was indeed a significant problem for a gain medium using LLS glass. It can be seen that there were two large absorption transitions from the excited state that have a large degree of overlap with the $^4A_2$ to $^4T_2$ and the $^4A_2$ to $^4T_1$ ground state absorption bands. These ESA bands were attributed to the $^4T_2 \rightarrow {}^4T_1b$ transition (430nm) and $^4T_2 \rightarrow {}^4T_1a$ transition (660nm)[6,7]. One would expect this latter transition to be observed as a narrow line given that $^4T_2$ (t_2^2e) $\rightarrow$ ^4T_1a (t_2^2e) does not involve a configuration change. In fact, this ESA transition was observed as a broad band, due to the influence of the Jahn-Teller effect[5,7,8]. A major consequence of the position of these ESA bands was that the selection of pump wavelength would be critical in order to maximise the population inversion for a given pump power. The central $\sigma_a + \sigma_e - \sigma_{ESA}$ curve in Figure 7.3 revealed that pumping in the region between 600 and 640nm gave the best ratio of GSA / ESA cross-sections. Obviously, the effect of the ESA at the pump wavelengths would become more significant as the excited-state population gets larger.

The most important conclusion to be made was that although the strength of the ESA band $^4T_2 \rightarrow {}^4T_1a$ diminished as it extended into the near infrared, it still dominated the emission cross-section for all the emission wavelengths. If correct this result rules out the possibility of a laser no matter what the fibre geometry or the pump power. However, it would be very easy for the problems of drift in the experiment to lead to a zero offset distorting a result where the emission cross-section was bigger than the ESA cross-section. This is especially true when the ESA strength is so much so greater than the emission, as in this case. In fact this happened in Reference 5 for the $LaSc_3(BO_3)_4$ crystal. Here, the ESA investigation suggested that the ESA cross-section dominated the emission cross-section so that gain would be impossible, and yet the group went on to demonstrate a laser.

If it is possible that gain could still be demonstrated despite the ESA result, it will certainly be the case that the effective emission cross-section will be much reduced from that calculated using the Fuchtbauer-Ladenburg equation. Additionally, the gain profile will be strongly skewed to longer wavelengths due to the action of ESA.

7.5 Gain Investigation

Despite the ESA investigation suggesting that a laser would never be feasible, a gain investigation was still carried out since there was a possibility of experimental error when quantifying the ESA. Like the ESA experiment, the gain investigation was based upon the idea of comparing the transmission of a probe beam through the fibre in the presence and absence of a pump beam. To maximise the size of the gain effect, it was important that the pump and probe were confined within the smallest possible core. Due to the inevitability of cladding modes in the small-cored fibre, this experiment was extremely difficult to perform, particularly ensuring that both pump and probe beams were both well aligned within the core to achieve good overlap.

The experimental arrangement used in the gain investigation is shown in Figure 7.4. It employed a counter propagating scheme for the pump and probe laser beams as this allowed excellent independent control of each beam's alignment. The pump source was a rhodamine 6G dye laser that could be tuned between 580-630nm. The ESA results from Section 7.3.2 demonstrated that pumping between 600 and 640nm would minimise detrimental pump ESA. The pump wavelength selected was 605nm where the dye laser could produce the most optical power and bring about the most fluorescence from the

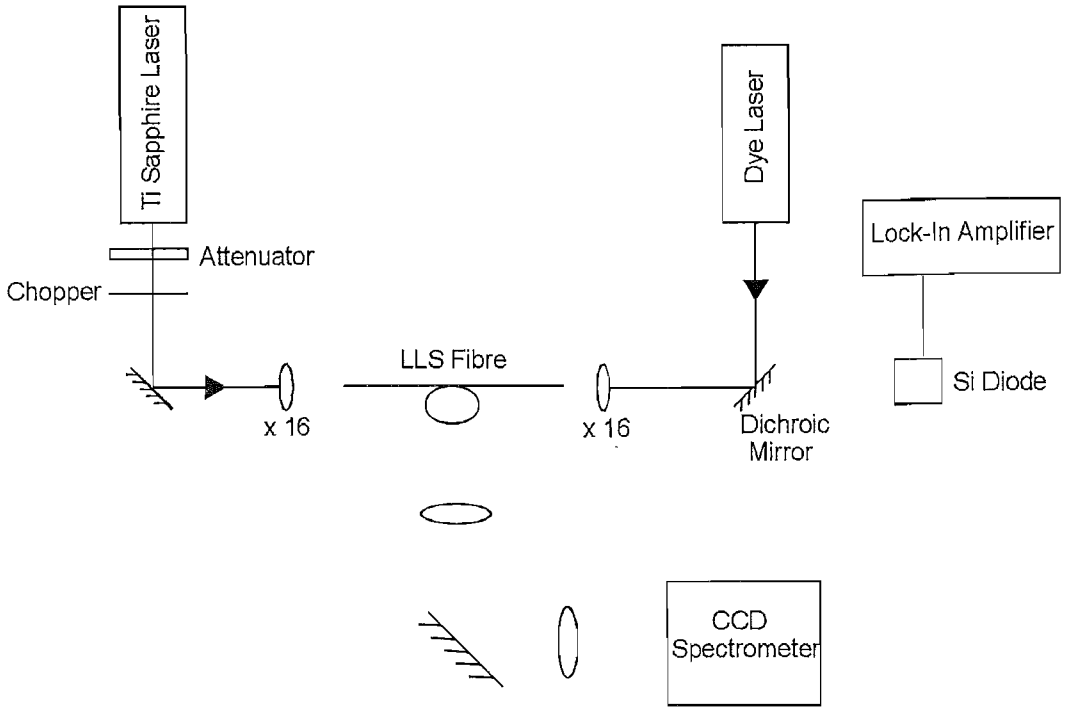

Figure 7.4 : Experimental Setup for the Gain Investigation

fibre. Coupling of the pump beam was controlled by the 16x microscope objective (N.A. 0.32) being moved on a high precision Martock mount whilst monitoring the fibre side fluorescence with the CCD spectrometer. Although the microscope objective's numerical aperture was nominally greater than the fibre's N.A. of 0.26, the dye laser's beam did not completely fill the objective and there would have been a good match of N.A.s.

The probe laser beam was generated by a Ti Sapphire laser with a mirror set that allowed an output between 710 and 850nm. Accurate coupling of this beam was achieved by monitoring the fibre side fluorescence when using 710nm light to excite the Cr^{3+}. The Ti sapphire laser could then be tuned to longer wavelengths where the gain was expected and there could be confidence that the beam position remained unchanged, within the core. During the experiment the probe laser could be tuned to obtain the gain profile.

The chopped probe transmission was detected by a silicon diode and a lock-in amplifier. The diode was positioned on the other side of a dichroic mirror selected so that the 605nm pump would be reflected and the probe light would be transmitted. The movement of the lock-in voltage with time was recorded with a simple chart recorder so that average values could be extracted later. In this experiment, any gain would be apparent as an increase in probe transmission in the presence of the pump light. By dividing this change in transmission, as a function of wavelength, by the probe transmission in the absence of the pump, a figure for the gain could be obtained. This division by the probe transmission automatically corrected for the spectral dependence of the apparatus and additionally any gain measured would be independent of fibre loss.

Figure 7.5 shows the gain experiment result for an 11cm length of 5μm diameter core fibre. The input power of the 605nm pump light was 700mW. By observing the fibre with an infrared viewer, it could be seen from the side fluorescence that this power was saturating the absorption transition. A large fraction of this power would not have been absorbed, either travelling along the fibre as cladding modes or attenuated if the fibre was lossy. Black ink was applied to the outside of the fibre but this would not have

diminished the inner cladding modes. In fact the pump power detected at the end of the fibre was 185mW. The power of the probe beam was 4mW and its wavelength was scanned between 740 and 860nm to obtain the gain profile. It was possible for this result to be repeated for this section of fibre and the effect was extremely sensitive to both the pump and probe beams' accuracy of alignment within the core.

The shape of the gain spectrum above 800nm looked quite plausible, notably the peak position and the way the effect diminished close to 800nm could be considered consistent with a diminishing ESA band overlapping the emission band.The magnitude of the measured effect at its peak was 8%, but this was not taking into account a large unknown offset of probe light power propagating as cladding modes; this meant the actual effect would have been significantly larger. However, the points below 800nm are of great concern, as one would expect a small negative change for the probe power in the presence of the pump due to the ESA. With the overall effect being quite small, these points cast doubt on the legitimacy of attributing the 840nm peak as gain. However, during the experiment it became clear that the two separate peaks, 750nm and 840nm, had quite different origins. Investigating how the size of the effect depended upon the probe pump power highlighted this point. Figure 7.6(a) shows how the size of the effect was independent of the probe power for 840nm probe light. This is consistent with genuine small signal gain. Figure 7.6(b), however, shows that for the 750nm probe

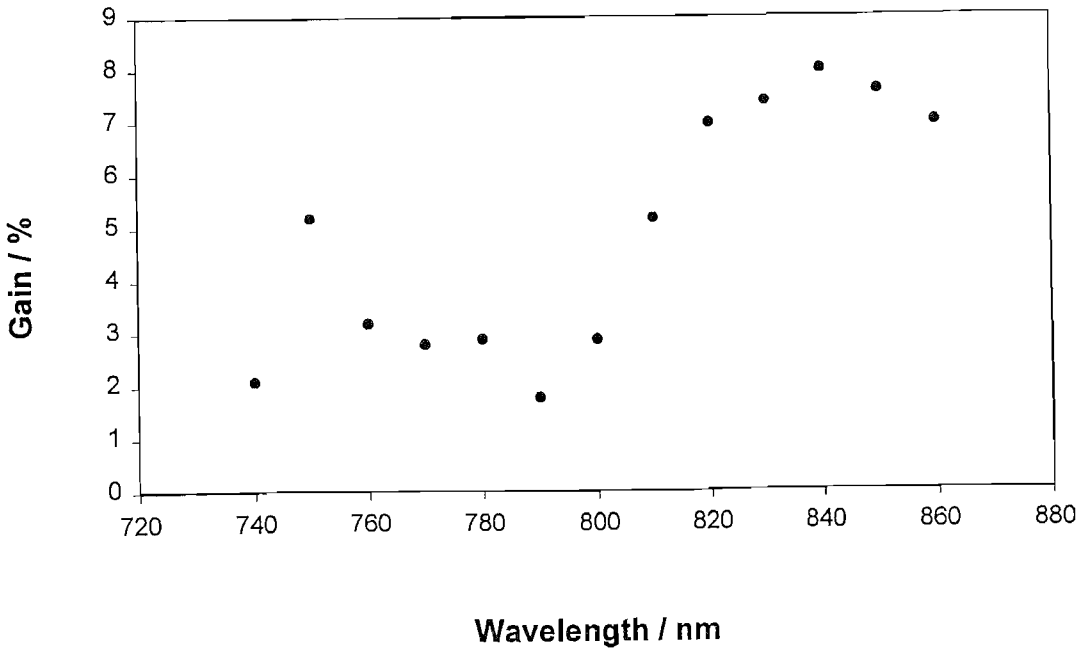

Figure 7.5: Gain Investigation Result for the LLS Fibre

light, the size of this effect increased non-linearly with increasing probe power. This can be interpreted as two separate effects causing the two peaks. It is difficult to think of a mechanism that explains the unexpected peak around 750nm. One possibility was that it was feedback of probe light back into the Ti:sapphire laser.

Figure 7.6(a)

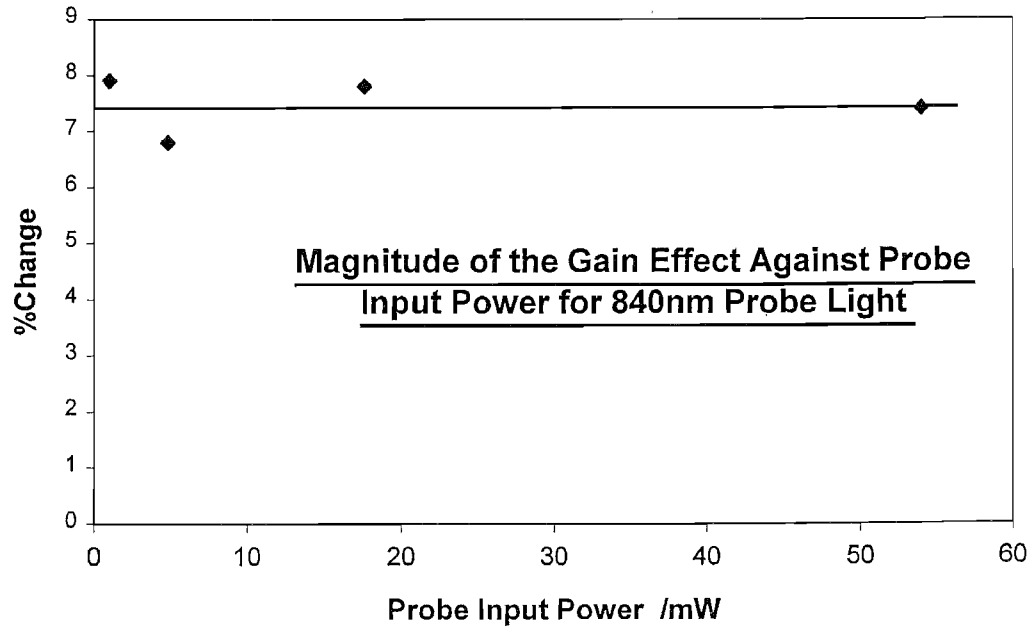

Figure 7.6(b)

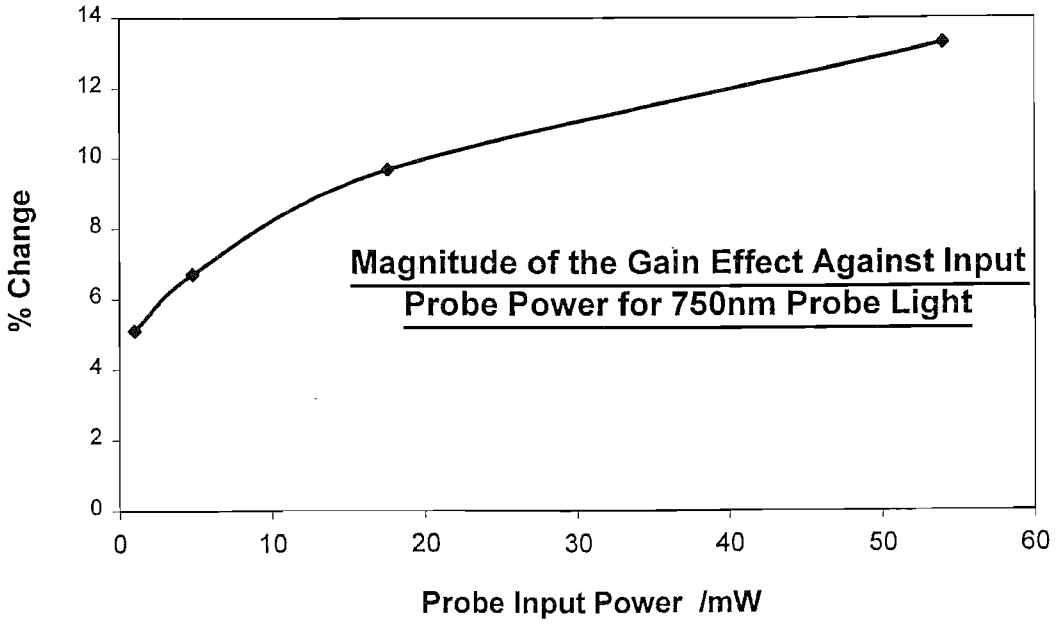

(The lines on these figures are included as a guide to the eye)

If the gain effect was genuine, then by using samples of fibre with substantially smaller cores (had they been available), a clearer gain effect should have been observed, and the experiment would have been significantly improved. Unfortunately, due to the breakage during the fibre drawing process, 5μm was the smallest diameter core available.

7.6 Summary

This chapter investigated the LLS fibre, whose fabrication was reported in Chapter 6. These experiments included a fibre loss measurement, an evaluation of the excited-state absorption and a gain investigation. It was unfortunate, though, that the work was handicapped by the quality of the narrow-cored fibre. The smallest core diameter available was only 5μm, which prevented tighter confinement of the pump and signal beams. Additionally, the cavity between the fibre's double cladding supported cladding modes that could not be attenuated during the experiments.

The material loss for the LLS fibre, found by cutback measurement on a 30μm diameter core fibre section, was found to be 3.5dB/m. The effects of extrinsic scattering and the loss for the narrow-cored fibre could not be evaluated because of the presence of the unwanted cladding modes. However, shining laser light along the fibre revealed that there were no obvious poor sections of fibre with high concentration of scattering centres such as crystals or bubbles.

The large-core highly-multimode fibre was also used for the ESA investigation. We believe this to be the first report of an ESA measurement for a transition metal ion within a glass host. The results showed two broad bands, $^4T_2 \rightarrow {}^4T_1b$ (400-500nm) and $^4T_2 \rightarrow {}^4T_1a$ (600-750nm), which to a large degree overlapped the ground state absorption bands. These results suggested that the best pump wavelength to maximise a population inversion was 600-640nm. Although the strength of the $^4T_2 \rightarrow {}^4T_1a$ ESA band was diminishing as it approached the longer emission wavelengths, the results suggested that the ESA cross-section was greater than the emission cross-section for all the relevant wavelengths. However, the degree to which the effective emission cross-section was reduced by the ESA cross-section was difficult to ascertain accurately, as the signal to noise ratio was poor for this wavelength range and there was a possibility

of a zero offset. In other words, it was difficult to be certain whether ESA completely rules out the possibility of a chromium doped LLS laser. Because of this lack of certainty, a gain investigation was still carried out.

The problems with the fibre quality severely hampered the gain investigation and led to a result that was not clear-cut. A small gain effect was observed peaking at 840nm. The size of the effect was only 8%, but this value would have been diminished by a large unknown offset of the probe light propagating as cladding modes. At the same time, though, there was an unexpected peak at 750nm where no gain should exist. This cast doubt on the legitimacy of attributing the 840nm peak as gain. However, an investigation into the size of the gain effect whilst varying the probe power showed that the two peaks had differing origins, with only the 840nm peak being consistent with genuine small signal gain.

If the cross-section of emission is indeed greater than that of the ESA for any wavelength, the gain model suggests that using a smaller-cored fibre (e.g. 3μm diameter) will lead to a more distinct gain result. If the small-cored fibre loss is not too high, being dominated by extrinsic scattering, a Cr^{3+}:LLS fibre laser might be possible.

---

[1] "Excited State Absorption in the Laser Wavelength Region of Alexandrite", M L Shand and J Walling, IEEE J. Quantum Electronics, **QE18,** 1152 (1982)

[2] "Infrared Excited State Absorption and Stimulated Emission Cross Sections of Er^{3+} Doped Crystals", J Koetke and G Huber, Appl. Phys. B, **61**, 151 (1995)

[3] "Spectral Variations of Excited State Absorption in Nd Doped Fibre Lasers", P R Morkel, M Farries and S Poole, Optics Communications, **67**, (5), 349 (1988)

[4] "Excited State Absorption Spectra of V^{2+} in K $MgF_3$and MgF_2", S Payne, L Chase and G Wilke, Physical Review B, **37**, (2), 998 (1988)

[5] German degree thesis: Simone Hartung, "Cr^{3+} Dotiertes $LaSc_3(BO_3)_4$: Spektroskopie und Lasereigenschaften", University of Hamburg (1994)

[6] "Excited State Absorption of Cr^{3+} in $LiCaAlF_6$: Effects of Asymmetric Distortions and Intensity Selection Rules", H W H Lee, S Payne and L Chase, Physical Review B, **39**, (13), 8907 (1989)

[7] "Excited State Absorption of Cr^{3+} in K_2NaScF_6 and $Gd_3Ga_2(MO_4)_3$, M=Ga, Al", L J Andrews and S Hitelman, J. Chem. Phys., **84**, (10) 5229 (1986)

Chapter 8

Bulk Spectroscopy of Cr^{4+} Doped Chalcogenide Glass

8.1 Introduction

Another strong candidate for a transition metal ion that might be made to lase in a glass host is Cr^{4+}. Since the late 1980's, a number of Cr^{4+} doped crystals have been demonstrated to lase[1]. The first of these, forsterite (Mg_2SiO_4), lased in the near infrared, spanning a range of $1.17 - 1.35\mu m$[2].

Unlike the octahedrally coordinated Cr^{3+} ion, Cr^{4+} sits within a tetrahedral ligand formation that does not have any inversion symmetry. Cr^{4+} has two electrons in its 3d shell and the tetrahedral symmetry leads to the Tanabe-Sugano diagram[1] shown in Figure 8.1. Apart from the effect on the placement of the energy levels, tetrahedral symmetry changes the radiative transition strength. As explained in Section 2.7.1, the lack of inversion symmetry introduces odd parity terms into the crystal field Hamiltonian. It follows that odd parity wavefunctions will be mixed into the d-functions and the electric dipole transitions become stronger, substantially increasing the oscillator strength by at least one order of magnitude[1].

Low radiative quantum efficiency is a major obstacle for getting transition metals to lase within glass hosts By increasing the radiative transition strength due to the T_d coordination, and assuming the non-radiative decay rate remains unchanged, the QE could be increased as shown by Equation 8.1. In other words, Cr^{4+} may well have a larger $\sigma_e\tau$ product than Cr^{3+} within glass hosts and therefore be worth investigating.

$$\sigma_e\tau \propto \eta = \frac{W_r}{W_r + W_{nr}} \qquad 8.1$$

Figure 8.1: Tanabe-Sugano Diagram for $3d^2$ Ions in Tetrahedral Symmetry

(Figure from Reference 1)

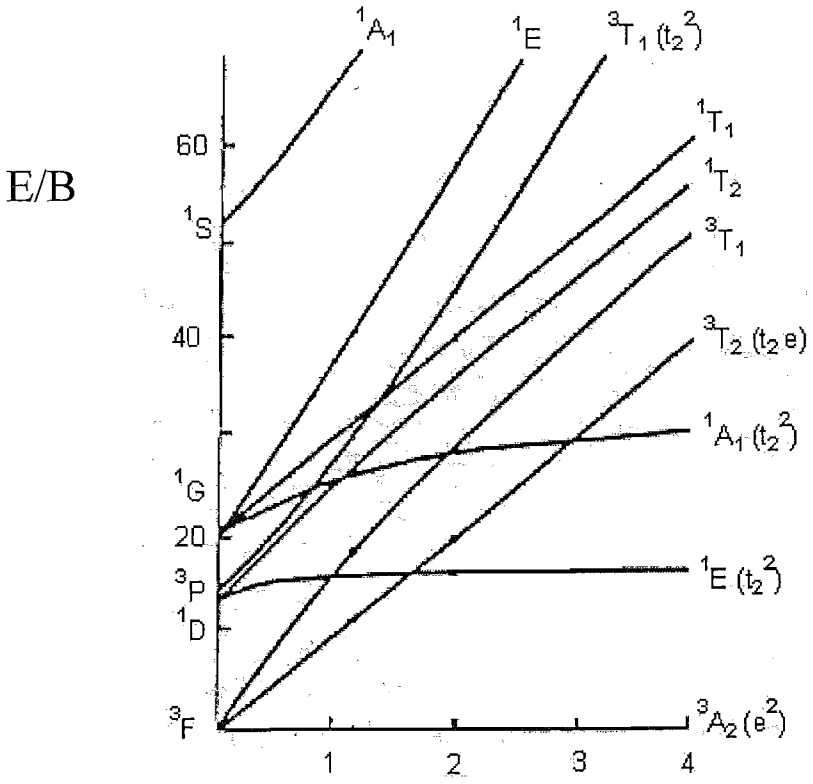

If Cr^{4+} fibre lasers or fibre amplifiers could be developed, they would certainly be very attractive devices. In glasses, although the exact value depends on the host, Cr^{4+} typically emits between 1.2 and 1.6μm and can be pumped between 600nm and 1μm. This makes semiconductor diode lasers a straightforward optical pump source. A tunable Cr^{4+} laser could emit over a very broad range, with the long wavelength extreme being eye-safe beyond 1.5μm. Most attractive of all would be a Cr^{4+} fibre amplifier which covered both the silica telecommunications windows. Such a broad band amplifier would be very attractive for wave division multiplexing either to fit in more channels or to offer gain flattening over a smaller wavelength range.

Apart from applications that rely on emission, Cr^{4+} in crystals has been used as a saturable absorber in the Q-switching of neodymium lasers near 1.06μm[3]. Because glasses may be manufactured in large sizes, with excellent optical quality and at a lower price than most crystals, they may be a very attractive choice for a Cr^{4+} solid-state saturable absorber[11]. Additionally, Cr^{4+} doped fibre could be used as a passive Q-switching element for an all-fibre based Nd fibre laser.

However, fabricating a Cr^{4+} doped fibre is extremely problematic. Firstly, there is a difficulty in obtaining the pure tetravalent state of chromium within glass. In fact there are only three families of glass that have been found to host Cr^{4+} - aluminates, gallates and alumino-silicates, all with a very high content of network modifiers[4]. Unfortunately, none of these glasses is suitable for fibre drawing without the problems of crystallisation. If new glasses could be found that host Cr^{4+} with promising spectroscopy and greater stability suitable for fibre drawing, then the applications outlined above would become a possibility.

This chapter reports the results of a spectroscopic investigation of a range of chromium doped chalcogenide glasses. The investigation included absorption spectra, temperature-dependent emission spectra, room-temperature radiative lifetime measurements and room temperature quantum efficiency. The results reveal that for these glasses, the chromium sits in its tetravalent form. This is significant, since not only is this a completely new family of glass found to host Cr^{4+} but these glasses have the right thermal properties for fibre drawing.

8.2 Cr^{4+} Literature

There is much literature concerning Cr^{4+} doped crystals[1,2,5,6,7], investigating spectroscopy that can be applied to lasers and reporting on laser performance. Reference 1 is a review paper for Cr^{4+} laser materials. The chromium ions in forsterite (Mg_2SiO_4), substituting for the tetrahedrally coordinated Si^{4+} ions, have a radiative lifetime of 2.7μs[1] and emission cross-section of $1.9 \times 10^{-19} cm^2$. YAG is another high performance laser material and the Cr^{4+} has a radiative lifetime of 4μs[1], an emission cross-section of $4 \times 10^{-19} cm^2$ and a radiative quantum efficiency of 11%[7]. These two laser materials were notable for hosting Cr^{3+} simultaneously to the Cr^{4+}.

Comparatively, there has been much less work on Cr^{4+} in glass. This is probably for two reasons. Firstly, it is not that common to find a glass that hosts Cr^{4+}, and secondly, the belief that the weak fluorescence with short radiative lifetimes precludes the possibility of a bulk solid-state laser. The first absorption spectra attributed to Cr^{4+} in glass were reported as long ago as 1968 by Lunkin et al. [8]. The authors performed room temperature absorption measurements and EPR studies on a series of alumino-silicate glasses that were prepared under various melting conditions. They identified a new optical centre in the glass melted under weak oxidising conditions and assigned it to tetravalent chromium.

In the early 1990's the first work on the emission spectroscopy of Cr^{4+} doped glass was carried out. These papers highlighted how unusual it was to find tetravalent chromium in glass and their investigations established glass compositions and melt conditions that could host chromium ions predominantly in the tetravalent state. These families of glass were aluminates[9,10], gallates[5], and alumino-silicates[11], all with extremely high content of network modifiers and melted under weakly oxidising conditions. Reference 11 was written with the overall aim of fabricating a glass saturable absorber for passive Q-switching in the 1μm region. Murata et al.[5] developed a theory as to what controls the valency of the Cr dopant in oxide glasses. It was notable that all of these papers point out that the selection of the atmosphere during melting gave control over the valency of the chromium in the glass. For instance, increasing the oxygen content in a predominantly argon atmosphere[10] led to an increased Cr^{6+} content relative to Cr^{3+}.

8.3 Chalcogenide Glasses

A large family of glasses may be formed from metals such as arsenic and germanium combined with heavier elements in the oxygen family ('the chalcogens') which include sulphur, selenium and tellurium. The vitreous materials derived from such compounds are commonly known as chalcogenide glasses and are notable for their transmission in the infrared. Generally speaking, the electronic absorption edges of chalcogenide glasses lie either in the visible, making the glass red (e.g. As_2S_3), or in the near infrared making the glass black (e.g.AsGeSe). The transmission of a typical bulk chalcogenide specimen may extend to 10-15μm due to the multiphonon edge being at lower energy. The location and steepness of this edge is a complicated function of the effective charges, masses, interatomic bonding forces and sizes of the molecular species which

compose the solid. A simple explanation, however, is that the heavier and more weakly bonded the cations and anions of the glass, the lower the energy of the multiphonon edge.

For a long time the rewards of developing techniques to fabricate chalcogenide optical fibres have been clear. Firstly, because the strength of the intrinsic Rayleigh scattering process is proportional to λ^{-4} and the fact that chalcogenides transmit at these longer infrared wavelengths, chalcogenide glasses were originally identified as a potential material for ultra-low loss fibres for telecommunications. Unfortunately, chalcogenide glasses have never fulfilled their promise as ultra-low loss fibres, since the minimum attainable attenuation[15] is 0.1-10dB/m. Secondly, IR transmitting fibres could be used to conveniently deliver IR light passively to a remote location away from a bulky laser. Examples of applications that would benefit here are flexible laser scalpels or remote gas sensing using IR light. Finally, the low phonon energy of chalcogenides leads to reduced non-radiative decay for rare earth ions[12], making many otherwise infeasible long-wavelength radiative transitions efficient enough for laser action. Chalcogenide fibre lasers, doped with suitable rare earths, make very attractive sources of the infrared wavelengths required for optical sensing of environmentally unfriendly gases. For instance, a particular transition of the Er^{3+} ion may be used to generate 3.8μm light to detect hydrogen sulphide[13].

Despite the development of the erbium doped fibre amplifier for the 1.5μm third telecommunications window there is still a strong need for a 1.3μm fibre amplifier for the second telecommunications window, since much of the World's land based fibre is still at this wavelength. One application that is currently receiving much attention is the use of praseodymium doped chalcogenide glass, with its reduced non-radiative decay, as a host for a 1.3μm fibre amplifier. The most promising glasses in terms of dopant solubility, optical transmission, spectroscopy and thermal properties for fibre drawing are based upon gallium lanthanum sulphide (GLS) and gallium sodium sulphide (GNS)[17].

This chapter reports on how many chalcogenide glasses host the Cr^{4+} ion. The reasons why chalcogenides give rise to advantageous spectroscopy for rare earth ions do not apply to the same extent for transition metals, particularly with respect to the non-

radiative decay mechanisms and active ion solubility. However, all the prior research on the thermal properties of chalcogenides for the purpose of fibre drawing can be usefully applied to this project.

8.4 The Selection of Host Glasses

There is obviously an enormous range of chalcogenide glasses, in terms of both the combinations of atomic species and fractional composition of the constituents. After our initial discovery that GLS hosts Cr^{4+}, it was decided that a wide-ranging survey of chromium doped chalcogenides would be the best way to proceed and find how common this characteristic was. The criteria applied for the selection of host glasses for investigation were, firstly, the glass must transmit at the absorption (600nm - 1μm) and emission (0.8 – 1.6μm) wavelengths for Cr^{4+} - this excluded most selenides and tellurides. Secondly, because the most attractive applications were fibre based, it made good sense to concentrate on glasses that had either been demonstrated to make good fibre already, or had good stability to make successful fibre drawing likely. For the ten selected glasses, the exact composition was chosen to lie well within the glass-forming region, if this was well known.

(1) Arsenic Trisulphide Glass (As_2S_3)

This is one of the most stable chalcogenides and has already been successfully drawn into a fibre. As_2S_3 has a value of (Tx-Tg) = 290°C [18]. The best fibre loss that has been obtained for an arsenic sulphide glass ($As_{40}S_{60}$ at 2μm) was 0.1dB/m [14].

(2) Germanium Gallium Arsenic Sulphide (GeGaAsS)

(Tx-Tg) in this glass can range from 110°C to 300°C depending on the exact composition[15].

(3) Germanium Gallium Barium Sulphide (GeGaBaS)

(Tx-Tg) of certain compositions of this glass can be greater than 150°C[16].

(4) Germanium Sulphur Iodide (GeSI)[16]

The presence of the iodine means this is not a chalcogenide but is instead termed a chalcohalide. This glass can be very stable (T_x-T_g > 150°C) and fibre drawing has been demonstrated with fibre loss of 3dB/m.

(5) Gallium Sodium Sulphide (GNS)

This is another stable chalcogenide glass that has already been successfully drawn. GNS (66:34), the value of (Tx-Tg) = 98°C [17]. The best fibre loss that has been obtained is 1dB/m [18].

(6) Gallium Lanthanum Sulphide Oxide (GLSO)

This is the most stable of the GLS based glasses with (Tx-Tg) =192°C for GLSO (Ga_2S_3 72.5 : La_2O_3 27.5) [18].

(7) Germanium Modified Gallium Lanthanum Sulphide (GLS Ge)

The value of (Tx-Tg) = 129°C [18].

(8) Caesium Chloride Modified Gallium Lanthanum Sulphide (GLS CsCl)

This is another very stable GLS based glass.

(9) Calcium Modified Gallium Lanthanum Sulphide (GLS Ca)

This one of least stable of the GLS based glasses.

(10) Pure Gallium Lanthanum Sulphide (GLS pure)

The value of (Tx-Tg) = 132°C for GLS (Ga_2S_3 70 : La_2S_3 29 : La_2O_3 1).

Most of these glasses have large T_x-T_g, making the glasses stable but it is important to remember that in order to draw a fibre, a temperature must be found where the viscosity is right for pulling within this stable range (see Figure 6.1). This constraint, amongst others, can make drawing these glasses into fibres technically difficult.

8.5 Glass Preparation

All the glasses were melted from powder except the arsenic trisulphide, which was obtained as a high purity commercial glass that was simply remelted with Cr_2S_3 dopant. All the raw materials were high purity (at least 99.99%) and were weighed out in a nitrogen-filled glove box. All the glass samples were 15g in mass.

Glasses 1-4 in the above list were all melted in silica ampoules that had been evacuated to ~10^{-6} Torr and then flame sealed. The purpose of melting inside a sealed chamber is primarily so that the volatile constituents cannot escape. The ampoule was fused onto a silica rod so that it could be held by a chuck situated outside the oven. An electric motor rotated the chuck in alternate directions for 30 second periods. This had the effect of agitating the melt to improve its homogeneity. The powders were heated at a rate of 5°C per minute until the temperature of the lowest melting point of all the constituents was reached. Subsequently, the melt temperature was increased at 1°C per minute, until it reached the top temperature, to avoid a quick build up of large vapour pressures for the sulphur and halide constituents. The glasses were held at the maximum temperature for 20hrs, after which they were quenched in the air. Each glass, still in the ampoule, was annealed at a temperature that was estimated to be T_g from the literature. Finally the glasses were removed from their ampoules and were cut and polished into small cuboids, (5x5x3)mm in dimension.

Glasses 5-10 in the above list were melted following a different procedure. The starting powders were at least 99.99% pure. These glasses were melted within vitreous carbon crucibles in a large silica tube furnace with argon gas flowing through it. The glasses were quenched in an unheated part of the tube with a flowing water jacket. The partial loss of volatile components (~2% weight, mostly gallium sulphide) was tolerated and corrected for by adjusting the batch composition. These glasses were annealed at maximum temperature that that was accurately held just below its T_g for 24hrs before ramping the temperature down. Finally the glass was cut and polished into small cuboids, (5x5x3)mm in dimension.

There was uncertainty over the chromium concentration for all of the glasses. It was extremely difficult to weigh and add about (1.0 +/- 0.1)mg of Cr_2S_3 powder to the batch composition as would have been the accuracy required. The approximate Cr

concentration could be estimated for the samples by comparing the absorption coefficients to the GLS based glasses which had the least uncertainty in the concentration. It was assumed that the absorption cross-section did not vary between the different glasses and this process revealed that the Cr concentration never exceeded 200ppm – low enough for concentration effects not to be a problem.

Table 8.1: Chalcogenide Glass Preparation Details

Glass	Composition (mole %)	Melt Details	Annealing Details	Comments
As_2S_3	As_2S_3 commercial glass (Cr ~ 80ppm)	400°C for 3hrs	300°C for 2hrs ramp 20°C/hr	Glass remelted with Cr dopant
GeGaAsS	GeS_2-80 Ga_2S_3-10 As_2S_3-10	900°C for 20hrs	410°C for 2hrs ramp 20°C/hr	Sample poorly annealed and not polishable.
GeGaBaS	GeS_2-74 Ga_2S_3-16 BaS-10	900°C for 20hrs	470°C for 2hrs ramp 20°C/hr	Polished sample contained almost no Cr
GeSI	GeS_2-50 I-50 (Cr ~ 70ppm)	900°C for 24hrs	320°C for 2 hrs ramp 20°C/hr	
GNS	Ga_2S_3-66 Na_2S-34 (Cr ~ 190ppm)	1150°C for 24hrs	530°C for 24hrs, ramp 1°C/min	
GLSO	Ga_2S_3-72.5 La_2O_3-22.5 (Cr ~ 170ppm)	1150°C for 24hrs	530°C for 24hrs, ramp 1°C/min	
GLS Ge	Ga_2S_3-66.5 GeS-5 La_2S_3-28.5 (Cr ~ 80ppm)	1150°C for 24hrs	530°C for 24hrs, ramp 1°C/min	
GLS CsCl	Ga_2S_3-65 La_2S_3-10 CsCl-25 (Cr ~ 110ppm)	1150°C for 24hrs	530°C for 24hrs, ramp 1°C/min	
GLS Ca	Ga_2S_3-69.7 La_2S_3-28.4 $CaLa_2S_4$-1.9 (Cr ~ 110ppm)	1150°C for 24hrs	530°C for 24hrs, ramp 1°C/min	
GLS pure	Ga_2S_3-70 La_2S_3-29 La_2O_3-1 (Cr ~ 110ppm)	1150°C for 24hrs	530°C for 24hrs, ramp 1°C/min	

Table 8.1 shows the individual details to each glass's preparation, including composition, melt temperature, melt time, annealing maximum temperature, annealing time at the top temperature and annealing cooling rate.

8.6 Results and Discussion

8.6.1 Room Temperature Absorption Spectra

Figure 8.2 shows a selection of the absorption spectra for the chalcogenide glasses investigated. The spectra in this section were all taken with 5nm resolution; higher resolution revealed no extra detail. Unfortunately, values for absorption cross-sections were extremely difficult to estimate because of the large uncertainty over the Cr content for each glass sample. No absorption spectrum could be obtained for the GeGaAsS sample since it was not robust enough to withstand polishing.

All the samples investigated showed a single vibronic absorption band. These broad transitions peaked in the near infrared and were approximately 400nm wide, indicating large electron-lattice coupling. What was notable was that the absorptions of these samples had extremely long tails, often stretching well beyond 1.3μm. For what are otherwise very similar absorption profiles, this prominent characteristic is often used to deduce that the chromium's valency is (IV) rather than (III)[1]. This does indeed mean that all these chalcogenide glasses under investigation host the Cr^{4+} ion – a fact confirmed by the emission experiments. None of the absorption spectra exhibit a clear $^4A_2$ to $^4T_2$ Cr^{3+}-transition and the samples' UV-edges obscure the position of the higher energy Cr^{3+} bands and potential Cr^{6+} transitions. The different glass hosts naturally had different positions for their UV-edge, the values of which are included on Table 8.2. Sometimes this electronic absorption edge extended to wavelengths that were long enough to seriously overlap with the chromium (IV) absorption; the GeSI sample was the clearest example of this.

In previous literature, this absorption has been assigned to two overlapping transitions $^3A_2$ to $^3T_1$ (600-900nm) and $^3A_2$ to $^3T_2$ (900-1200nm) – see the Tanabe-Sugano diagram in Figure 8.1. In other Cr^{4+}doped glasses such as the aluminates[5,10], these transitions lead to discernible structure which is not present in this study. Careful examination of the GNS result (see Figure 8.2), however, showed subtle indications of similar structure this structure for these chalcogenide glasses.

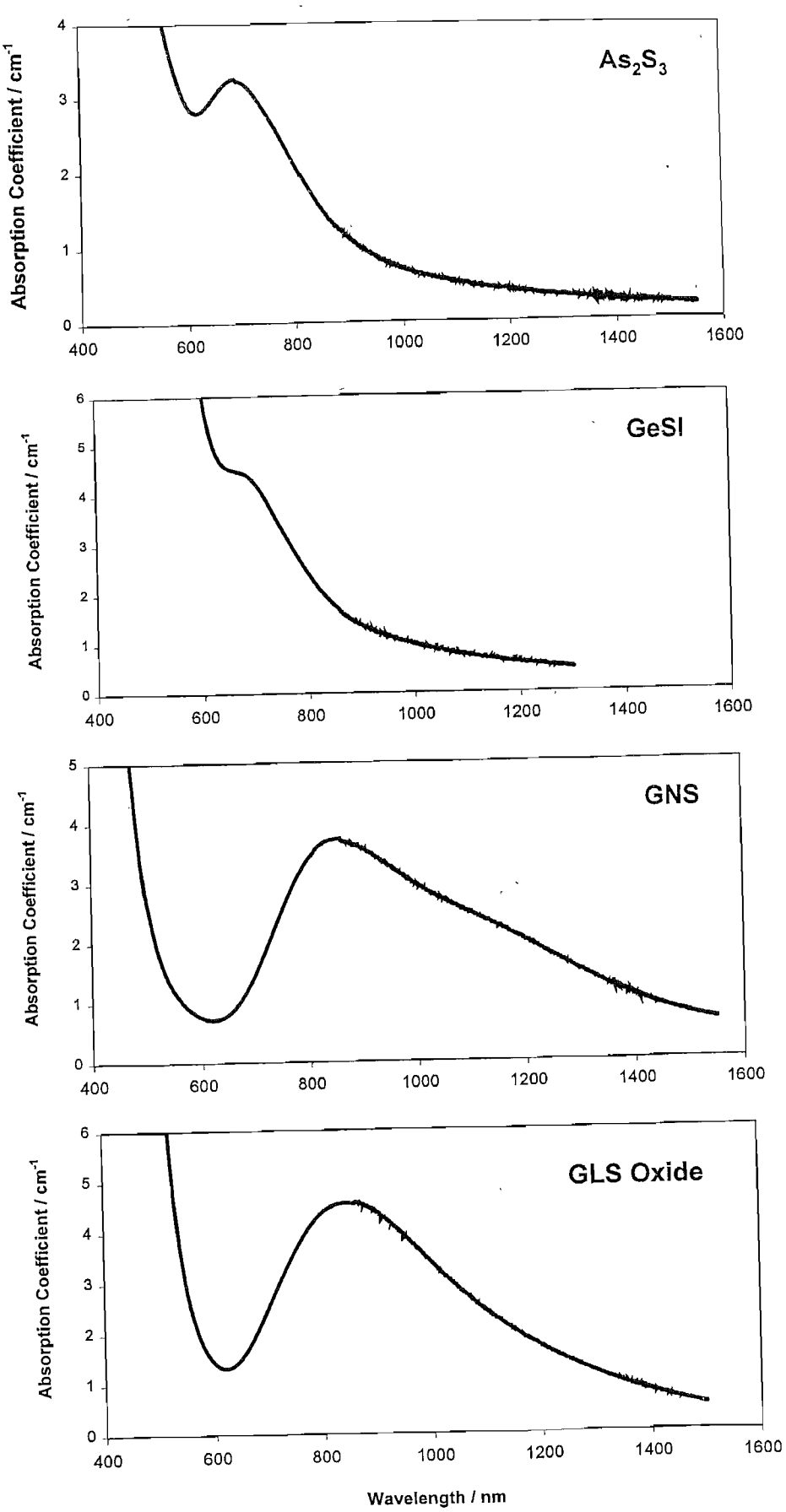

Figure 8.2: Selection of Absorption Spectra of the Chalcogenide Glasses

What was clear, however, was that the position of the Cr^{4+} absorption peaks for all the samples fell into two distinct groups. Firstly, all the GLS based glasses and the GNS had an absorption that peaked at close to 860nm and a tail that stretched beyond 1.4μm. However, the other samples – As_2S_3, GeSI and GeGaBaS – peaked at substantially higher energy around 710nm, which was more in line with previous studies[5,10]. This meant the GLS based glasses experienced a lower crystal field strength, maybe from the differing form of the glass structure or possibly due to two different types of site.

8.6.2 Temperature Dependent Emission Spectra

Emission spectra were taken for all the glass with different sample temperatures. There was no fine detail in the spectra, so the monochromator slits were opened up to maximise the detected signal for the weak fluorescence. The resolution of the monochromator was found to be 20nm and data points were taken every 10nm.

The samples were cooled within a closed cycle He refrigerator and the temperatures investigated ranged between 70K and room temperature. The Ti sapphire pump beam's wavelength was 800nm and had a low input power of 10mW so not to cause laser heating within the sample. The strength of the fluorescence was much weaker at the higher temperatures. The signal to noise ratio was improved by using a longer time constant for each point and increasing the pump power (maximum 40mW). This did not cause significant laser heating of the sample because of the increased heat capacity at the higher temperature.

Because the emission spectra were so broad, they extended beyond the wavelength sensitivity range of the InGaAs detector. For the room temperature experiments, additional spectra were taken using the Si CCD array to obtain data points below 1μm. The spectra were scaled relative to one another and combined to form the complete room temperature spectra. Corrections were made for the spectral response of both these experimental arrangements. Finally, because reabsorption of fluorescence could be a significant problem in these samples, it was important that the pump was aimed at the edge of the sample to minimise distortion of the spectra.

Table 8.2: Detail from the Absorption and Emission Experiments for the Chalcogenide Glasses

Host Glass	710nm Absorption Peak	860nm Absorption Peak	UV-Edge Position (nm)	Emission Peak Position at 70K (μm)	Emission Peak Shift from 70K to Room Temp (nm)
As_2S_3	•		530	1.3	300
GeGaAsS	-	-	-	1.5	100
GeGaBaS	•		580	1.3	300
GeSI	•		600	1.3	300
GNS		•	450	1.5	200
GLSO		•	520	1.4	400
GLS Ge		•	540	1.4	400
GLS CsCl		•	510	1.4	400
GLS Ca		•	580	1.4	400
GLS pure		•	580	1.4	400

Figure 8.3 shows a selection of these emission spectra results, chosen to display the range of features that were observed. Key details of individual results are included on Table 8.2. All the spectra showed a single vibronic band that could be attributed to the $^3T_2$ to $^3A_2$ transition. The fluorescence was extremely broad having a width up to 450nm (FWHM). All the samples at 70K had an emission peak between 1.3μm and 1.5μm. The differences could be attributed to the different crystal field strengths, which tied in well with the peaks in the absorption spectra (see Table 8.2). For instance, As_2S_3 had absorption and emission peak positions with high energy relative to the other samples indicating large crystal field strength. Similarly, the GLS based glasses and GNS had absorption and emission peaks with lower energy indicating a smaller crystal field strength. Additionally, GNS had the largest Stokes shift of about 650nm.

As the sample temperature was increased, the emission peak experienced a remarkable blue shift, perhaps as much a 400nm when the temperature reached room temperature. This may be explained by considering that there was also a dramatic reduction in the strength of fluorescence (approximately a factor of 15 for the GLS based samples). The thermally activated non-radiative decay mechanism described in Section 2.6, which preferentially affects sites with low crystal field strength or large electron-lattice coupling, would lead to such a blue shift. In other words, the remaining emission at room temperature simply resulted from the sites with high Dq and low S that tended to emit at the shorter wavelengths. This remaining fluorescence was a small fraction of the emission that existed at 70K.

To confirm this idea, the short wavelength regions of GLS Ge spectra were closely examined for the two temperature extremes. This experiment was carried out with the experimental arrangement using the CCD array. The experimental details were unaltered for the two spectra so that the strength of fluorescence could be compared. Figure 8.4 shows the spectra for the two temperatures and demonstrates that the room temperature emission was only a subset of the 77K emission. Additionally, it can be seen that there was a narrower zero-phonon transition (810nm) that appeared at low temperature. This characteristic was very similar to the R-line observed in the Cr^{3+} doped glasses from Section 4.6.3. The effect was caused by a population of electrons, existing in the ^1E level, making the optically disallowed transition back into the ground state. The fact that this transition exists indicates that the crystal field strength for this host lies quite close to the $^1E - {}^3T_2$ crossing-point on the Tanabe-Sugano diagram (Figure 8.1). As the sample warmed up, the ^1E level depopulated as the electrons made the phonon-assisted transition over to the lower $^3T_2$ level, and this fluorescence disappeared.

There have been very few papers reporting investigations on Cr^{4+} emission in glass. Aluminates[12] have been shown to emit between 1.1 and 1.7μm at room temperature, peaking at 1.34μm. Despite a similar emission width, and presumably similarly low quantum efficiency, the aluminate glass emits at considerably longer wavelength than the chalcogenides at room temperature. One good explanation for this is that aluminate emission spectrum does not experience such a large blue shift upon increasing

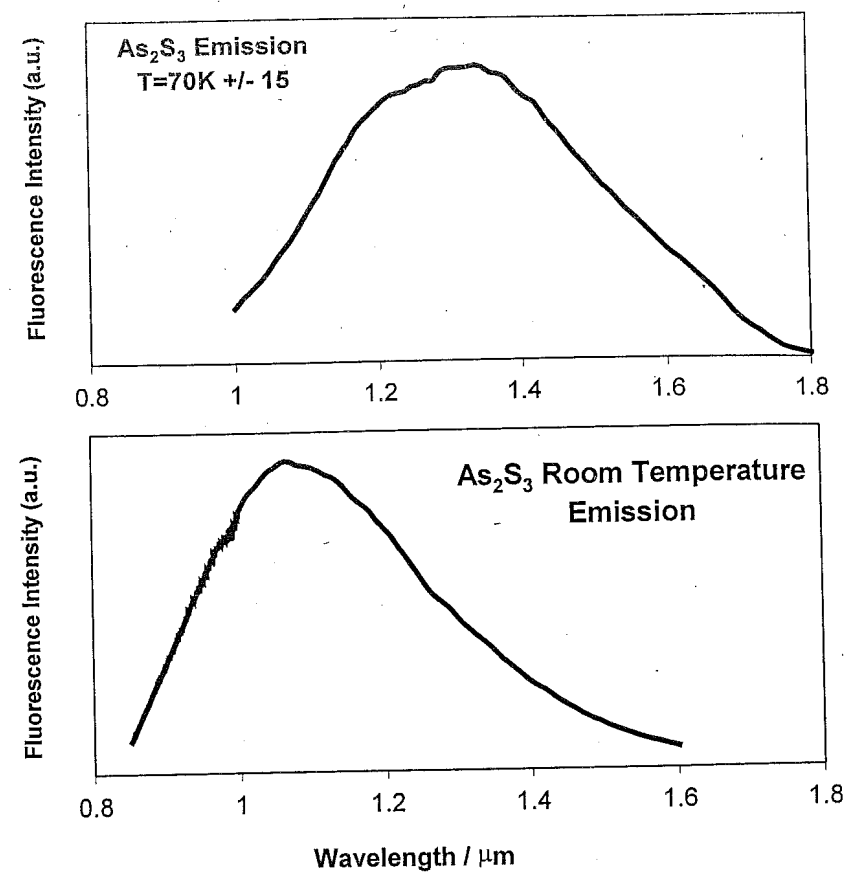

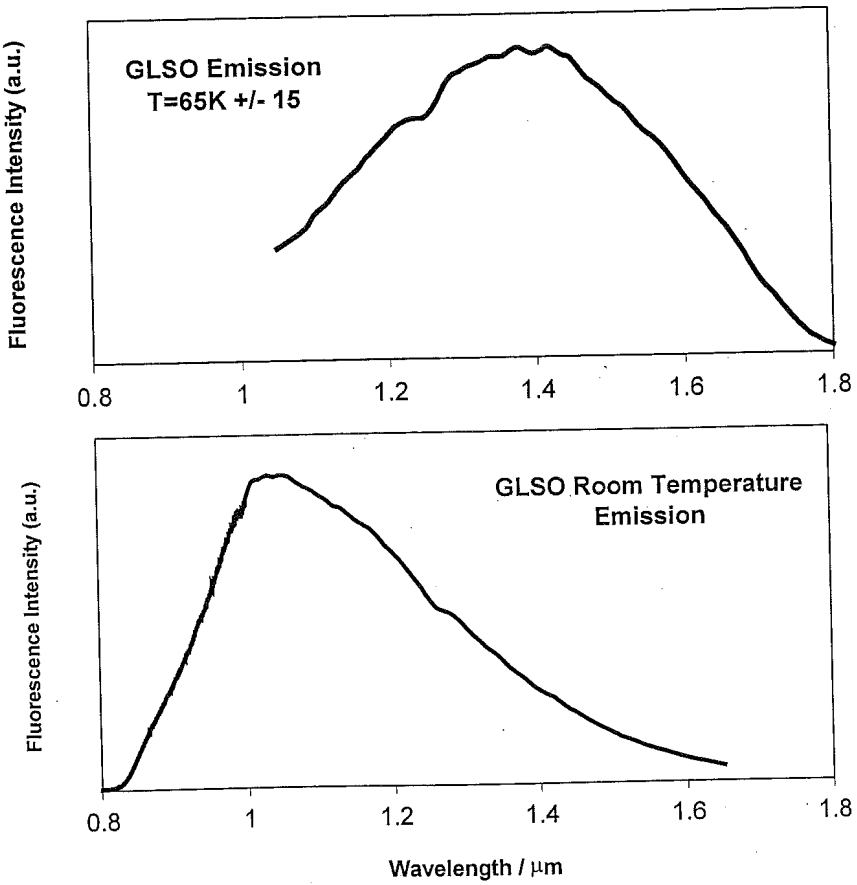

Figure 8.3(a): Low Temperature and Room Temperature Emission Spectra for As_2S_3 and GLS Oxide

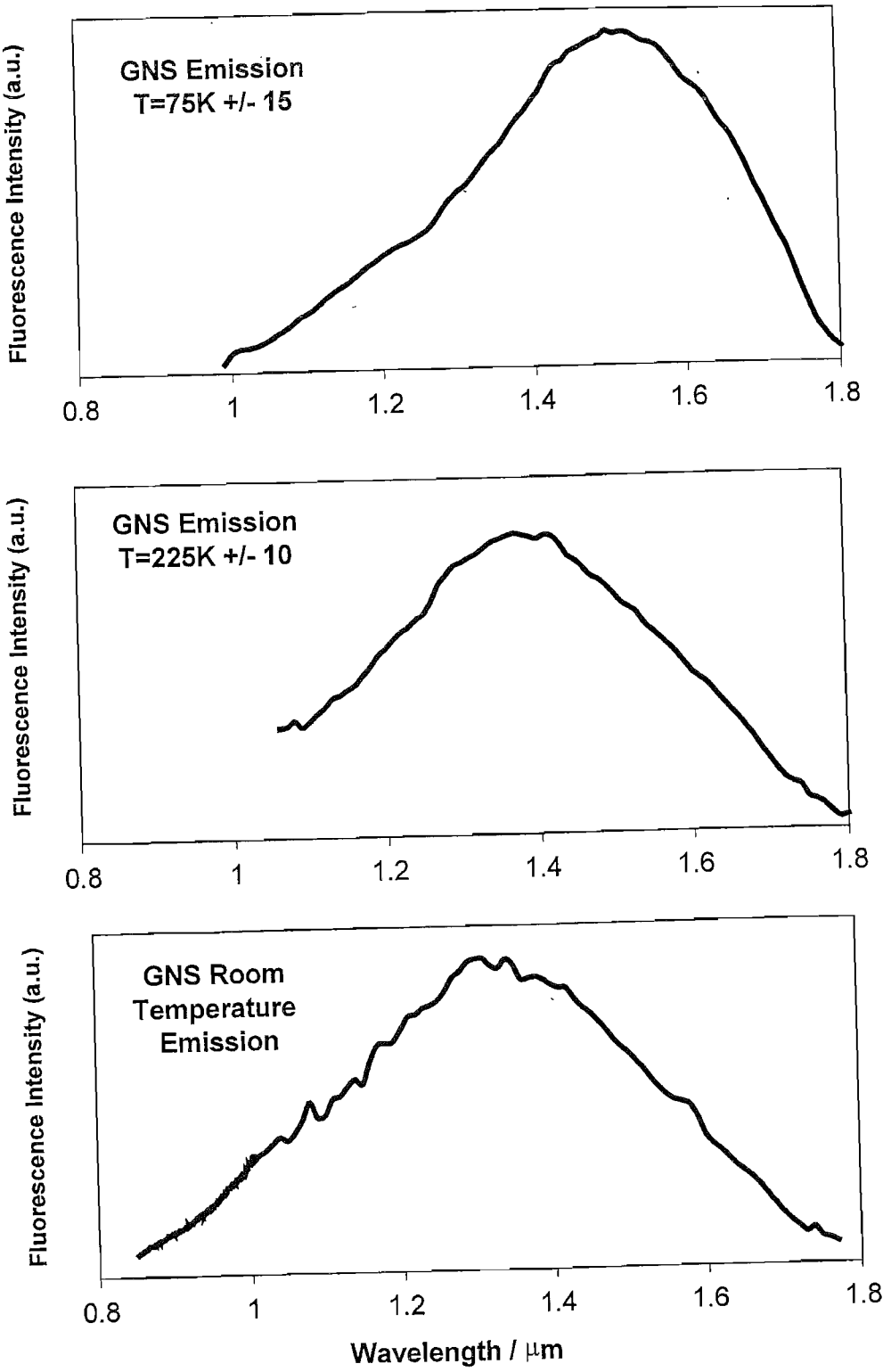

Figure 8.3(b): Low Temperature and Room Temperature Emission Spectra for GNS

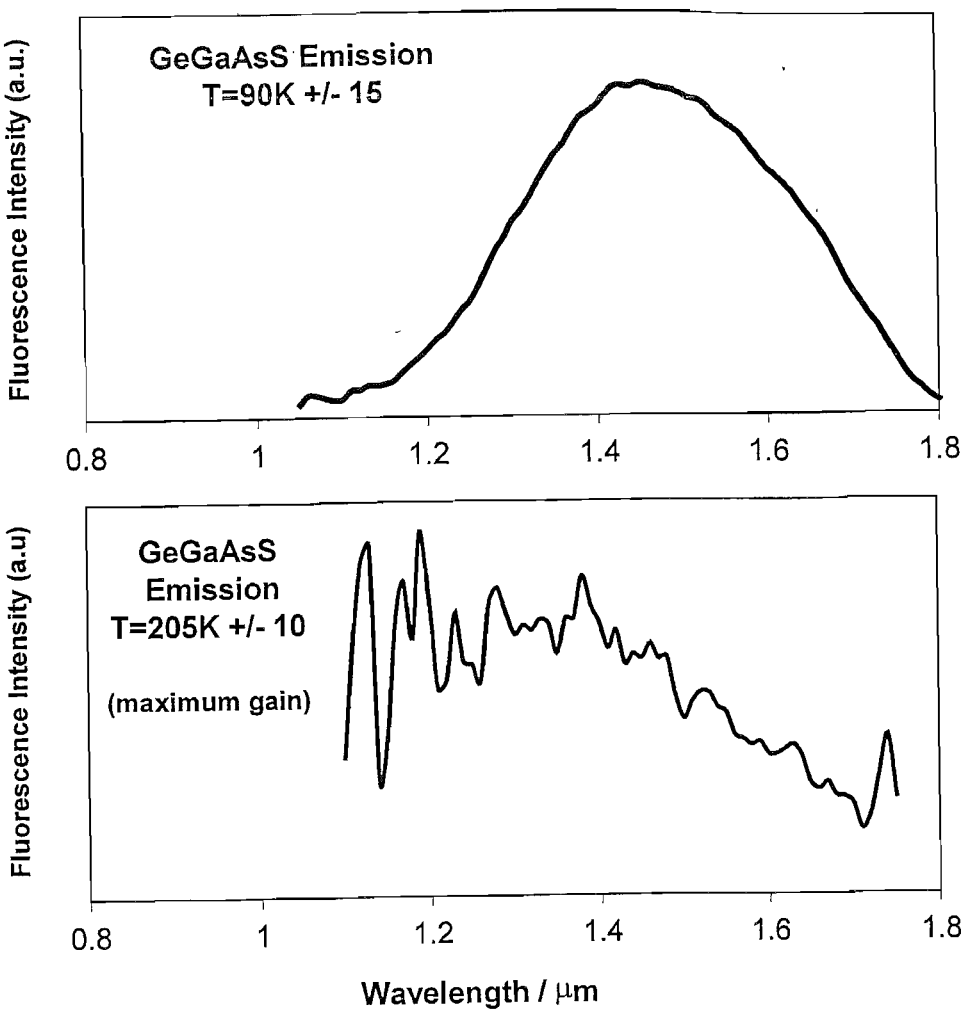

Figure 8.3(c): Low Temperature and Room Temperature Emission Spectra for GeGaAsS

temperature due to a less pronounced site-dependent non-radiative decay rate. This would indicate that there is less variation between sites for the values of crystal field strength and electron-lattice coupling. What is interesting is that the GNS sample, in this investigation, experienced a similarly small blue shift and emitted over a similar wavelength range at room temperature. Having a smaller degree of site to site variation in Dq and S would also explain the discernible $^3A_2$ to $^3T_2$ absorption transition in the GNS absorption spectra in Section 8.6.1.

Crystals[1] tend to emit at this longer wavelength range (typically 1.1-1.7μm) at room temperature, consistent with this idea of little site to site variation in Dq and S. They, too, do not experience such a significant blue shift as in the case of the chalcogenides.

The weakest fluorescence at room temperature was observed in the GNS and the GeGaAsS samples. In fact, there was no detectable emission at all from the latter, which is why a very noisy GeGaAsS emission spectrum for a temperature of 205 K is shown in Figure 8.3(c). Both these samples experienced the least dramatic blue shift with increasing temperature. This dramatic reduction in fluorescence strength was thought to be due to these hosts having the lowest crystal field strength out of the all the samples, the largest electron-lattice coupling in the case of GNS, and therefore possessing the smallest potential barrier for level crossing.

It should be noted that Cr^{3+} emission from 700-900nm was looked for in all the samples but none was ever seen.

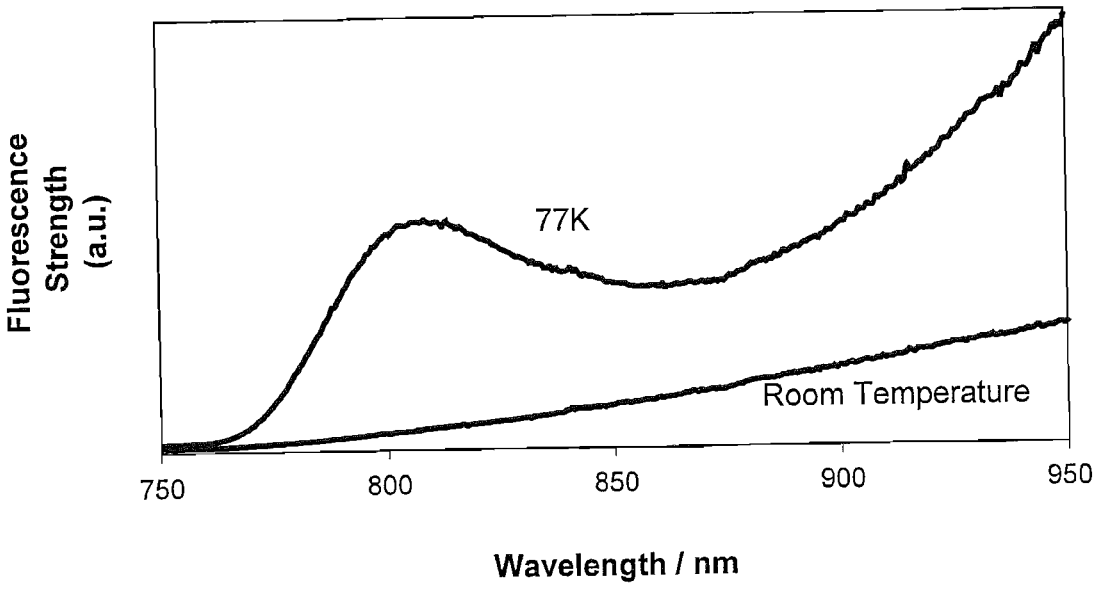

Figure 8.4: Short Wavelength End of Emission Spectrum for GLS Ge at 77K and Room Temperature

8.6.3 Room Temperature Radiative Quantum Efficiency

The room temperature quantum efficiency was investigated for all the samples using the integrating sphere technique described in detail in Chapter 3. The technique gave a constant geometry for the collection of fluorescence and the setup was calibrated with a sample of known QE. In order to have confidence in the results, a number of important corrections needed to be made.

The pump wavelength used in this investigation was 750nm and the reference sample was Cr^{4+}:YAG which was known to have a QE of 11% [7]. Although there was uncertainty over the exact dopant concentration for the samples, the value was low (~ 200ppm). Consequently, the possibility of ion-ion interactions could be ignored. The samples had been polished on six sides of 5x5x3mm cuboid. All the glasses were investigated except GeGaBaS for which there was no suitable polished sample.

There were many reasons to why the error in this Cr^{4+} QE investigation is greater than that for the Cr^{3+} experiments from Section 4.6.6. Firstly, because the reference YAG sample was optically thin (absorbed 10% of incident power), there would have been a relatively large uncertainty over the absorbed power due to error in the estimated reflected fraction of incident power. It was reckoned that this problem could lead to a potential systematic error of 30% of the QE value. Additionally, owing to there being no appropriate wavelength that was unaffected by the UV-edge or the Cr^{4+} absorption, it was very difficult to estimate the scattered fraction of incident power without having similar blank samples. The doped samples were good quality with no major scattering centres and so the small effects of scattered power were neglected.

Another large source of error, however, was due to the problem of reabsorption of fluorescence. Compared to the Cr^{3+} QE investigation, the effect of reabsorption was thought to be a much more significant effect. This was because the samples were optically thicker (typically 75% of incident power absorbed), and there was much greater overlap between the absorption and emission bands. As a reasonable estimate of the reabsorbed fraction for each sample, the absorption coefficients for the relevant wavelengths were calculated from the absorption results and it was assumed that the average emitted photon would have to travel 2mm to reach the surface of the sample. Multiple scatterings, re-emission, and fluorescence re-entering the sample from light

travelling inside the integrating sphere were all assumed to be improbable. The reabsorbed fraction for these samples was estimated to range between 10% for As_2S_3 to 60% for GLS pure. It was reckoned that the uncertainty in this correction could lead to a potential error of up to 20% of the final QE values.

Glass Host	Quantum Efficiency (%) (+/- 50% of absolute value)	Room Temperature Lifetime (μs) (+/- 0.1)	Stretch Factor
As_2S_3	2.4 (3.4)	0.7	0.56
GeGaAsS	~ 0	-	-
GeGaBaS	-	0.7	0.55
GeSI	0.8 (2.5)	0.5	0.53
GNS	< 0.05	-	-
GLSO	1.7	1.7	0.64
GLS Ge	1.7	1.3	0.68
GLS CsCl	1.3	1.7	0.67
GLS Ca	1.8	1.1	0.65
GLS pure	1.5	0.9	0.60

Table 8.3: Room Temperature Quantum Efficiency and Lifetime Results

The QE results are displayed along with the room temperature lifetimes in Table 8.3. As expected, all the samples were subject to considerable non-radiative decay and the values of the quantum efficiency were low. This is further evidence that having a low phonon energy glass host is not the key consideration for good radiative quantum efficiency for transition metals. The strongest fluorescence came from the As_2S_3 glass that had a QE of over 2% and this is likely to be an underestimate. Because of the 750nm pump light and the position of the UV-edge for the As_2S_3 and GeSI samples, the

absorbed power will have been overestimated. The estimate for absorbed power was adjusted for the effect of the band-edge, giving As_2S_3 a corrected QE value of 3.4% and GeSI 2.5%. By selecting a longer pump wavelength, the measured QE would improve dramatically but there will always some unwanted absorption due to effect of the UV-edge, especially for GeSI. Interestingly, these glasses had the highest crystal field strength (the peaks of absorption had the highest energy), leading to a large potential barrier for non-radiative decay by level crossing.

The GLS based glasses had QE values between one and two percent. Easily the worst samples for strength of fluorescence were GNS and GeGaAsS. In fact, the latter had no detectable room temperature luminescence. Again what is interesting is that these glasses had the lowest crystal field strength and large electron-lattice coupling (see Table 8.2), leading to a small potential barrier for non-radiative decay for level crossing.

To our knowledge, this is the first investigation of QE in Cr^{4+} doped glass and so no comparisons can be made to these results.

8.6.4 Room Temperature Lifetimes

From Section 8.6.2, it can be seen that for most samples the broad fluorescence peaked at 1μm, at the edge of Si and InGaAs detection. Measurement of fast decays with weak fluorescence above 900nm using the insensitive InGaAs diode would have been very difficult. Instead, a photomultiplier tube (Hamamatsu R3236 with S1 photocathode, sensitive up to 1.1μm) was used to measure the decays for the high-energy portion of the fluorescence profile. Like the Cr^{3+} results (see Section 4.6.4), it was expected that emission with longer wavelengths will have shorter lifetimes due to the site dependent non-radiative decay rate. The 800nm pump light was 10mW in power and an 850nm long pass filter prevented this pump light from being detected. The decays were found to fit best with stretched exponentials. The error in the lifetime results should be small because PMTs have fast time response (10ns), the pump turnoff was short (90ns) compared to the lifetime, and the fits were good. A reasonable estimate of the error is 0.1μs.

Table 8.3 displays the room temperature lifetimes with its stretch factor for the stretched exponential fit along with the QE results. There are no results for the GNS and GeGaAsS because there was not sufficient fluorescence to obtain decay profiles with an acceptable signal to noise ratio.

All the samples had room temperature lifetimes of around 1μs, and the decays were highly non-exponential. These values can be compared to a 0.65μs lifetime at the peak of emission or aluminate glass[10]. It must be remembered, though, that the lifetimes in this investigation were distorted to higher values owing to only the detected short wavelengths contributing to the measurement. In crystals[1], Cr^{4+} has a great range (0.1 - 5μs) of room temperature lifetimes depending upon the host. Forsterite has a lifetime of 2.7μs and YAG 4μs[1].

8.7 A Note on the Cr^{4+} Site

Given how unusual it is for a glass to host Cr^{4+}, it is worth considering where the chromium ion may be situated within the glass structure. In glass, the valency and position of a dopant ion depend on two major factors. Firstly, the wavefunction lobes for the ion must be directed so as to have the lowest energy. Changing the ion's valency will change the form of the electron wavefunction and may serve this purpose. Secondly, the ion must be small enough to fit in the site.

The trivalent rare earth ions prefer highly coordinated sites that are close to octahedral symmetry and are known to substitute for the highly coordinated lanthanum ion[19] in the GLS based glasses. Clearly, the chromium ion could have replaced the lanthanum in a similar manner and become Cr^{3+}. From the absorption and emission experiments, it is apparent that this has not happened.

In crystals, Cr^{4+} is known to substitute for the tetrahedrally coordinated Si^{4+} and Ge^{4+} ions[1]. In the case of the GLS based glass, the Ga exists in tetrahedral networks[20,20] as GaS_4. Although it is possible that the tetravalent chromium is located in an interstitial site for these glasses, it is more likely it is replacing the Ga ion within the glass using the ready-made tetrahedral sites in a similar way to Cr^{4+} doped crystals.

8.8 Suitability of Cr^{4+} Doped Chalcogenide Glass as a Gain Medium

The Fuchtbauer-Ladenburg equation (see Section 4.2) and the results in this investigation can be used to estimate the $\sigma_e\tau$ product and $\sigma_e(\lambda)$ for these glasses. In a similar treatment to the Cr^{3+} results, this equation provides a method of obtaining the cross-section of emission, in order to assess the glasses' suitability as gain media.

Figure 8.5 shows the cross-section of emission as a function of wavelength for As_2S_3. The parameters entered into the Fuchtbauer-Ladenburg equation were as follows: the QE was assumed to be 3.4% (slightly higher than the measured value on Table 8.3, adjusting for the pump absorbed by the UV-edge). The measured lifetime was taken to be 0.5μs (acknowledging that the real lifetime will be slightly lower than the measured value in Table 8.3 as that experiment only accounted for the high-energy emission). The refractive index for As_2S_3 was taken to be 2.48 at a wavelength of 1μm[21].

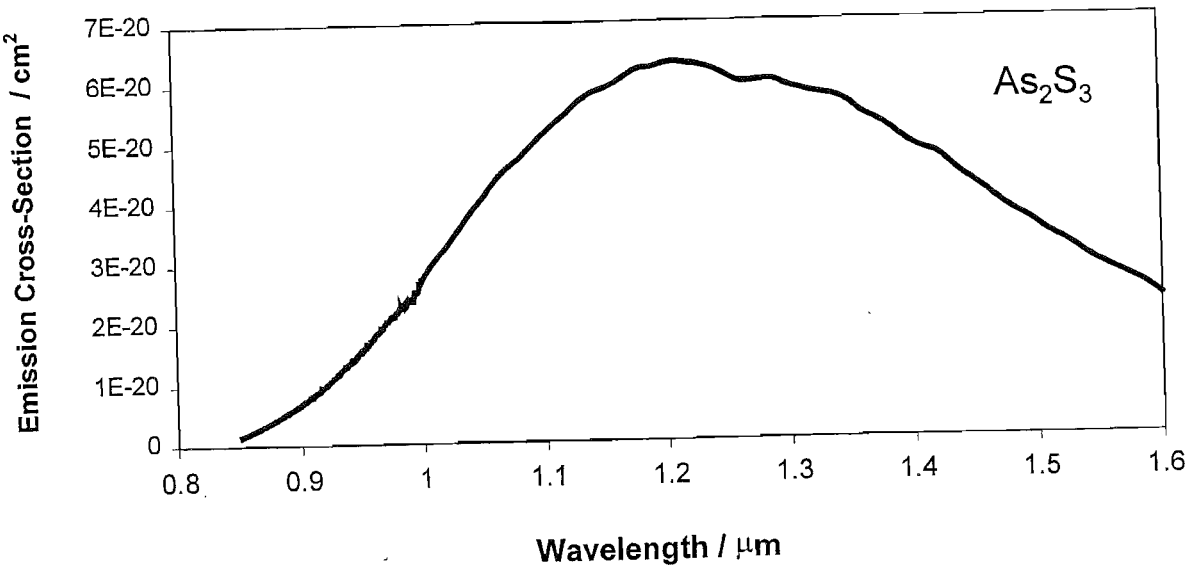

Figure 8.5: Calculated Cross-Section of Emission for Arsenic Trisulphide

The figure shows that the position of the peak for the emission cross-section is just above 1.2μm, excellently positioned for the second telecommunications window for silica fibres. This peak position has made a considerable shift to longer wavelengths relative to the fluorescence spectra (see Figure 8.3) which is explained by the factor of λ^5 in the Fuchtbauer-Ladenburg equation. The strength of the peak cross-section is just over $6x10^{-20}$ cm^2. However, there is a large potential error in this value due, primarily, to the error in the QE (up to 50%). This value can be compared to $1.9x10^{-19}cm^2$ in forsterite[1] crystal which is greater, partly due to smaller emission bandwidth (200nm FWHM)[2].

The parameter with overall importance for a laser is the $\sigma_e\tau$ product. This can be estimated using the Fuchtbauer-Ladenburg equation without the need of correcting the measured lifetime, and is calculated as being $3.2 \times 10^{-26}cm^2s$. This about sixteen times smaller than the value for forsterite[1] ($51 \times 10^{-26}cm^2s$).

Another interesting comparison is the $\sigma_e\tau$ product calculated for Cr^{3+} doped lithium lime silicate glass in Section 4.7 which was $18 \times 10^{-26}cm^2s$, about six times greater. It was hoped at the start of this work that the stronger transition strength of Cr^{4+} doped glasses would make the non-radiative decay less significant compared to Cr^{3+} doped glasses (see Section 8.1) and lead to larger $\sigma_e\tau$ products. Unfortunately, this has not turned out to be the case. The QE is smaller for these Cr^{4+} doped glasses as the non-radiative decay rate has increased even more than the radiative rate. The significantly higher non-radiative decay exists because of the lower energy emission (smaller Dq) and the larger electron-lattice coupling for the Cr^{4+} in these sulphides.

Additionally, the sulphides' Cr^{4+} emission is substantially broader than that of the Cr^{3+}, diminishing the cross-section lifetime product. Despite this, these results suggest that an As_2S_3 Cr^{4+} fibre laser might work but would likely have a very high threshold. What is not known, however, is the position of ESA bands, which could introduce serious problems.

Independent of the emission characteristics of the Cr^{4+} doped chalcogenide glasses, this investigation does lead to the prospect of Cr^{4+} doped fibre for use as a saturable absorber. Further work needs to be carried out to determine the suitability of these glasses' saturation properties[11]. If the glasses were promising, they might also be suitable as cheap saturable absorbers for Q-switching of bulk lasers.

8.9 Summary

If Cr^{4+} doped fibre could be fabricated, some interesting possible applications present themselves, which include a broad band 1.3μm amplifier and a 1μm Q-switching saturable absorber. However, it is unusual for glasses to host the Cr^{4+} ion. Aluminates, gallates and aluminosilicates, the families of glass that are known to support chromium (IV), unfortunately do not have the right thermal properties to draw fibre without the problems of crystallisation.

This chapter reported that sulphide chalcogenide glass, which is suitable for fibre drawing, also hosts the Cr^{4+} ion. Ten glasses were fabricated, including arsenic trisulphide and a number of gallium lanthanum sulphide based glasses, and all were found to host tetravalent chromium. A thorough spectroscopic investigation was carried out, including absorption spectra, temperature dependent emission spectra, room temperature quantum efficiency and radiative lifetime measurements. The most notable results were, firstly, a remarkable blue shift of the emission spectrum (up to 400nm) was observed as the samples were warmed from 70K to room temperature owing to a site-dependent non-radiative decay mechanism. The radiative quantum efficiency for As_2S_3, after adjusting for the absorbed pump power by the UV-edge, was measured to be 3.4%. This was the highest QE value out of all the samples and could be partly attributed to this glass experiencing one of the largest crystal field strengths, leading to a bigger potential barrier for the quenching mechanism. Finally, the radiative lifetimes were all found to be about 1μs and the decays were highly non-exponential.

Using these results and the Fuchtbauer-Ladenburg equation, the $\sigma_e\tau$ product could be calculated. Arsenic trisulphide was the most promising glass in this respect and had a value of $3.2 \times 10^{-26} cm^2 s$. This is about sixteen times lower than that of Cr^{4+}:forsterite crystal and six times lower than the value for Cr^{3+}:LLS glass calculated in Chapter 4.

This latter comparison was disappointing since it was hoped that the greater transition strength of the Cr^{4+} doped glasses would make the non-radiative decay less significant and result in larger $\sigma_e\tau$ products. This has not turned out to be the case. Despite this, these numbers do not rule out the possibility of a Cr^{4+} fibre laser, but the additional information of an excited-state absorption investigation is required in order to make an accurate prediction. However, it is unlikely that these chalcogenide glasses will ever lead to a 1.3μm fibre amplifier with sufficient performance for the telecommunications industry.

---

[1] "Cr^{4+} and Mn^{5+} Active Centers for New Solid State Laser Materials", R Moncorge, H Manaa and G Boulon, Optical Materials, **4**, 139 (1994)

[2] "Laser Action in Chromium Activated Forsterite for Near Infrared Excitation: Is Cr^{4+} the Lasing Ion?", V Petricevic, S Gayen and R Alfano, Appl. Phys. Lett., **53**, 2590 (1988)

[3] Y Chen, L Shiqun, K Lee and S Zhou, Opt. Lett., **18**, 1418 (1994)

[4] "Compositional Dependence of the Valency State of Cr Ions in Oxide Glasses", T Murata, M Torisaka, H Takebe and K Moringa, Journal of Non-Crystalline Solids, **220**, 139 (1997)

[5] "Spectroscopy of Cr^{3+} and Cr^{4+} ions in Forsterite", W Jia, H Liu and S Jaffe, Physical Review B, **43**, (7), 5234 (1991)

[6] "Performance of YAG:Cr^{4+} Laser Crystal", A G Okhrimchuk and J Shestakov, Optical Materials, **3**, 1 (1994)

[7] "Optical Spectrocopy of Cr^{4+}:Y_2SiO_5", C Deka, M Bass, B Chai and Y Shimony, J. Opt. Soc. Am. B, **10**, (9), 1499 (1983)

[8] S P Lunkin, D Galimov and D Yudin, Opt. Spectrosc., **19**, 323 (1968)

[9] "Spectroscopy of Cr^{4+} in MgCaBa Aluminate Glass", X Wu, S Huang, U Hommerich, B Aitken and M Newhouse, Chemical Physics Letters, **233**, 28 (1995)

[10] "Optical Absorption, Absorption Saturation and a Useful figure of Merit for Chromium Doped Glass", E Munin, A Villaverde, M Bass and K Cerqua-Richardson, J. Phys. Chem. Solids, **58**, (1), 51 (1997)

[11] "Near Infrared Emission at 1.35μm in Cr Doped Glass", U Hommerich, H Eilers, W Yen, J Hayden and M Aston, Journal of Luminescence, **60 & 61**, 119 (1994)

[12] "Possible Ways of Relaxation for Excited States of Rare Earth Ions in Amorphous Solids", R. Reisfeld, Journal de Physique, **46**, c7-349 (1985)

[13] D Hewak, Chemistry in Britain, **33**, (5)

[14] "Transmission Loss Characteristics of $As_{40}S_{60}$ and $As_{38}Ge_5Se_{57}$ Glass Unclad Fibers", T Kanamori, Y Terunuma, S Takahashi and T Miyashita, Journal of Non-Crystalline Solids, **69**, 231 (1985)

[15] B Seddon, Corning Inc., USA (Private Communication)
[16] V Krateva, Rutgers University, Piscataway, NJ. (Private Communication)
[17] D Hewak and D Brady, ORC, University of Southampton. (Private Communication)
[18] H Tawarayama, "Optical Amplifiers and their Applications" (PDI)
Victoria, Canada, July 21-23 (1997)
[19] "An EXAFS Structural Approach of the Lanthanum-Gallium-Sulfur Glasses",
S Benazeth, M Tuilier, A Loireau-Lozach, H Dexpert, P Lagarde and J Flahaut,
Journal of Non-Crystalline Solids, **110**, 89 (1989)
[20] "A Structural Study of Gallium Lanthanum Sulphide Glass Bulk and Thin films by
X-ray Absorption Fine Structure Spectroscopy"
R Asal, J. Phys. Condens. Matter., **9**, 6217 (1967)
[21] "Handbook of IR Optical Materials", ed. P Klocek, Marcel Dekker Inc. (1991)

Chapter 9

Summary and Future Directions

9.1 Introduction

In the last three decades, since highly transmitting silica fibres have been identified as the principal element for optical telecommunications systems, tremendous efforts have been made in developing techniques to eliminate the presence of transition metals during fibre fabrication. Transition metal impurities within glass, such as Fe^{2+}, Co^{2+}, Ni^{2+}, Cu^{2+} and Cr^{3+} etc, can cause several hundreds of dB/km loss with impurity-ion content of only 1ppm[1]. In complete contrast to this history, the objective of this project has been to purposely dope optical fibre with transition metal ions with the aim of developing a new class of laser. To date, there has been no demonstration of a transition metal ion laser using a glass host. This is particularly a consequence of these ions' poor radiative quantum efficiency within glass resulting in threshold pump powers for bulk lasers that are infeasibly high. The fundamental idea underpinning this project was that if the pump and signal beams could be confined to the small cross-sectional area of a fibre core, then the lower thresholds might make laser action possible.

The approach taken throughout this project was to search for suitable host glasses which have promising spectroscopy whilst simultaneously possessing the correct thermal properties for fibre drawing. The two key spectroscopic investigations for evaluating the glasses were measurement of the radiative quantum efficiency (QE) and the excited state absorption spectrum. Together, these results led to estimates of the emission cross-section lifetime product, which could be used to evaluate the prospect of gain.

The work in this project comprised two parts. Firstly, there was the identification of lithium lime silicate glass as an excellent host for Cr^{3+}. This glass's composition was optimised spectroscopically and subsequently a technique to fabricate low loss LLS fibre was developed. The second part to the project was the spectroscopic investigation of a range of Cr^{4+} doped sulphide chalcogenide glasses. Undoubtedly, fibre lasers or

amplifiers using either of these transition metal ions would lead to interesting devices. Manufactured from glass hosts rather than expensive crystal and having absorption bands that are suitable for diode laser pumping, these devices could be both cheap and compact. The extremely broad emission would lead to highly tunable lasers or broad band amplifiers and at particularly useful wavelengths. The Cr^{3+}emission extends between 700nm and 1050nm giving rise to a laser that would be an alternative to the Ti:sapphire. The emission of Cr^{4+} stretches between 0.8μm and 1.5μm leading to an amplifier that would cover the second telecommunications window.

9.2 Cr^{3+}:Lithium Lime Silicate Work

The first stage of development of a Cr^{3+} fibre laser was the selection of favourable host glasses. Generally, the radiative quantum efficiency of Cr^{3+} doped glass is very poor (often less than 5%) due to a thermal quenching mechanism. Chapter 4 reported the spectroscopic investigation of Cr^{3+} doped lithium lime silicate (LLS) -- a particularly promising glass for a fibre laser. Relatively easy to melt, LLS was reported in the literature as having one of the highest QEs amongst glasses, which will lead to an increased $\sigma_e\tau$ product. Lithium lanthanum phosphate, aluminium phosphate and lead germanate were also investigated, but were found to have problematic melting or inferior QE compared to the LLS.

A large range of bulk samples was fabricated, based upon the original LLS composition from the literature. The compositions were carefully selected so that the QE could be optimised and the effect of Cr concentration could be investigated. The spectroscopic evaluation included absorption spectra and temperature dependent emission spectra, temperature dependent and emission wavelength dependent radiative lifetimes, quantum efficiency and refractive index measurements. Wherever possible the results were linked to transition metal theory and the important parameters for a potential fibre device have been found. These included QE of 15%, lifetime of 36μs, refractive index of 1.56 for the basic composition of LLS. These numbers lead to a calculated value for the peak cross-section of emission of $6 \times 10^{-21} cm^2$.

An important finding that came from the QE investigation was strong confirmation of the theory put forward by Kisilev and Reisfeld[2] that increasing the size of the modifying cation led to a marked decrease in the QE for the Cr^{3+}. Overall, one of the most notable features of the results was that the basic composition of LLS was already quite close to being optimised. Only small changes in certain elements of the composition brought benefits to the spectroscopy, but more often quite large changes had little effect on the QE.

Chapter 6 described the developmental work for LLS fibre fabrication. Differential thermal analysis experiments showed that the basic composition of LLS was a very stable glass with T_x at 795°C and T_g àt 500°C. Precautions were taken to reduce the final fibre loss. In particular, modifications were made to the LLS core composition to lower its viscosity, reducing the bubble content within the glass. These modifications could be made in the knowledge that they did not detrimentally affect the quantum efficiency, using the spectroscopy results from Chapter 4. In addition, a glass-melting schedule was developed which further aided the removal of bubbles from the glass. It was also found that the details of the annealing treatment were critical to ensure that the cast glass was robust enough to drill the LLS cylinders for the preform.

A rod-in-tube technique was used to draw the fibre. The cladding glass chosen was the commercial glass Schott LLF2, which led to a fibre numerical aperture of 0.26 at 589nm. This commercial glass had a fibre drawing temperature 45°C lower than T_x for the modified core composition of LLS, reducing the possibility of crystallisation problems. A range of fibre was fabricated with different core diameters to give some flexibility for the fibre experiments. Unfortunately, there were problems with the final narrow-cored fibre. Firstly, the fibre snapped during the latter stages of the drawing process with the consequence that the smallest core diameter produced was 5μm. Additionally, the outer cladding collapsed poorly onto the inner cladding of the dual clad fibre. Although this feature would not affect the core modes, cladding modes were extremely difficult to remove during the fibre experiments. However, there was no evidence of problems with bubbles or crystallisation within the fibre and future fibre drawing trials should be able to avoid the difficulties experienced on this occasion.

Chapter 7 reported the results for the LLS fibre experiments including fibre loss, ESA and gain investigations. Although the scope of the investigation was limited by the problems with the narrow-cored fibre, important results were obtained.

The material loss for the LLS fibre, found by cutback measurement on a 30μm diameter core fibre section, was found to be 3.5dB/m. The effects of extrinsic scattering and the loss for the narrow-cored fibre could not be evaluated because of the presence of the unwanted cladding modes. However, shining laser light along the fibre revealed that there were no obvious poor sections of fibre with high concentration of scattering centres such as crystals or bubbles.

Excited-state absorption (ESA) can be a major influence in determining the usefulness of a fluorescent material for laser applications. Its presence can impair the pumping efficiency or reduce the effective emission cross-section if the ESA overlaps the ground state absorption or the emission bands respectively. The large-core highly-multimode fibre was also used for the ESA investigation and we believe this to be the first report of an ESA measurement for a transition metal ion within a glass host. The results showed two broad bands, $^4T_2 \rightarrow {}^4T_1b$ (400-500nm) and $^4T_2 \rightarrow {}^4T_1a$ (600-750nm), which to a large degree overlapped the ground state absorption bands. These results suggested that the best pump wavelength to maximise a population inversion was 600-640nm. Although the strength of the $^4T_2 \rightarrow {}^4T_1a$ ESA band was diminishing as it approached the longer emission wavelengths, it was still of great significance as it suggested ESA cross-section was greater than the emission cross-section. If correct there would be no possibility of gain or a laser no matter what the fibre geometry of pump power. However, the degree to which the effective emission cross-section was reduced by the ESA cross-section was difficult to ascertain accurately, as the signal to noise ratio was poor for this wavelength range and there was a possibility of a zero offset distorting the results. Because of these problems a gain investigation was still carried out.

The complications with the fibre quality severely hampered the gain investigation and led to a result that was not clear-cut. A small gain effect was observed that was similar in shape to the predicted gain spectrum, peaking at 840nm. The size of the effect was only 8%, but this value would have been diminished by a large unknown offset of the probe light propagating as cladding modes. At the same time, though, there was an

unexpected peak at 750nm where no gain should exist. This cast doubt on the legitimacy of attributing the 840nm peak as gain. However, an investigation into the size of the gain effect whilst varying the probe power showed that the two peaks had differing origins, with only the 840nm peak being consistent with genuine small signal gain.

The gain model suggests that if the emission cross-section is indeed bigger than the ESA cross-section, then using a smaller-cored fibre (e.g. 3μm diameter) will lead to a more distinct gain result. If the small-cored fibre loss is not too high, being dominated by extrinsic scattering, a Cr^{3+}:LLS fibre laser might be possible.

9.3 Suggestions for Future Cr^{3+} Work

9.3.1 Further LLS Fibre Fabrication Trials and Fibre Experiments

If an improved LLS fibre could be fabricated with a 3μm core diameter and no problems with cavities, much improved and clearer results should be obtained. There would be a greater idea of the problems of extrinsic scattering and the relevant fibre loss, more conclusive ESA and gain results could be achieved, and if gain exceeds the cavity loss a fibre laser could be demonstrated.

Although the rod-in-tube technique has the advantage of being a simple and versatile method of fibre fabrication, it can bring problems of imperfections on the interface between the rod and tube, resulting in higher losses. Other methods, for instance fabricating the preforms by extrusion, may significantly improve the loss.

9.3.2 Cr^{3+} Doped Glass Ceramics

Glasses that have had a post-annealing thermal treatment to grow nanocrystals are termed glass ceramics. These materials can be transparent despite a high crystalline fraction, as the small size of the crystals does not result in scattered losses. Whilst these materials can be cheap to produce, compared to the expense of fabricating crystals, they can offer an additional range of material properties.

If an optically active ion is incorporated into the nanocrystals, the local crystalline environment can change the fluorescent characteristics. It has been shown that rare earth ions doped in transparent glass ceramics, such as Pr^{3+} in oxyfluoride[3], can bring about an increase in the radiative quantum efficiency compared to glass. A similar increase in QE has also been observed in glass ceramics[4,5] doped with Cr^{3+}. In this case, the immediate crystalline surroundings will also act to narrow the emission profile and the ESA bands. If these effects increase the $\sigma_e\tau$ product sufficiently, then a Cr^{3+} doped glass-ceramic waveguide laser might become possible. However, the obstacle here likely to be that the high Cr concentration required for such a short device brings concentration quenching problems.

Recently, low-loss glass-ceramic optical fibre has been demonstrated [6]. If a suitable Cr^{3+} glass ceramic could be drawn into a fibre, then this could provide improved spectroscopy simultaneously with excellent pump and signal confinement.

9.4 Cr^{4+} Doped Chalcogenide Glass Spectroscopy

If Cr^{4+} doped fibre could be fabricated, some interesting possible applications present themselves, which include a broad band 1.3μm amplifier and a 1μm Q-switching saturable absorber. However, it is unusual for glasses to host the Cr^{4+} ion. Aluminates, gallates and aluminosilicates, the families of glass that are known to support chromium (IV), unfortunately do not have the right thermal properties to draw fibre without the problems of crystallisation.

Chapter 8 reported that sulphide chalcogenide glasses, which are suitable for fibre drawing, also host the Cr^{4+} ion. Ten glasses were fabricated, including arsenic trisulphide and a number of gallium lanthanum sulphide based glasses, and all were found to host tetravalent chromium. A thorough spectroscopic investigation was carried out, including absorption spectra, temperature dependent emission spectra, room temperature quantum efficiency and radiative lifetime measurements. The most notable results were, firstly, a remarkable blue shift of the emission spectrum (up to 400nm) was observed as the samples were warmed from 70K to room temperature owing to a site-dependent non-radiative decay mechanism. The radiative quantum efficiency for

As_2S_3, after adjusting for the absorbed pump power by the UV-edge, was measured to be 3.4%. This was the highest QE value out of all the samples and could be partly attributed to this glass experiencing one of the largest crystal field strengths, engendering a bigger potential barrier for the quenching mechanism. Finally, the radiative lifetimes were all found to be about 1μs and the decays were highly non-exponential.

One of the biggest successes of this project was the clear demonstration of the thermal quenching mechanism, described in Section 2.6, given by the QE results and temperature dependent emission spectra. This was especially true for the selection of Cr^{4+} doped chalcogenide glasses investigated. The range of QE values for these samples could be qualitatively linked to the crystal field strength and the extent of the electron-lattice coupling.

Using the results for the chalcogenide glasses and the Fuchtbauer-Ladenburg equation, the $\sigma_e\tau$ products could be calculated. Arsenic trisulphide was the most promising glass in this respect and had a value of $3.2 \times 10^{-26} cm^2 s$. This is about sixteen times lower than that of Cr^{4+}:forsterite crystal and six times lower than the value for Cr^{3+}:LLS glass calculated in Chapter 4. This latter comparison was disappointing since it was hoped that the greater transition strength of the Cr^{4+} doped glasses would make the non-radiative decay less significant and lead to larger $\sigma_e\tau$ products. This has not turned out to be the case. Despite this, these numbers do not rule out the possibility of a Cr^{4+} fibre laser, but the additional information of an excited-state absorption investigation is required in order to make an accurate prediction. However, it is unlikely that these chalcogenide glasses will ever lead to a 1.3μm fibre amplifier with sufficient performance for the telecommunications industry.

9.5 Suggestions for Further Work on Cr^{4+} Doped Chalcogenide Glass

9.5.1 ESA and Fibre Experiments

In order to make a better prediction of whether a Cr^{4+} chalcogenide fibre laser is practicable, data on the ESA is required. These experiments could be done with fibre or in bulk samples. It is possible that knowledge of the ESA may make As_2S_3 no longer the best candidate or rule out the possibility of a laser altogether.

Although these Cr^{4+} doped chalcogenide do not have as large $\sigma_e\tau$ products as Cr^{3+} doped LLS, they may still provide a good opportunity to demonstrate a laser because lower loss fibres are easier to fabricate. The ORC is working towards the technology to make low loss GLS fibre and the best fibre loss for arsenic sulphide glass[7] ($As_{40}S_{60}$ at 2μm) is 0.1dB/m.

9.5.2 Cr^{4+} Saturable Absorber

There is great interest in the development of solid-state saturable absorbers. Such devices can support an all-solid-state laser technology overcoming the disadvantages of liquid dye solution passive Q-switches. The Cr^{4+} absorption band, extending between 0.6μm to 1.2μm, covers the emission of some important lasers. Cr^{4+} doped crystals, such as Y_2SiO_5 (YSO) and $Ca_2Al_2SiO_7$ (CAS), have been placed inside the resonator of a tunable Cr^{3+}:LiSAF laser to achieve passive Q-switching action between 800 and 900nm[8]. Similarly, Cr^{4+} doped crystals have made possible the construction of passively Q-switched microchip lasers[9]. Because glasses can be manufactured with excellent optical quality at a cheaper price than most crystals, they would make a very attractive choice for a Cr^{4+} saturable absorber. The principal characteristic that makes a material suitable for this application is a high bleached transmission, with little loss due to ESA or scattering[10]. It is suggested that investigation of the saturation properties for the chalcogenide glasses is needed to determine whether they have a future in this area. One major advantage of these glasses is that, because they have thermal properties suitable for fibre drawing, they offer the opportunity for an all-fibre passive Q-switching element for a Nd fibre laser at 1.06μm.

9.5.3 Cr^{4+} Glass Ceramics

Glass ceramics would bring the same advantages to the Cr^{4+} ion as they would Cr^{3+} (see Section 9.3.2). If Cr^{4+} doped glass ceramic fibre could be fabricated, then the improved spectroscopic parameters could perhaps lead to a broad band amplifier with sufficient performance for telecommunications.

---

[1] K Beales and C Day, Phys. Chem. Glasses, **21**, (1), 5-21 (1980)

[2] "Spectral Characteristics and Fluorescence Quantum Efficiencies of Cr (III) in Phosphate and Silicate Glasses with Li and Be Modifiers", A Kiselev and R Reisfeld, Solar Energy, **33**, (2), 163 (1984)

[3] "Quantum Efficiency of Pr^{3+} Doped Transparent Glass Ceramics" R Quimby, P Tick, N Borrelli and L Cornelius, Journal of Applied Physics, **83**, (3), 1649 (1998)

[4] "Excited States of Chromium (III) in Translucent Glass Ceramics as Prospective Laser Materials", R Reisfeld and C Jorgensen, Structure and Bonding, **69**, 63 (1988)

[5] "Cr (III) in Gahnite Containing Transparent Glass Ceramics – Influence of Melting Conditions and Heat Treatment on Crystallisation and Spectroscopic Parameters", A Kisilev, R Reisfeld, A Buch and M Ish-Shalom, Chemical Physics Letters, **129**, (5), 450 (1986)

[6] "Are Low-Loss Glass Ceramic Optical Waveguides Possible?", P Tick, Optics Letters, **23**, (24), 1904 (1998)

[7] "Transmission Loss Characteristics of $As_{40}S_{60}$ and $As_{38}Ge_5Se_{57}$ Glass Unclad Fibers", T Kanamori, Y Terunuma, S Takahashi and T Miyashita, Journal of Non-Crystalline Solids, **69**, 231 (1985)

[8] "Broad Band Intensity Dependent Absorption in Tetravalent Chromium Doped Crystals", E Munin, A Villaverde, X Zhang and M Bass, Appl. Phys. Lett., **63**, 1739 (1993)

[9] "Diode Pumped Passively Q-Switched Picosecond Microchip Lasers", J Zayhowski and C Dill, Opt. Lett., **19**, 1427 (1994)

[10] "Optical Absorption, Absorption Saturation and a Useful figure of Merit for Chromium doped Glasses", E Munin, A Villaverde, M Bass and K Cerqua-Richardson, J. Phys. Chem. Solids, **58**, (1), 51 (1997)